FINITE ELEMENT ANALYSIS OF TUMBLING MILL DESIGN AND OPERATING EFFECTS ON LINER BOLT STRESSES, LINER STRESSES AND MILL RESONANCE

By

Yuyun Quan

February, 2006

Department of Mechanical Engineering

McGill University

Montreal, Quebec, Canada

A Thesis Submitted to

McGill University

in partial fulfillment of the requirements for the degree of

Master of Engineering

Your file Votre référence
ISBN: 978-0-494-25010-5
Our file Notre référence
ISBN: 978-0-494-25010-5

Abstract

Tumbling mills describe a class of mechanical systems defined by a cylindrical chamber filled with balls and/or rocks that rotate around their own longitudinal axis. Due to the action of charges, the lifters/liners wear significantly and their shape will be changed which will influence the efficiency of the mill. Liner bolts are the mill components which connect the mill interior with the exterior environment. With this property, bolts have been paid more and more attention. The first part of the thesis covers the structural analysis of the lifter/liner bolts, and the possibility for on-line charge motion measurement with the aid of bolts is discussed by comparing the strain distributions at the bolt areas where the bolts occupy different mill circumferential positions. In order to measure the lifter/liner wear, a real-time, on-line wear sensor was developed by the Comminution Dynamics Laboratory. However, the positioning of the sensor/sensors affects the strength of the mill is unknown. The second part of the project provides detailed research on this issue by FEA analysis so as to provide a basis for the practical application of this kind of sensors. Finally, during the grinding process of tumbling mills, some mills can vibrate greatly at some ranges of mill rotating speeds and as a result the mills cannot work properly because of this vibration or resonance. With six different mill models, the final part of the thesis investigates the mill natural frequencies and their modes by FEA and furthermore, explores the effect of mill diameter, length on these frequencies and modes.

Resume

Les moulins à boulets sont une classe de systèmes mécaniques définis par une chambre cylindrique remplie de boulets et/ou de roches qui tournent autour de l'axe longitudinal. En raison de l'action de la charge, les releveurs/revêtements usent de manière importante, changeant ainsi leur forme, ce qui influence fortement l'efficacité du moulin. Les boulons qui fixent le revêtement sont des composantes très importantes. Elles relient l'intérieur du moulin à l'environnement extérieur. À cause de cette fonction, les boulons reçoivent de plus en plus d'attention. La première partie de cette thèse couvre l'analyse structurale des boulons des releveurs/revêtements; en comparant les distributions de contraintes près des boulons occupant différentes positions périmétriques, la possibilité de la détermination continuelle du mouvement de la charge à l'aide des boulons est discutée. Afin de mesurer l'usure des releveurs/revêtements, un capteur opérant en temps réel a été développé par le Comminution Dynamics Laboratory de l'Université McGill. Cependant, si et comment le positionnement du capteur affaiblit le moulin est inconnu. En utilisant la méthode d'éléments finis, la deuxième partie de ce projet présente la recherche détaillée sur cette question, afin de fournir une base pour l'application pratique de ce genre de capteurs. En conclusion, pendant le processus de broyage, certains moulins à boulets peuvent vibrer considérablement, surtout à certaines vitesses d'opération. En conséquence, les moulins ne peuvent pas fonctionner correctement en raison de cette vibration ou résonance. Avec six modèles de moulin différents, la partie finale de la thèse étudie les fréquences normales des moulins ainsi que leurs modes par éléments finis, explorant l'effet du diamètre du Moulin et de la longueur sur des fréquences naturelles et des modes des moulins.

Acknowledgements

I am very delighted to take this opportunity to express my sincere gratitude and thanks to my supervisor, Prof. Peter Radziszewski for his patient, precious guidance throughout this project. Thanks to him for giving me this opportunity to set foot in the milling research, which greatly broadens my horizon. The smooth completion of the thesis cannot be separated from his rich experience and invaluable advice. I heartily thank him for his financial support to me from the very beginning of my thesis. It is really a very pleasant period of time to work and study with such an easy-going supervisor.

Sincere thanks to Mr. Sudarshan Martin and Wei Li who provide me many useful information about the liner sensor. I would like to thank all the other Communition Dynamics Laboratory group members. From the regular meetings and their wonderful presentations, I benefit a lot.

I would also like to thank COREM, with which part of the present work is cooperated. Special thanks to Mr. Sylvain Caron, research engineer of COREM for his beneficial discussion and advice to the project.

Last but not the least; I would like to thank my husband and two lovely daughters for all their understanding and support.

Table of Contents

List of Tables

List of Figures

CHAPTER 1

INTRODUCTION

1.1 Tumbling Mill Grinding

Mineral processing, sometimes called ore dressing, mineral dressing or milling is the practice of extracting valuable minerals from their ores. Industrial mineral treatment processes usually combine a number of unit operations in order to liberate, concentrate and classify minerals using physical properties and processes. Mineral processing involves manipulating particle size by crushing and grinding the ore. Combined with particle size classification unit operations, this area is often termed comminution. Since most minerals are finely disseminated and intimately associated with the gauge, they must be initially "unlocked" or "liberated" before separation can be undertaken. Comminution, which is the first stage of mineral processing, is to separate valuable minerals contained in the ore from the non-valuable host rock by progressively reducing the size of the ore. In the minerals sector, comminution takes place mainly within mills as part of the run of mine processing. A criticism of the comminution process has been its reliance on high-energy consumption to grind coarse materials to either separate a precious metal, such as gold, or to produce an industrial mineral, such as concrete. The industries which produce large quantities of mineral through comminution have become much more energy-conscious, and research being undertaken globally reflects this move towards a 'greener' milling footprint.

During the process of comminution, crushing is the first mechanical stage and grinding is the last stage. Grinding is the required process when size reduction of below 5-20 mm is needed. Grinding systems are a symbol of the application of brute force to extract mineral wealth from nature and are a major and critical part of any mineral processing facility. Grinding is a powdering or pulverizing process, and it can use three methods: tumbling, stirring or vibration.

Grinding of materials in a tumbling mill with the presence of metallic balls or other media dates back to the late 1800's. Figure 1.1 shows a primary grinding circuit [1]. Tumbling mills are large-scale grinding devices commonly used in mineral processing. They describe a class of mechanical systems defined by a cylindrical chamber filled with balls and/or rock that rotates around its own longitudinal axis. They are either cylindrical in shape or modified cylinders. These mills are used at the last stage in the comminution process to grind a given ore to a desired size. This class of mechanical systems is used to grind to a desired quality of different material in at least three industries: mining, cement and metal powder industries (ore, clinker and metal powder). Tumbling mills include autogenous mills, rod mills, ball mills and roller mills.

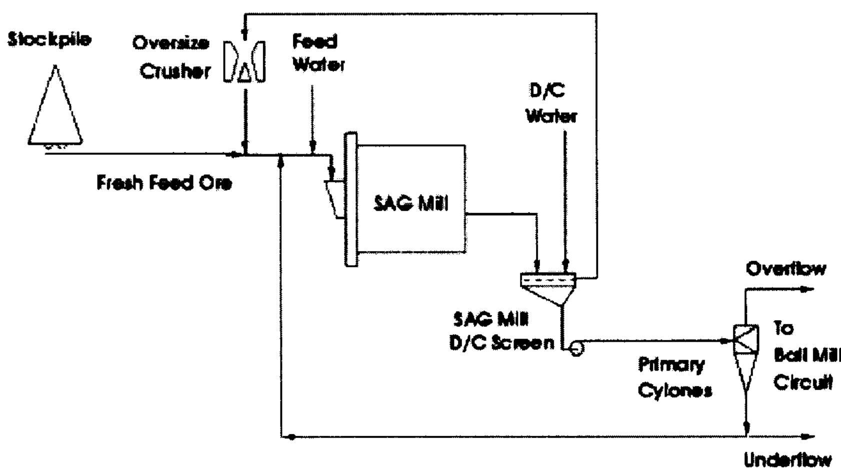

Figure 1.1 Primary grinding circuit [1]

Autogenous (AG) grinding is the size reduction of material in a tumbling mill utilizing the feed material itself as grinding media. This type of mill consists of a large diameter, short length cylinder fitted with lifting bars. The cylinder is fed with a coarse feedstock of up to 250mm in size and in rotating, the feedstock is lifted and then allowed to drop through a significant height. Three significant mechanisms cause the breakdown of the mineral: (1) impact due to the fall of the mineral onto the charge below causes a reduction in the size of the feedstock; (2) attrition of smaller particles between larger grinding bodies; (3) abrasion or rubbing off of particles from the larger bodies. Steel or ceramic balls are often added to aid with the reduction process (the mill is then referred to as a semiautogenous mill). The process can be carried out wet or dry. Removal of the final product can be carried out using air (where the process is dry) removing only the fines. Rotational speed is usually fairly low, about 80% of critical speed (critical speed is the speed at which the charge will be pinned to the rotating drum and does not drop) and typical drum diameter ranges from 2 to 10 meters. Autogenous mill is often used as a single stage process, providing sufficient size reduction in a single process. Alternatively, it can be part of a two-stage process where further size reduction is required. Autogenous mills are most suited to large installations, i.e., more than 50 tones per hour and have a power requirement ranging from 40 KW up to hundreds of KW. Besides, this type of mill is only suited to certain kinds of minerals, which have a fairly coarse nature but once broken will disintegrate readily into small sizes. In certain circumstances this type of mill can deliver a product with a fineness of less than 0.1mm. Testing is required beforehand to determine the suitability of a mineral for processing in an autogenous mill. Autogenous mills have the distinct advantage of accepting coarse feedstock and supplying a relatively fine finished product, often sufficient as an end product. This can provide a reduction in plant costs if a single mill is used as a substitute for two or more stages.

Semi-Autogenous (SAG) grinding is the size reduction of material in a tumbling mill utilizing the feed material plus supplemental grinding media. The most common supplementary medium is steel balls. Grinding is a fundamental process in the mineral industries. Grinding mills are often very large machines. Their efficiency and energy consumption therefore are of major importance. The employment of ball mills with a diameter over 5 meters in industry began only a decade ago. The abnormal behavior of these big mills surely surprised many who had an optimistic view of them. However, the problems have to be overcome since the trend of increasing mill size is still prevailing.

Tumbling mills range in size from small 1 ft diameter lab mills to a 40 ft diameter semi-autogenous industrial mill. Figure 1.2 shows a 40ft diameter SAG mill. Tumbling mills are composed of three main interactive and interdependent elements: the mill shell, liners/lifters and charge. These three elements work together to impact energy on the mill charge through the rotational motion of the mill shell.

Mill shells are designed to sustain impact and heavy loading, and are constructed from rolled mild steel pates, buttwelded together. Holes are drilled to take the bolts for holding the liners.

Mill shell has 4 types: pancake, square, tube, conical as showed in Figure 1.3.

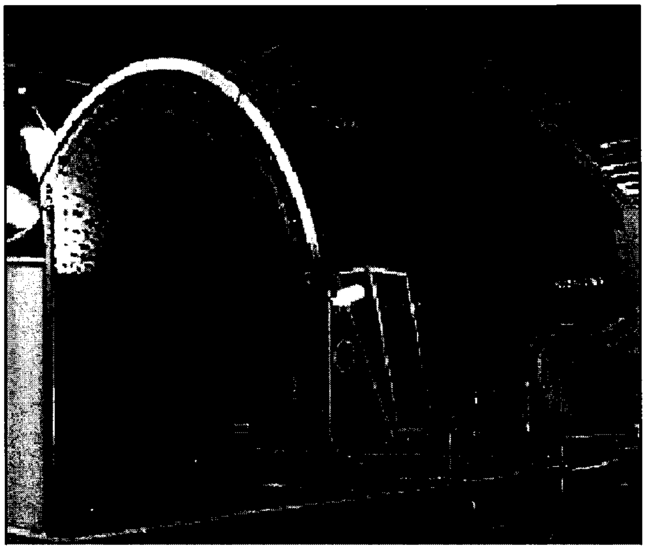

Figure 1.2 40 ft diameter SAG mill [2]

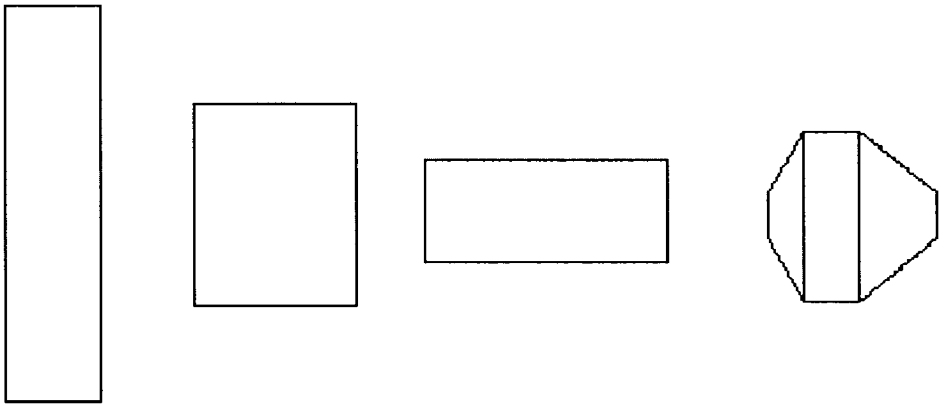

Pancake Square Tube Conical

Figure 1.3 Mill shell types

The internal working faces of mills consist of renewable liners, which must withstand impact, be wear-resistant, and promote the most favorable motion of the charge. Ball-mill ends usually have ribs to lift the charge with the mill rotation. These prevent excessive slipping and increase liner life. Liners are usually made of white cast iron, alloyed with nickel (Ni-hard), other wear-resistant material or rubber. Liners are generally shaped to provide lifting action and to add to the impact and crushing effect. Some common shapes of liners are showed in Figure 1.4. The liners are attached to the mill shell and ends by forged steel countersunk liner bolts. Mill liners are a major cost in mill operation, and efforts to prolong liner life are constantly being made.

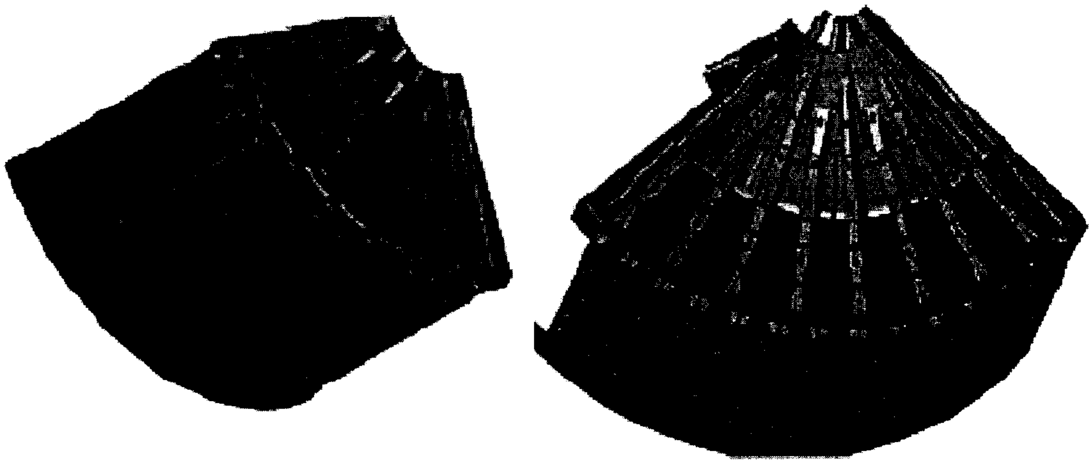

Figure 1.4 Typical mill liners [2]

Mill liners are the agents that transmit energy and motion to grinding balls, which in turn, crush and grind ore particles [3]. The way in which mill liners agitate the ball charge determines how the balls will grind ore and how the liners will wear.

Liners are usually made of cast materials such as Ni-Hard, chrome-molybdenum steel, and manganese steel. Rolled alloy steel plate with lifter bars is also used. Using of a backing material, such as rubber between the liners and the mill shell provides additional benefits.

A liner that includes lifter bars offers unlimited potential for identifying the optimal solution. The shape and height of the lifter bars are the most important factors for grinding. From the standpoint of liner economy, the lifter bars should be as high as possible in order to provide maximum service life. But the required grinding performance is a constraint on lifter bar height. The bars become rounded off after roughly 10% of service life has elapsed. An important factor related to drop height is the increase in charge pressure as lifting height is increased. Besides, the maximum height from which the ball cataract begins is very important to liner damage. The shape and geometry size of lifters are very much related to energy consumption and mill efficiency. More energy will be consumed in impact type breakage as the number of lifters increases within a mill of given size. Results also show that power consumption for given mill and charge properties decrease with an increase of the height of the lifters [4]. So, the design of the mill liner has an effect on both solutions. Liner design must take account of several parameters such as energy consumption, liner economy, and liner life, grinding media economy, capacity and product size. Previously, liner design was mostly based on plant experience, and this practice continues today. And now, everyone agrees that correct liner design is important. Dunn concluded that liner design is one of the most important factors that can be varied widely, easily and inexpensively to attain optimum capacity [5].

A very important issue about liner and lifter design is wear. During the life cycle of the liner and lifter, the profile of the lifter will change greatly because of wear. Generally, the liner/lifter can only be used for a few months and must be replaced by a new one for this reason. Figure 1.5 shows the lifter profile wearing process. Changing liner/lifter is complex work and costs a lot for large mills.

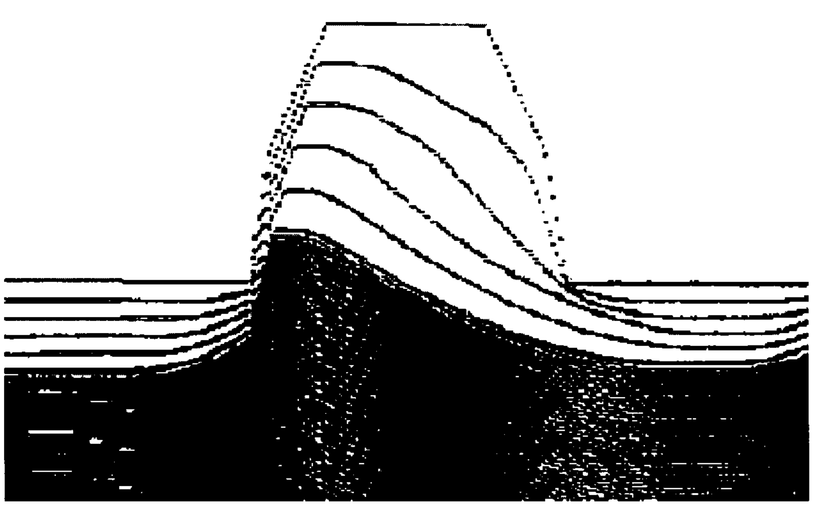

Figure 1.5 Bevel liner profile simulation [6]

Wear is a loss or redistribution of surface material from its intended location by definition of the ASTM. The wear life of mechanical components is affected by nearly as many variables as those affecting human life. Wearing surfaces respond to their environment, method of manufacture, and conditions of operation. In the mechanical concept of wear, the contact between bodies is prerequisite for wear to take place. Wearing is not only related to the contact area, but also related to the presence of oxides, absorbed gases on surfaces and repeated contact on sliding surfaces, which may lead to fatigue modes of material loss. Factors that influence wear include the contact pressure or stress, the temperature caused by ambient heating and frictional temperature rise, the sliding speed, misalignments, duty cycles, and the type of maintenance the designed item will receive. For that reason, most wearing surfaces have to be redesigned in order to function normally.

The mill charge is composed of steel media, rock and slurry. The wear of the steel media constitutes a large portion of mill operating costs. Figure 1.6 shows the charge motion. The analysis of the charge motion inside the ball mill under various mill conditions is important because it can lead to some practical information. The charge breakage property is shown by the proportion of the charge that is in flight and the proportion that is in rotation. The dilation and contraction of the charge bed shows the mill transport property.

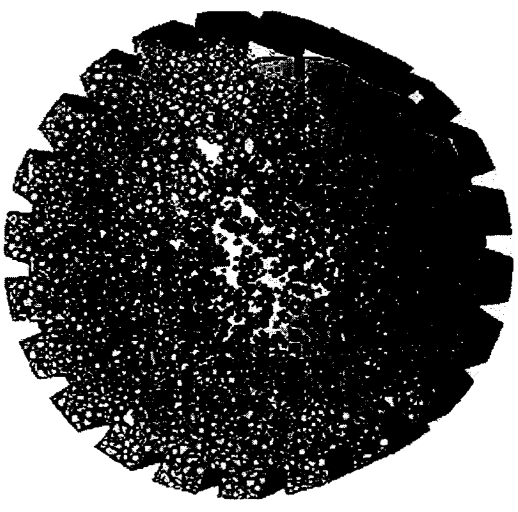

Figure 1.6 Simulated mill charge motion [7]

When a material is to be milled there are certain characteristics which have to be taken into account. These include the following:

- Hardness
- Brittleness
- Toughness
- Abrasiveness
- Stickiness
- Softening and melting temperature
- Structure (e.g. close grained or cellular)
- Specific gravity
- Free moisture content
- Chemical stability
- Homogeneity
- Purity

The mill power draft and grinding efficiency depend on the motion of the grinding charge and the ensured ball collisions that utilize the electric power and cause particle breakage. The movement of balls and rocks in tumbling mills has been of interest since the beginning of the century when Davis (1919) first studied single ball trajectories. And in the following decades, the profile of the cascading charge began to figure on mill power prediction. [5].

1.2 Tumbling Mill Dynamics Investigation

Generally speaking, there are two methods in use now for mill dynamics research, that is, soft experiment, which simulates the charge motion with computer codes and real experiment, which mainly uses sensors to investigate the behavior of charge motion.

1.2.1 Simulation

With advanced computer technology, research into understanding the complex interactions of mineral processes is now a practical proposition for aiding design and optimization. In comminution research, recent trends have been made to describe internal dynamics of mills using the discrete element method (DEM), which simulates the movement of elements within the milling process based on mathematical and physical analysis represented in high definition graphics and animation. Discrete element modeling (DEM) has been used for several years to model large mills. Most DEM work has been based on non-commercially available codes, which are developed and used in house [8]. DEM researches are mostly anchored in physical fundamentals of particle motion and produce broadly similar results to charge motions profiles. The Powell/Nurick single ball trajectory model defines well the outer extremity of the mill charge. Mishra/Rajamanis' model simulates the individual balls while Radziszewskis' model agglomerated ball technique permits fast calculation of charge profiles. Two of the models (Mishra/Rajamani, Radziszewski) predicted ball mill power quite well when the Morrell no-load power was included. However, these two approaches to DEM modelling have advantages and disadvantages. Basically, the strength of one approach becomes the weakness of the other. [9]

The charge motion model developed by Radziszewski takes advantage of the empirical approach of Morrell [9] while being anchored in the fundamentals of discrete element models such as those of Inoue [10] and Mishra/Rajamani [11]. This technique permits charge motion to be calculated while determining a frequency distribution of impacts for any given mill, be it grate or overflow discharge.

In general, ball mills operate at speeds varying between 65 and 85 per cent of critical, whereas autogenous and semi-autogenous mills operate at speed up to 90 per cent of critical. In particular cases, some slippage might occur between the load and the liners, and the mill has to be run at a higher speed to overcome this and to rotate the load at an acceptable speed.

The typical charge motion profile (Figure 1.7) shows four zones that can be characterized by the type of action produced there. That is, the fall zone where balls in flight follow a parabolic path under the action of gravity; the crushing zone where balls in flight re-enter the charge and crush rock particles at relatively high energies; the grinding zone where ball layers slide over one another grinding the material trapped between them; and finally, the tumbling zone where balls roll over one another and break material in low energy breakage. When the mill speed is increased, a cascade effect is obtained. The relative movement of the particles is very small at the top of the charge.

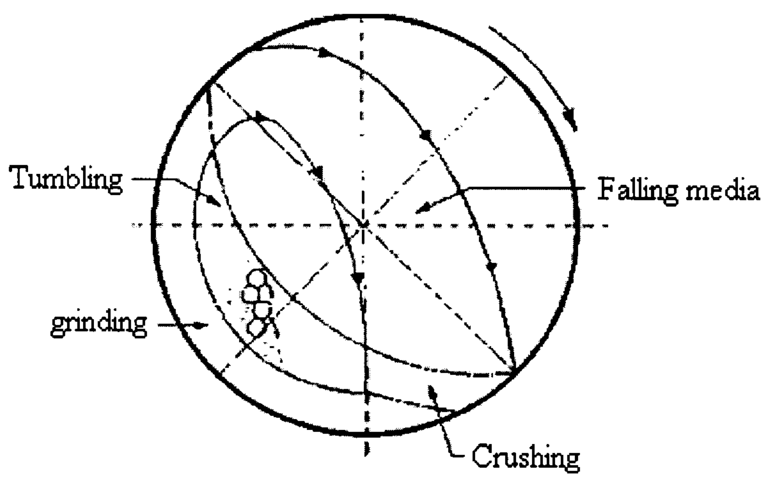

Figure 1.7 Typical ball charge motion profile [9]

The results of grinding operations are strongly dependent on the position of the components of the charge. Best results are achieved when all sizes of balls are uniformly distributed throughout the charge, so that there is a maximum of contact between the particles. Mill speed is a major factor and the lining profile is also vital. If the correct balance between mill speed and lifter bar height is determined, the optimal cascade effect can be generated.

Figure 1.8 shows the balls distribution at selected times. The three-dimensional motion of the charge in a ball mill has been computed for a mill of 5 m diameter and 3 m length. The mill was equipped with 23 lifter bars rotating clockwise at 75% of the critical speed, and filled with 75, 100 and 200 mm spherical particles. The motion of the balls (colored by their velocity magnitude) is shown in the following animation and images. Periodic boundary conditions have been applied at both ends of the ball mill.

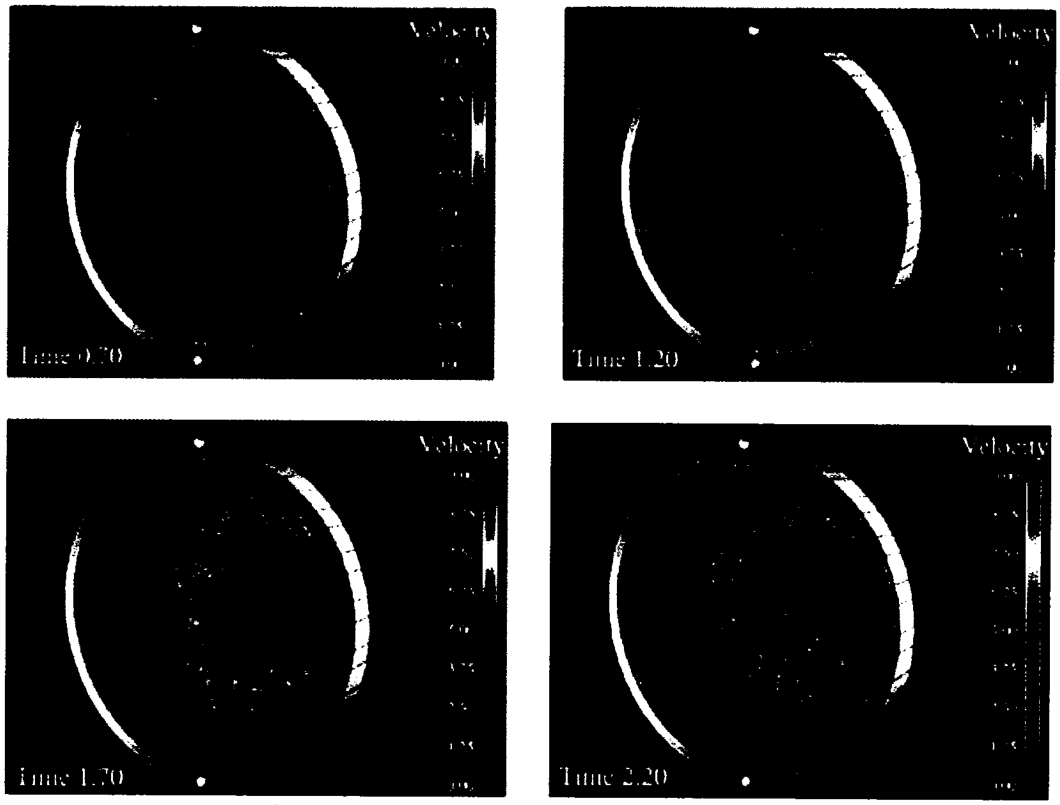

Figure 1.8 Ball distributions at selected times [12]

1.2.2 Instrumentation

Besides simulations, a lot of researchers devoted themselves to experimental research. A major objective of most mill control systems is to stabilize the operation of the mill at a pre-specified operating point selected by the mill operator. Moys developed a technique for measuring the dynamic behavior of the load in the grinding mill. This method involves the monitoring of the response of a conductivity probe mounted in the shell of the mill which gives a measurement of the orientation of the load inside the mill. It was found that the load behavior was strongly influenced by slurry rheology [13]. The relation between power and grinding performance is a complex and non-linear function. Herbst and Rajamani [14] developed the advanced control systems that considerably helped the situation. However, these systems are still lacking in relevant information such as mill load, charge position or slurry properties.

Sensors are a kind of device that can receive a signal or stimulus (as heat or pressure or light or motion etc.) and respond to it in a distinctive manner. They are capable of delivering information inside the mill and therefore are of great value. While the difficulty for a sensor is that the complex motion of a grinding charge is determined by both mill design variables such as liners, lifter profile, discharge mechanism and process operating variables such as solid content, size distribution and slurry viscosity.

Moys, Herbst and Gabardi [15] have done pioneering work in the development of dynamic sensors, conductivity probes, and also in their application to the control of grinding mills. Moys and Montini [16] showed that conductivity measurements can well describe the load behavior and that it is strongly influenced by slurry rheology. Moys [17] stated that the interactions between the slurry, charge and the mill are mainly governed by the slurry viscosity. In an extensive contribution, Shi and Napier-Munn [18] [19] investigated effects of slurry rheology on industrial grinding performance. The results were focused on the overall breakage behavior with a grinding index used as a criterion. It was concluded that slurry viscosity affected grinding performance and that this influence depended on the rheological nature of the slurry. Furthermore, the development of sophisticated data analysis software has opened new possibilities for us to measure mill properties such as sound and vibration [20] and then correlate them with grinding performance calculated from variables measured in the laboratory. In Persson's research, the sensor uses a strain gauge mounted inside a rubber lifter [21]. The sensor can pick up the deflection of the lifter when it moves through the grinding charge, and a characteristic signal profile is obtained. The sensor has been further developed and integrated into a complete measurement system by Dupont and Vien [22]. It is at present marketed by Metso Minerals under the name CCM. The sensor system has been tested on both pilot and full-scale grinding mills under different operating conditions [21] [22]. Results obtained show that there exists a clear correlation between the signal profile and different charge properties such as load volume, angle of charge position expressed as toe and shoulder angle.

1.3 Thesis Objectives and Outlines

From the preceding descriptions, it is clear there is a lot of work being accomplished to describe mill dynamics through simulation and to monitor these dynamics through instrumentation. However, none of the work addresses how these simulation and instrumentation technologies affect the intrinsic behavior of the mechanical system: stress, strain and resonance.

In this thesis, the intrinsic behavior of three major components of a tumbling mill will be addressed by meeting the following objectives through the use of the finite element method:

(i) Analyzing liner bolt stress and strain
(ii) Analyzing liner stresses
(iii) Exploring mill resonance

The development and results of meeting these objectives will be described in separate chapters and each preceded by a review of the finite element method to be used.

CHAPTER 2

REVIEW OF FEA THEORY

This chapter focuses on the review of the related FEA theories that are used in meeting the thesis objectives. The algorithms and the corresponding element types of ANSYS that are used afterwards in static, impact, contact and modal analyses are also reviewed.

2.1 Introduction

The Finite Element Method (FEM) is used to meet the objectives of this thesis. Meeting these objectives requires an understanding of the theoretical foundations of FEM as well as how it is implemented through a specific software to a given application. This chapter aims at giving an adequate description of FEM theory related to static, impact, contact, as well as modal analysis. It will also describe the related element types chosen for use in ANSYS, ANSYS/LS-DYNA the software used in this thesis.

2.2 Static analysis

According to the principle of virtual work, a virtual (very small) change of the internal strain energy must be offset by an identical change in external work due to the applied loads [23] [24]. That is,

$$\delta U = \delta V \tag{2-1}$$

where,

U : strain energy (internal work)

V : external work

δ : virtual operator

After finite element discretization, expression (2-1) can be further written as [23]:

$$\begin{aligned}&\{\delta u\}^T \int_{vol} [B]^T [D][B] d(vol)\{u\} - \{\delta u\}^T \int_{vol} [B]^T [D]\{\varepsilon^{th}\} d(vol) + \{\delta u\}^{T_K} \int_{area_f} [N_n]^T [N_n] d(area_f)\{u\} \\ &= \{\delta u\}^T \rho \int_{vol} [N]^T [N] d(vol) \frac{\delta^2}{\delta t^2}\{u\} + \{\delta u\}^T \int_{area_p} [N_n]^T \{P\} d(area_p) + \{\delta u\}^T \{F_e^{nd}\}\end{aligned} \tag{2-2}$$

where:

vol : volume of element

$[B]$: strain-displacement matrix, based on the element shape functions

$[N_n]$: matrix of shape functions for normal motions at the surface

$[N]$: matrix of shape functions

$\{u\}$: nodal displacement vector

$\{\varepsilon\}$: strain vector

$\{P\}$: the applied pressure vector

$\{F_e^{nd}\}$: nodal force applied to the element

$area_f$: area of the distributed resistance

$area_p$: area over which pressure acts

ρ: density

t: time

δ: virtual operator

Equation (2-2) can also be reduced to:

$$\{[K_e]+[K_e^f]\}\{u\}-\{F_e^{th}\}=[M_e]\{\ddot{u}\}+\{F_e^{pr}\}+\{F_e^{nd}\} \tag{2-3}$$

where:

$[K_e]=\int_{vol}[B]^T[D][B]d(vol)$: element stiffness matrix

$[K_e^f]=k\int_{area_f}[N_n]^T[N_n]d(area_f)$: element foundation stiffness matrix

$\{F_e^{th}\}=\int_{vol}[B]^T[D]\{\varepsilon^{th}\}d(vol)$: element thermal load vector

$[M_e]=\rho\int_{vol}[N]^T[N]d(vol)$: element mass matrix

$\{\ddot{u}\}=\dfrac{\partial^2}{\partial t^2}\{u\}$: acceleration vector

$\{F_e^{pr}\}=\int_{area_p}[N_n]^T\{P\}d(area_p)$: element pressure vector

Equation (2-3) represents the equilibrium equation on a one-element basis.

And the overall equilibrium equations for structural static analysis can be represented by:

$$[K]\{u\} = \{F\} \qquad (2\text{-}4) \quad [23]$$

where:

$[K]$: total stiffness matrix

$\{u\}$: nodal displacement vector

n: number of elements

$[K_e]$: element stiffness matrix

$\{F\}$: load vector

ANSYS FEA structural static analysis is executed in liner bolt analysis (chapter 3) and lifter/liner stress analysis (chapter 4). The models are meshed with SOLID92 and SOLID45 elements. SOLID92 (Figure 2.1 (a)) has a quadratic displacement behavior and is well suited to modal irregular meshes. It has 10 nodes and each node has three degrees of freedom: translations in the nodal x, y, and z directions. The element has plasticity, creep, swelling, stress stiffening, large deflection, and large strain capabilities. SOLID45 (Figure 2.1 (b)) is defined by eight nodes having three degrees of freedom at each node. It also has plasticity, creep, swelling, stress stiffening, large deflection, and large strain capabilities. SOLID45 has another two kinds of options: one is prism option (Figure 2.1 (c)) and the other is tetrahedral option (Figure 2.1 (d)) [23].

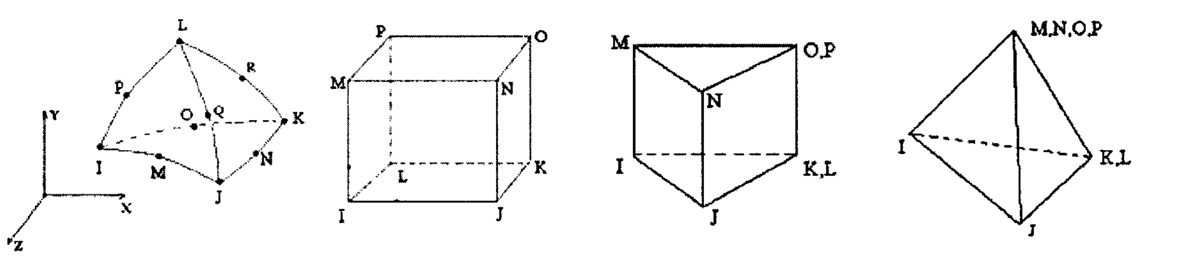

(a) SOLID92 (b) SOLID45 (c) SOLID45 Prism Option (d) SOLID45 Tetrahedral Option

Figure 2.1 SOLID92 and SOLID45 elements [23]

2.3 Impact analysis

ANSYS/LS-DYNA is used in chapter 4 for impact analysis. ANSYS/LS-DYNA provides fast solutions by an explicit method of solution. Since the explicit method can solve the problem in much shorter time then that of the implicit method, it is very useful for complex impact problems. In ANSYS/LS-DYNA, there are two kinds of solid elements that we can use, one is SOLID164 and the other is SOLID168. The SOLID164 element is an 8-node brick element. By default, it uses one point reduced integration plus viscous hourglass control for faster element formulation. SOLID168 element is a higher order 3-D, 10-node explicit dynamic element. One-point integration is advantageous in that it saves computing time and maintains robustness in cases of large deformations. Thus, in this thesis, SOLID164 element type is chosen for generating FE models (see Figure 2.2). SOLID164 also has some simply degenerate shapes such as prism, tetrahedral, and pyramid (see figure 2.3). In these cases, some of the nodes are repeated.

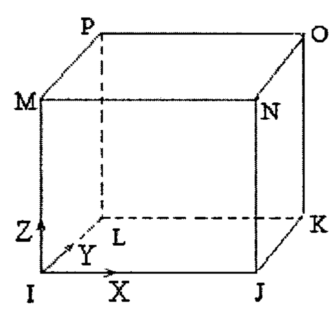

Figure 2.2 SOLID164 element type [23]

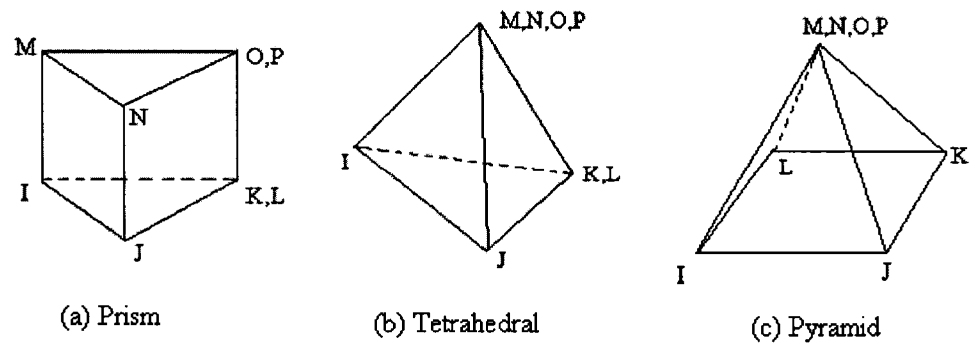

Figure 2.3 SOLID164 degenerate shapes [23]

For a common structural dynamic problem (2-5), ANSYS and ANSYS/LS-DYNA provide two kinds of time integration algorithms: implicit time integration and explicit time integration.

$$[M]\{\ddot{u}\}+[C]\{\dot{u}\}+[K]\{u\}=\{F\} \tag{2-5}$$

In ANSYS implicit time integration, inertia effects of mass and damping ([C] and [M]) are typically not included for implicit time integration. Average acceleration – displacements evaluated at time t+Δt are given by [23]:

$$\{u_{t+\Delta t}\}=[K]^{-1}\{F^{a}_{t+\Delta t}\} \tag{2-6}$$

In ANSYS/LS-DYNA explicit time integration, a central difference time integration method is used. Accelerations are evaluated at time t:

$$\{a_t\}=[M]^{-1}(\{F_t^{ext}\}-\{F_t^{\text{int}}\}) \tag{2-7}$$

where $\{F_t^{ext}\}$ is the applied external and body force and $\{F_t^{\text{int}}\}$ is the internal force vector.

The velocities and displacements are then evaluated:

$$\{v_{t+\Delta t/2}\}=\{v_{t-\Delta t/2}\}+\{a_t\}\Delta t_t \tag{2-8}$$

$$\{u_{t+\Delta t}\}=\{u_t\}+\{v_{t+\Delta t/2}\}\Delta t_{t+\Delta t/2} \tag{2-9}$$

The geometry is updated by adding the displacement increments to the initial geometry $\{X_0\}$:

$$\{X_{t+\Delta t}\}=\{X_0\}+\{u_{t+\Delta t}\} \tag{2-10}$$

The problem of friction cannot be avoided when we investigate the charge impact force. The frictional coefficient used for contact is determined from the static friction coefficient (*FS*), the dynamic friction coefficient (*FD*), and the exponential decay coefficient (*DC*).

The frictional coefficient μ_c is assumed to be dependent on the relative velocity, V_{rel}, of the surfaces in contact: [23]

$$\mu_c = FD + (FS - FD)e^{-DC \cdot V_{rel}} \tag{2-11}$$

In the following calculations, a *FS* of 0.45 is used between the mill and the charge. Since we have no corresponding experiment to decide *FD*, we just consider *FD* is the same as *FS* and *DC* is ignored. The coefficient for viscous friction *VC* can be used to limit the friction force to a maximum. A limiting force is computed:

$$F_{\lim} = VC \cdot A_{cont} \tag{2-12}$$

where A_{cont} is the area of the segment contacted by the node in contact. The suggested value for *VC* is to use the yield stress in shear:

$$VC = \frac{\sigma_0}{\sqrt{3}} \tag{2-13}$$

where σ_0 is the yield stress of the contacted material.

In order to avoid undesirable oscillation in contact, a contact damping perpendicular to the contacting surfaces is applied. The contact damping coefficient is calculated as:

$$\xi = \frac{VDC}{100} \cdot \xi_{crit} \tag{2-14}$$

VDC is the viscous damping coefficient. ξ_{crit} is determined in the following fashion by ANSYS/LS-DYNA:

$$\xi_{crit} = 2m\omega \tag{2-15}$$

and:

$$m = \min(m_{slave}, m_{master}) \tag{2-16}$$

$$\omega = \sqrt{K \cdot \frac{m_{slave} + m_{master}}{m_{slave} \cdot m_{master}}} \tag{2-17}$$

where:

K: interface stiffness

m: mass

2.4 Contact analysis

Contact problems exist in the analyses of chapter 3 and chapter 4. ANSYS contact module is used in chapter 3 and both the ANSYS contact module and the ANSYS/LS-DYNA contact module are used in chapter 4.

ANSYS provides three kinds of contact capabilities: surface-to-surface contact, node-to-surface contact, and node-to-node contact. Since the surface-to-surface contact elements are well suited for applications such as interference fit assembly contact or entry contact, forging, and deep-drawing problems, they are used in the current work. ANSYS supports both rigid-to-flexible and flexible-to-flexible surface-to-surface contact elements. These contact elements use a "target surface" and a "contact surface" to form a contact pair. Since the charges and the mill are all deformable, so the flexible-to-flexible surface-to-surface contact element type is chosen to mesh the contact bodies. The contact body is meshed with CONTA173 elements and the target body is meshed with TARGE170.

For the ANSYS/LS-DYNA contact type, single surface contact is established for the FE model in this thesis. Single surface contact applies to when a surface of one body contacts itself or the surface of another body. In single surface contact, the ANSYS/LS-DYNA program automatically determines which surfaces within a model may come into contact. When it is defined, single surface contact allows all external surfaces within a model to come into contact. This option can be very powerful for self-contact or large deformation problems when general areas of contact are not known beforehand. Unlike implicit modeling, where over-defining contact will significantly increase computation time, using single surface contact in an explicit analysis will cause only minor increases in CPU time. Since automatic general (AG) contact is very robust, it is suitable for self- contact and large deformation problems when the contact conditions are not easy to predict.

The stiffness relationship between two bodies must be established for contact to occur. Without contact stiffness, bodies will pass through one another. The relationship is generated through an 'elastic spring' that is put between the two bodies, where the contact force is equal to the product of the contact stiffness (k) and the penetration (δ). The amount of penetration (δ) between the two bodies is therefore dependent on the stiffness k. The value of k that is used depends on the relative stiffness of the bodies in contact. In the ANSYS/LS-DYNA program, the contact stiffness is determined by the following relationships [23]:

$$k = \frac{f_s \times Area^2 \times K}{Volume} \quad \text{for segments on solid elements} \tag{2-18}$$

$$k = \frac{f_s \times Area \times K}{MinimumDiagonal} \quad \text{for segments on shell elements} \tag{2-19}$$

where:

Area:	area of contact segment
K:	bulk modulus of contacted element
f_s:	penalty factor (0.1 by default)
Volume:	volume of the solid elements
MinimumDiagonal:	minimum diagonal of the segments on shell elements

2.5 Modal analysis

For a typical undamped modal analysis eigenvalue problem (2-20), many numerical methods are available to solve it.

$$[K]\{\phi_i\} = \omega^2[M]\{\phi_i\} \tag{2-20}$$

where:

$[K]$:	stiffness matrix
$\{\phi_i\}$:	mode shape vector of mode i
$[M]$:	mass matrix
ω:	eigenvalue

In ANSYS, seven methods are offered [23]:

- Block Lanczos method
- Subspace method
- PowerDynamics method
- Reduced (Householder) method
- Unsymmetric method
- Damped method
- QR damped method

In the present work, the Block Lanczos method is used in modal analysis. The Block Lanczos method uses the sparse matrix solver. It is a variation of the Lanczos procedure. In Block Lanczos, instead of using a single vector, a block of vectors are used to perform Lanczos recursions. In addition, the block algorithms are generally more robust and efficient for matrices with multiple or closely clustered eigenvalues.

The vibration of a spinning body will cause relative circumferential motions, which will change the direction of the centrifugal load which, in turn, will tend to destabilize the structure. As a small deflection analysis cannot directly account for changes in geometry, the effect can be accounted for by an adjustment of the stiffness matrix, called spin softening. [23] When the spin softening is considered, the eigen equation becomes:

$$|([K]-\omega_s^2[M])-\omega^2[M]|=0 \qquad (2\text{-}21)$$

Where :

$[K]$: stiff matrix

ω_s: angular velocity of rotation

ω: natural circular frequencies of the rotating body

$[M]$: mass matrix

Tumbling mills have some similarity to circular cylinders by having cylindrical chambers. For hollow and circular cylinders, when vibrating with circumferential vibration wave numbers m=0, 1, 2, they have the following mode shapes as showed in Figure 2.4.

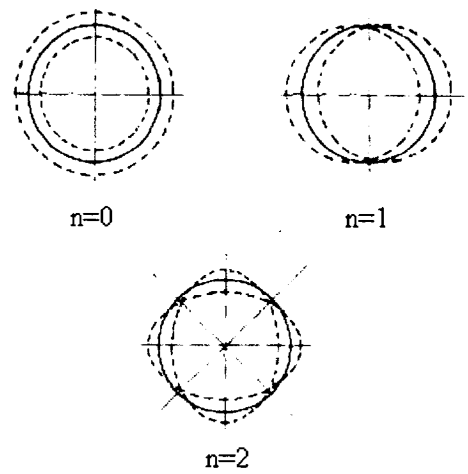

Figure 2.4 Circumferential vibration forms [25]

Regarding the tumbling mills, if we treat them as all-free-end cylindrical tubes (without considering the caps), the mode shapes at m=2, 3, 4 are shown in Figure 2.5, Figure 2.6, and Figure 2.7. In these figures, the different colors represent different stress (mises stress) ranges.

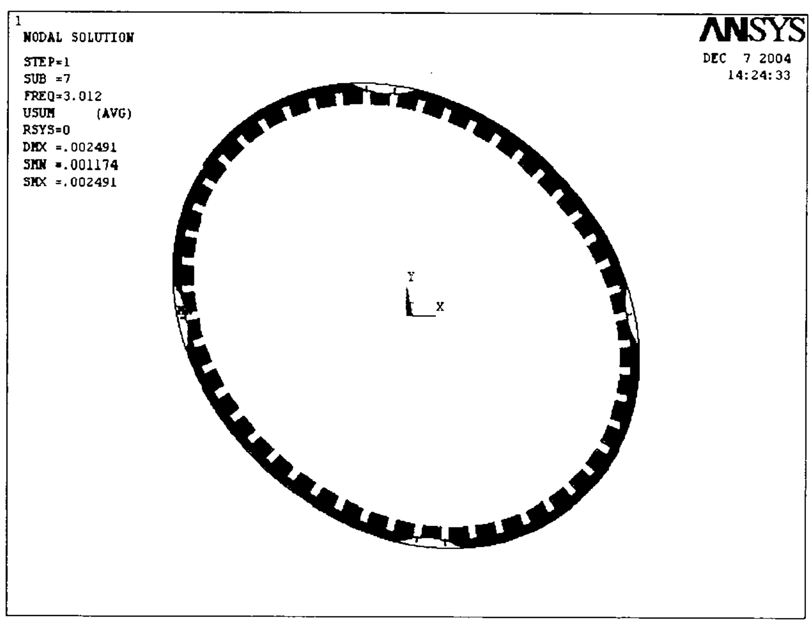

Figure 2.5 Mode shape of all-free-end cylindrical mill tube at m=2

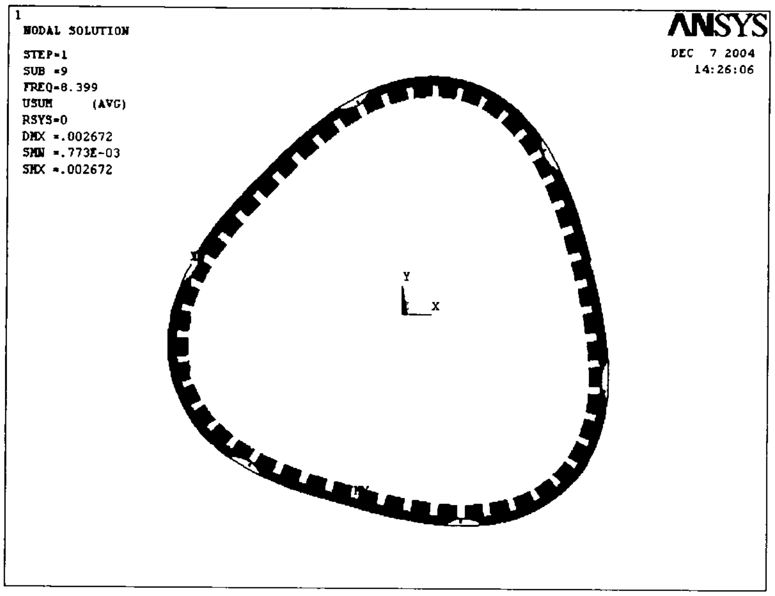

Figure 2.6 Mode shape of all-free-end cylindrical mill tube at m=3

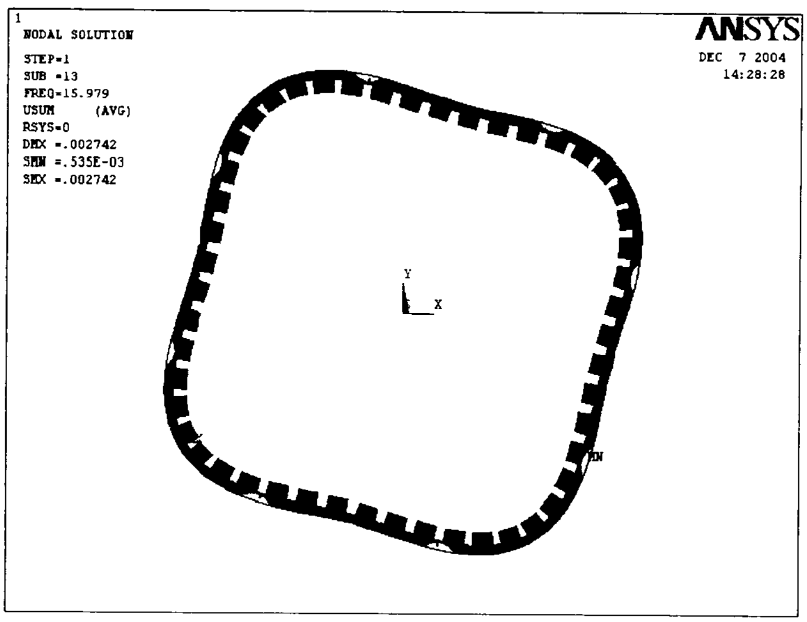

Figure 2.7 Mode shape of all-free-end cylindrical mill tube at m=4

Boundary conditions also have great influence on the mode shape. For the above cylindrical mill tube, if the all-free-end boundary conditions are replaced by all-fixed-end boundary conditions, the mode shapes at m=3, 4 are shown in Figure 2.8 and Figure 2.9.

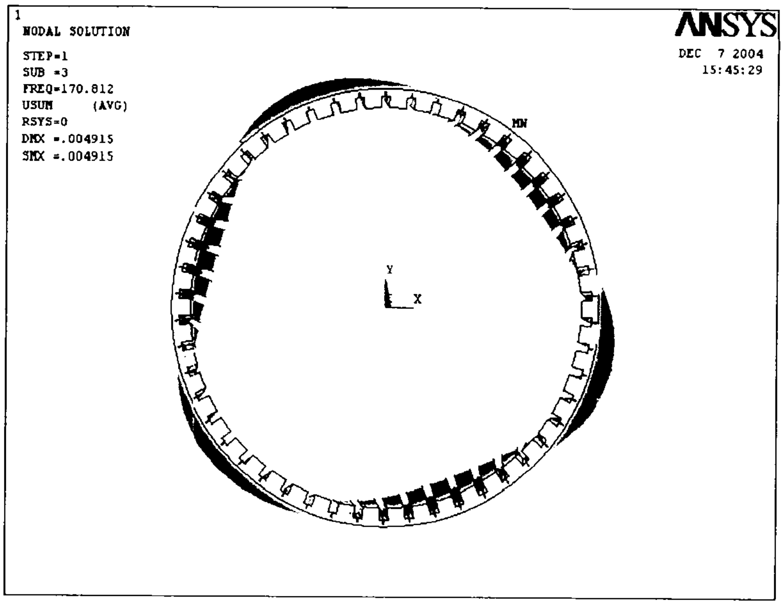

Figure 2.8 Mode shape of all-fixed-end cylindrical mill tube at m=3

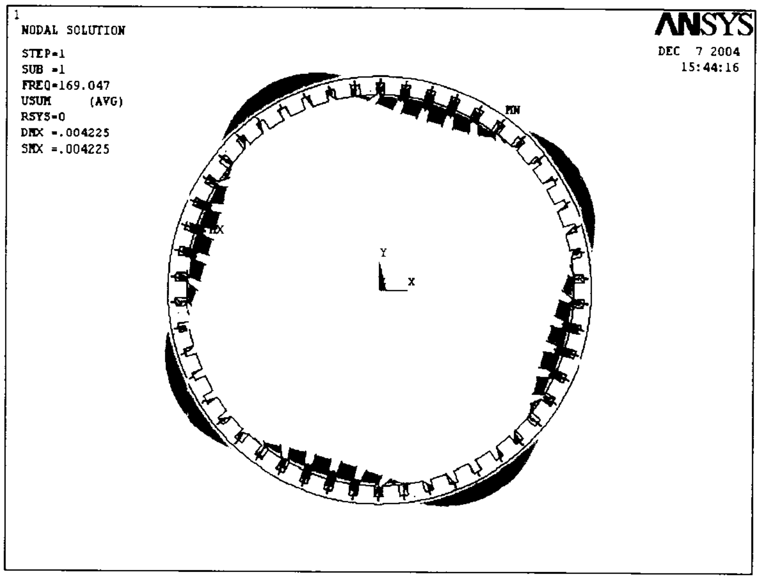

Figure 2.9 Mode shape of all-fixed-end cylindrical mill tube at m=4

2.6 Conclusions

Previous review provides us the detailed FEA bases on which the following analyses are based. In the following chapters, these FEA theories are used separately or combined and will be identified in the "introduction" part.

CHAPTER 3

LINER BOLT ANALYSIS

Liner bolts are very important parts of tumbling mills. They connect the inner side of the mill (the liners), and the outer side of the mill (the shell). In mill operating conditions, at different angles along the mill circumferential direction, bolts have different stress and strain distributions accordingly. The aim of this chapter is to investigate the bolts' stress and strain distributions at different mill positions, so as to explore the possibility of using the stress and strain distributions inside the bolts as a tool to decide the toe angle and shoulder angle, which can be further utilized to predict the charge profile inside the mills.

3.1 Introduction

The inner peripheral surface of the tumbling mills works in very hostile working environment. It is always subjected to the continuous impacts and abrasions coming from the ore. To control the movement of the ore inside the mill and to protect the steel shell against abrasion, wear-resistant shell liners are mounted onto the inner peripheral surface. Tumbling mills have plurality of longitudinal metal liners and each liner has one or more segments. Each segment is tightly fastened with mill shell by bolts shown in Figure 3.1. Bolted parts are held together by the clamping force which is produced by slightly stretching the connecting bolt. If there are no other forces acting on the bolt and the bolted parts, to properly tighten the bolted parts, this clamping force must be greater than the opposing force that is trying to pull the parts apart. When bolts are tightened they become stressed in tension. As long as the sum of the tensile load plus the opposing force does not exceed the yield strength of the bolt, it will return to its original length when the bolt is loosened and those forces are removed. If the total tensile load exceeds the yield strength, the bolt will have permanent deformation. When this happens the bolt is weakened and is no longer suitable for the same use.

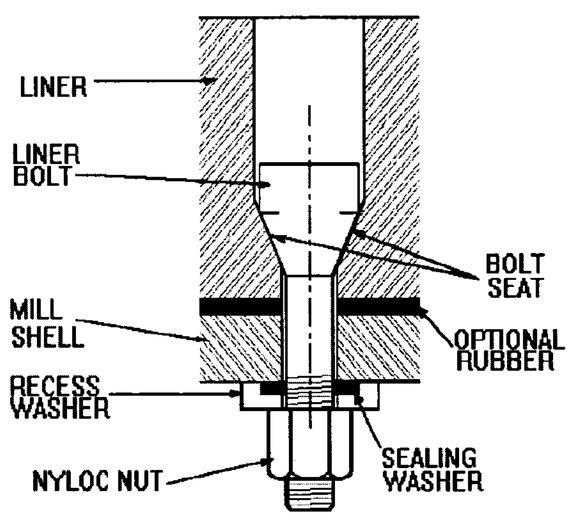

Figure 3.1 Mill liner bolt [26]

Bolts are very useful for investigating and controlling charge motion. Steven Spencer [27] developed an automated signal analysis system for source event location and characterization based on multiple-sensor surface vibration monitoring of tumbling mills. In his research, surface vibration data is simultaneously acquired by means of three piezoelectric accelerometers, which are mounted in a triangular array on the liner/lifter bolts of the rotating mill outer shell and coupled to analogue radio transmitters/receivers. Such a system can provide insights into both the efficiency of the grinding process and the propensity for liner wear as a function of mill operating conditions. Other researchers such as Herbst et al [28], Vermeulen and Schakowski [29] also made great efforts to utilize lifter bolts or lifter to measure the forces acting inside of the mill. Techniques that measure the force acting on the lifter or a lifter bolt have sparked an increased interest recently because of the ability to combine it with DEM modeling. Process Engineering Resources Inc. (PERI) markets a unit called CVM - Continuous Volume Measurement, and this uses the relaxation in strain in an instrumented lifter washer or bolt to infer the normal forces on the lifter [21].

In this chapter, a detailed lifter, liner, bolt and mill shell FEA model is established so as to analyze the stress and strain distributions of the bolts, bolt holes, liners and lifters at different positions. The results are very useful for exploring new sensor-using methods aimed at investigating the charge motion inside the mill.

3.2 Charge Profile

In order to consider the influence of the charge action inside the mill, Radziszewski's Charge Motion Simulator is used in the present work to get the charge profile at a certain charge motion state. Three kinds of charge volume level 25%, 30%, 35% are considered in this paper. (As shown in Figure 3.2, Figure 3.3, and Figure 3.4)

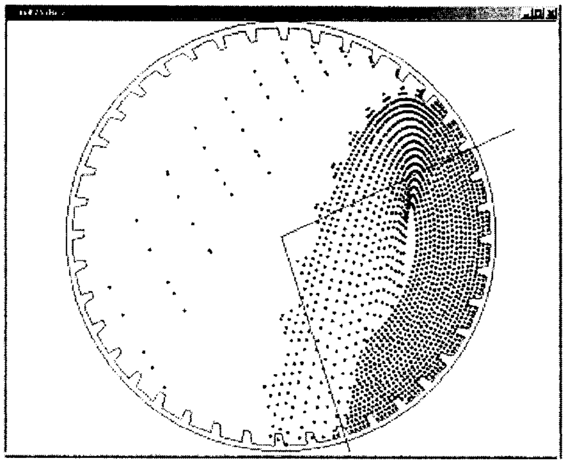

Figure 3.2 Charge profile of 25% charge volume

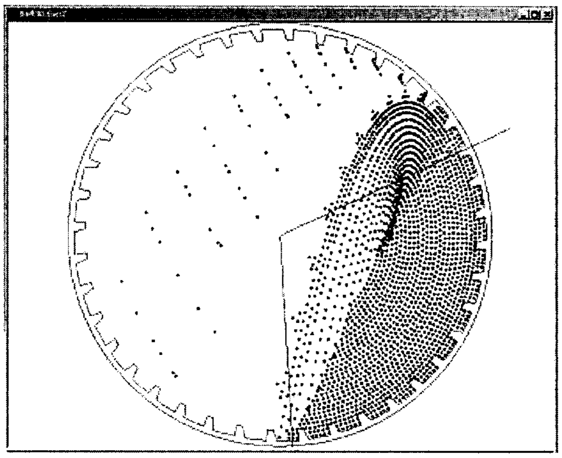

Figure 3.3 Charge profile of 30% charge volume

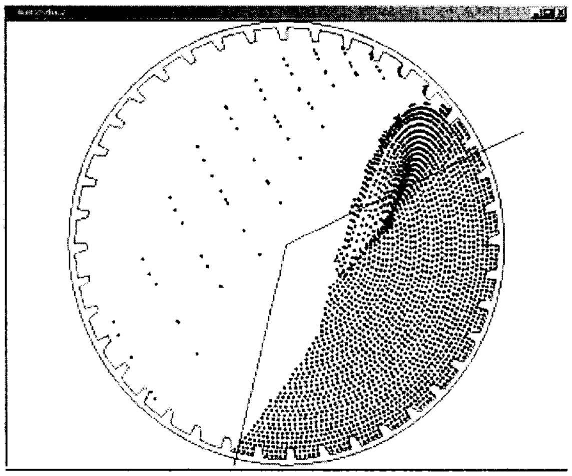

Figure 3.4 Charge profile of 35% charge volume

3.3 Boundary Conditions

According to the charge profiles shown above, the gravity and centrifugal force coming from the charge acting on the mill can be calculated. To calculate the gravity force, in the cross section of the mill, the whole charge profile area is divided into small sub areas where each liner matches one piece of area (see Figure 3.5). Here, we suppose that along the mill chamber axial direction, each mill cross section has the same charge profile. Then the gravity force on the surfaces of the liners/lifters can be easily applied by calculating the gravity force of each sub area.

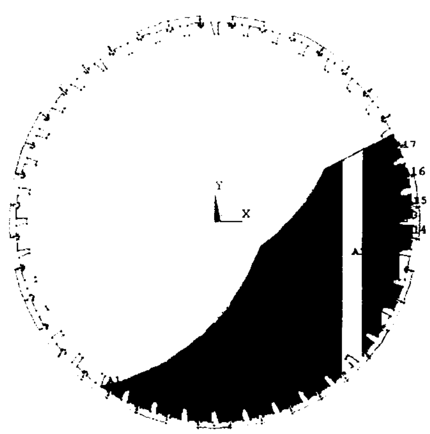

Figure 3.5 Gravity calculation

The centrifugal force is applied and calculated in the similar way as mentioned above (Figure 3.6). The difference is that the areas are divided along the mill rotating angle direction according to the radial direction property of centrifugal force.

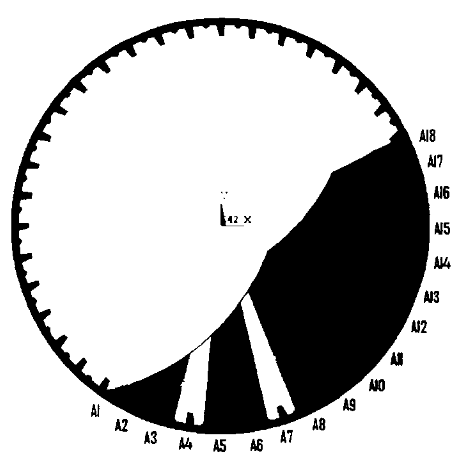

Figure 3.6 Centrifugal force calculation

3.4 Bolt Preload

Bolt pretension, also called preload or pre-stress, comes from the installation torque (T) applied by tightening the bolt. Torque applied is only an indicator of that preload. Because of many variables, there is no formula, method, or device that guarantees applying a certain torque will develop a precise and uniform bolt preload. The value of torque applied on the bolt should depend both upon the bolt's diameter and its grade. Of the torque applied, 50% overcomes friction between the nut or bolt head and joint surface and 40% overcomes friction between mating threads. Only 10% develops useful tension or preload in the bolt [30]. From the above number, it is very clear that the coefficient of friction has a great effect upon the preload. The Friction can be reduced by lubrication and attention to protecting threads during storage and use, replacing bolts with damaged threads, and placing hardened washers under the nut head. Theoretically, we'll get the greatest strength from a given bolt by tightening it exactly to the yield point. In general, to provide a margin of safety, bolt preload is specified between 75% and 100% of bolt proof strength, with 80%-90% being common [30] [31]. Bolt proof strength is the maximum tensile stress the bolt material can withstand without encountering permanent deformation. The working environment of the bolt should also be considered when applying the preload. On the one hand, the material property of the bolt is related to the environment. For example, heat will lower the yield strength (and proof strength) of a fastener. On the other hand, the working load acting on the bolt and the bolted parts cannot be neglected since it will influence the stress inside the bolt. There are many ways to measure the bolt preload. The common methods are: torque wrench, part turn of nuts, direct tension indicators, strain gauge, ultrasonic instruments, etc.

The initial tension in a bolt can be crudely estimated for a bolt tightened by hand with an experienced mechanic as follows [32]

$$F_p = k \cdot d \tag{3-1}$$

- d = nominal diameter of bolt (m)
- F_p = Preload (N)

- k = Coefficient vary from 1.75 x 10^6 N/m to 2.8 x 10^6 N /m

Torque coefficient k is a function of thread geometry, thread coefficient of friction, and collar coefficient of friction. Specified k needs to be chosen, depending on specific thread interface, collar (bolt head or nut annulus) interface materials, surface condition, and lubricant.

For a bolt tightened with a torque wrench the torque required to provide an initial bolt tension may be approximated by the formula.

$$T = F_p \cdot K \cdot d \tag{3-2}$$

Steel thread condition	K
Stainless on mild or alloy	0.3
Mild or alloy on same	0.2
Cadmium plated	0.18
Molybdenum-disulphide grease	0.14
PTFE lubrication	0.12

Table 3.1 Typical K factors

A more accurate value can be determined using the formula [32]

$$T = \frac{F_P \cdot d_m}{2}\left(\frac{p + \pi \cdot \mu \cdot d_m \sec(\alpha)}{\pi \cdot d_m - \mu \cdot p \cdot \sec(\alpha)}\right) + F_p \cdot \mu_c \cdot r_c \tag{3-3}$$

where

F_p : Desired bolt Preload (N)

P: Thread pitch (m)

d_m : Mean diameter of thread (m)

μ : Coefficient of Thread friction

μ_c: Coefficient of collar friction

2α: The thread angle

r_c: Collar friction radius (m)

In this chapter, the bolt preload is measured by torque measure. The torque is 6500 ft-lb. Then the bolt tension force can be calculated using:

$$T = 0.2 \cdot d \cdot F \tag{3-4}$$

where :

T: torque

d: Nominal bolt diamanter

F: Bolt tension force

3.5 FE Mill Model

In this part of analysis, only the FE model of tumbling mill chamber is generated. The mill is modeled by solid45 elements. In Figure 3.7, different liners are shown in different colors and the outer mill shell is shown in red.

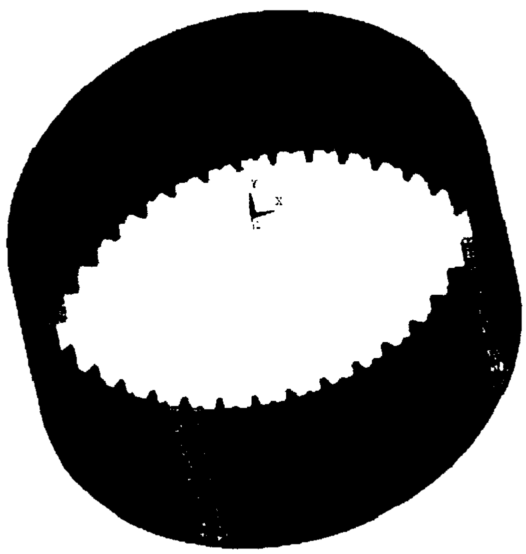

Figure 3.7 FEA model of the mill

3.6 Simulation Results

The simulation results are analyzed based on cylindrical system. The cylindrical system is defined in Figure 3.8 according to ANSYS.

Another two terms, toe position and shoulder position, are frequently mentioned below. Figure 3.9 illustrates these two positions.

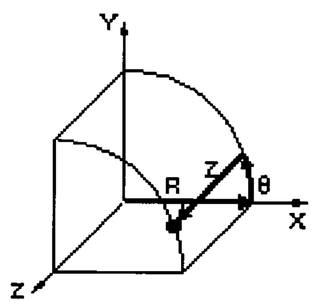

Figure 3.8 Cylindrical system [23]

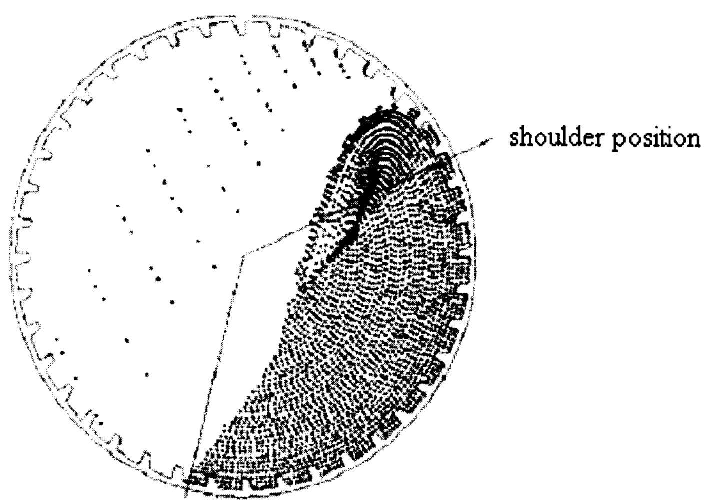

Figure 3.9 Toe position and shoulder position [9]

In order to clarify the discipline of how the strain and stress around the bolt area alter along the circumference of the mill, we compared the average strain and stress at the top, middle and bottom surfaces of the edges of the bolt holes separately. The top, middle, and bottom surfaces are defined as: (1) the top surface refers to the top surface of the bolt hole whose normal direction is pointing to the center of the mill; (2) the middle surface refers to the surface that lies on the intersection surface between the liner and the mill shell; (3) the bottom surface refers to the bottom surface of the bolt hole whose normal direction is pointing opposite to the center of the mill. And the strain/stress of each surface is the average value of all nodes on the edge of the hole at that surface. The unit for stress is N/m^2. In the present work, we compared 3 different bolt positions, that is, lifter bolts which lie in the lifters; right liner bolts which lie in the liners located at the right side of the lifter bolts; and left liner bolts which lie in the liners located at the left side of the lifter bolts. The bolt position (1 to 20) of lifter, right liner, and left liner is defined in Figure 3.10.

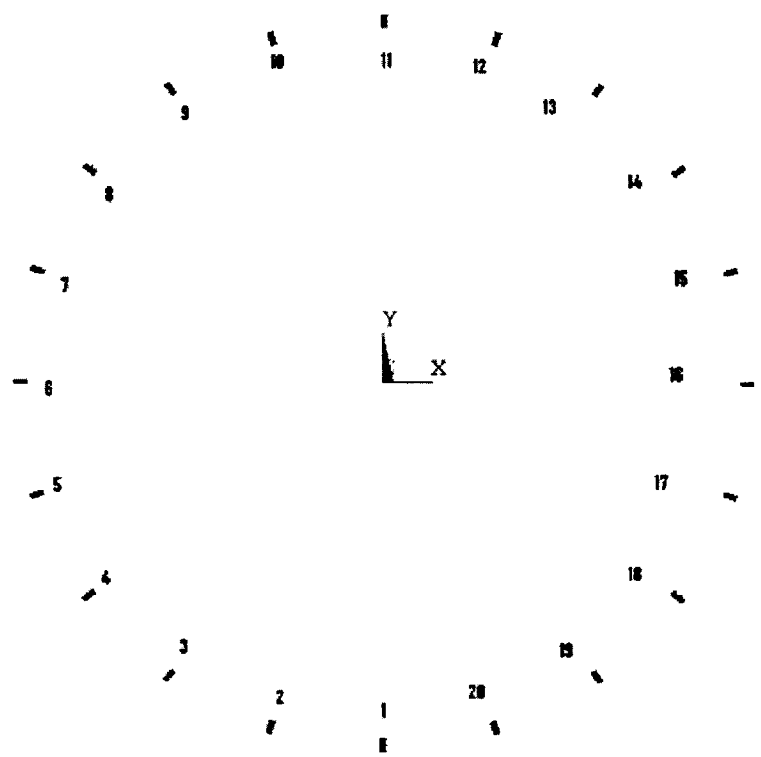

Figure 3.10 Bolt position

Figure 3.11 to Figure 3.16 illustrate the strain distributions of the three different surfaces of the lifter bolt holes in r and θ direction of cylindrical system. In the figures, the horizontal axes represent the bolt positions defined by the above figure; the vertical axes represent the strain values. Among them, Figure 3.11 and Figure 3.12 are for the top surfaces of the lifter bolt holes; Figure 3.13 and Figure 3.14 are for the middle surfaces of the lifter bolt holes; Figure 3.15 and Figure 3.16 are for the bottom surfaces of the lifter bolt holes.

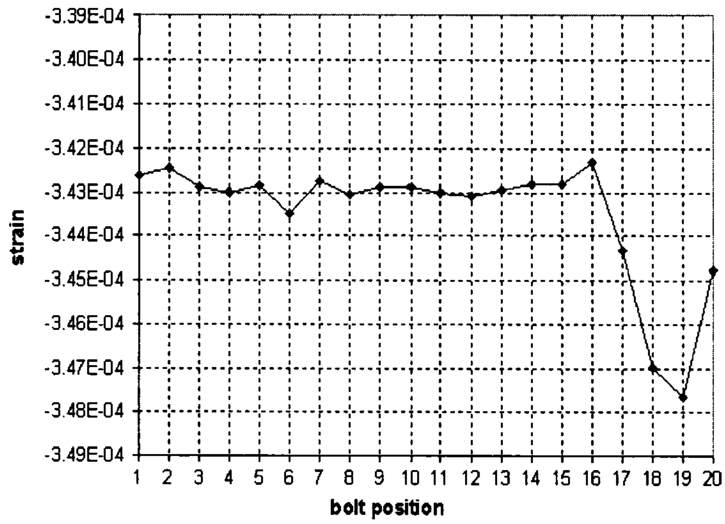

Figure 3.11 Average strains in r direction of the top surfaces of lifter bolt holes

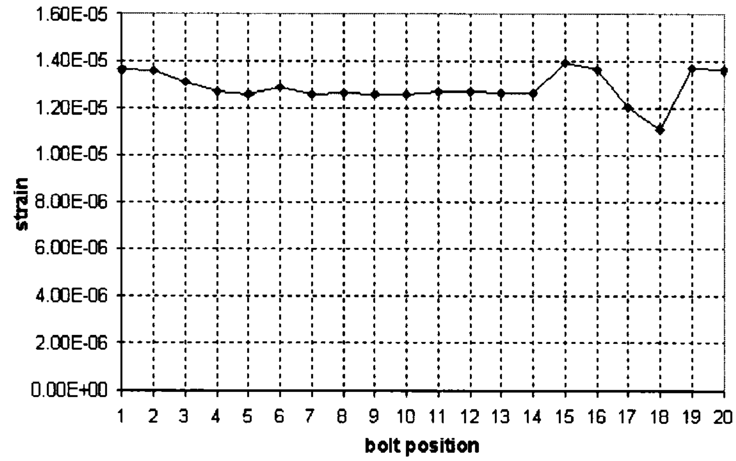

Figure 3.12 Average strains in θ direction of the top surfaces of lifter bolt holes

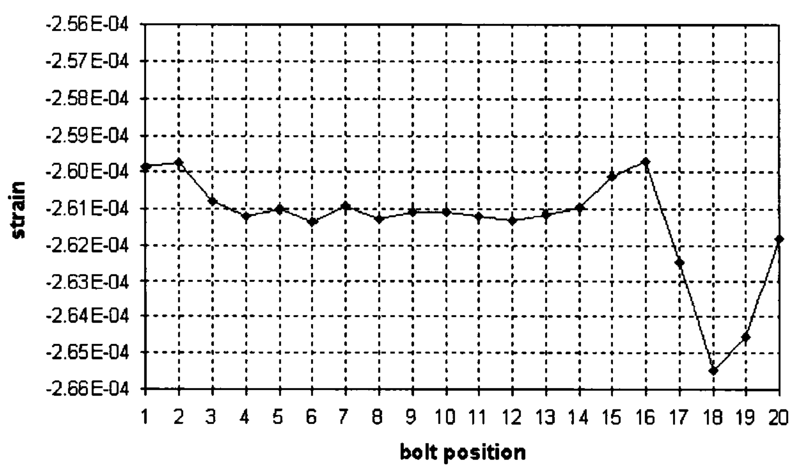

Figure 3.13 Average strains in r direction of the middle surfaces of lifter bolt holes

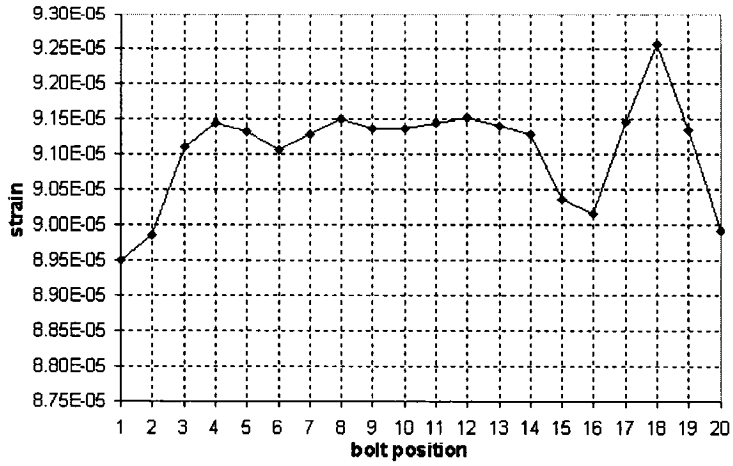

Figure 3.14 Average strains in θ direction of the middle surfaces of lifter bolt holes

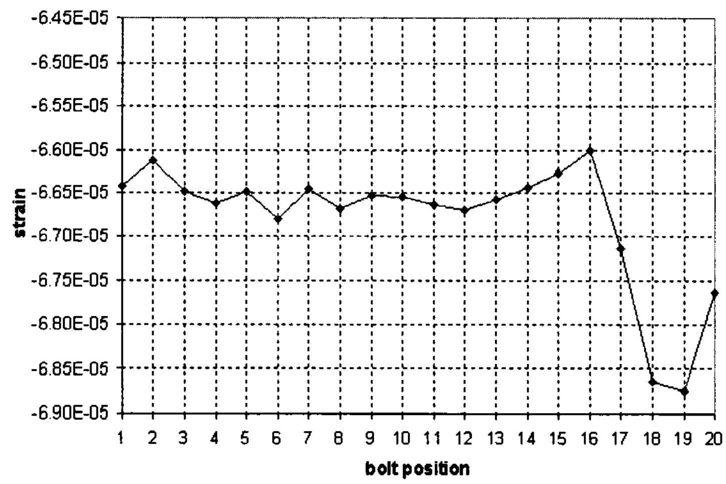

Figure 3.15 Average strains in r direction of the bottom surfaces of lifter bolt holes

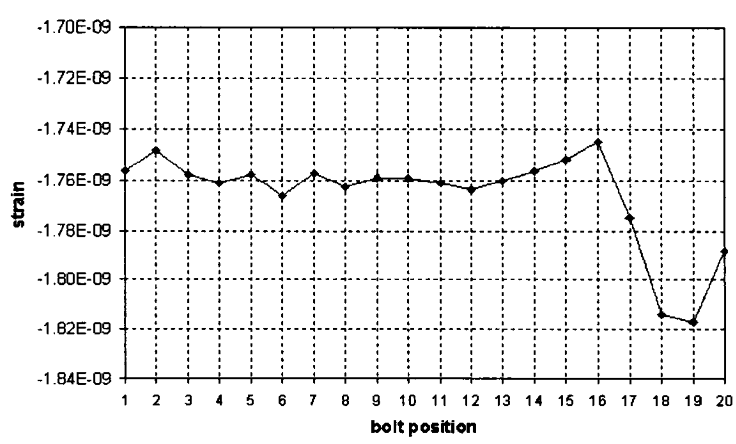

Figure 3.16 Average strains in θ direction of the bottom surfaces of lifter bolt holes

From the results of lifter bolt holes shown above, we can draw the following conclusions:

(1) Between bolt positions 3 to bolt position 14, the values of strains are almost the same or just have a little difference. From the bolt position definition in Figure 3.10, we know that the zone of the mill located between bolt position 3 and 13 is free of ore's action.

(2) The maximum strains (absolute value) occur at around bolt position 18 or 19. This position is where the mill affords the maximum force coming from ore.

(3) Bolt position 6 is almost opposite to the maximum force enduring position of the mill. Under the ore action, the mill itself will have a deformation tendency that goes along the bottom right direction. Being a united cylinder, the top right side has a tendency to go the other side. In that case, the bolt at position 6 has a little higher strain value (absolute value) than its neighbor bolts.

Figure 3.17 to Figure 3.22 illustrate the average strain distributions of the three different surfaces of the left liner bolt holes in r and θ direction of cylindrical system. In the figures, the horizontal axes represent the bolt positions defined by Figure 3.10; the vertical axes represent the strain values. Among them, Figure 3.17 and Figure 3.18 are for the top surfaces; Figure 3.19 and Figure 3.20 are for the middle surfaces; Figure 3.21 and Figure 3.22 are for the bottom surfaces.

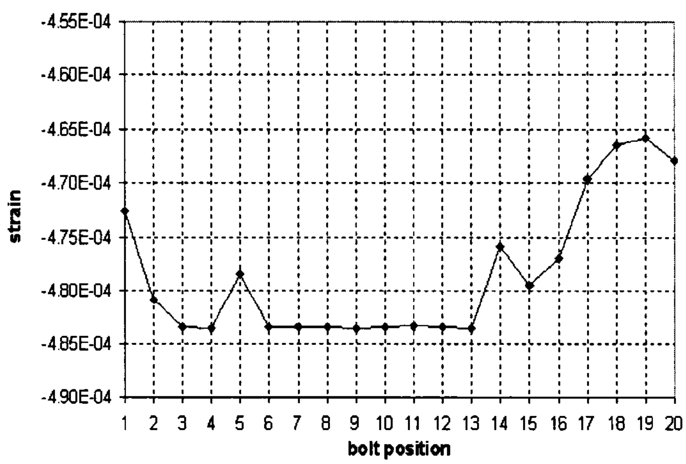

Figure 3.17 Average strains in r direction of the top surface of left liner bolt holes

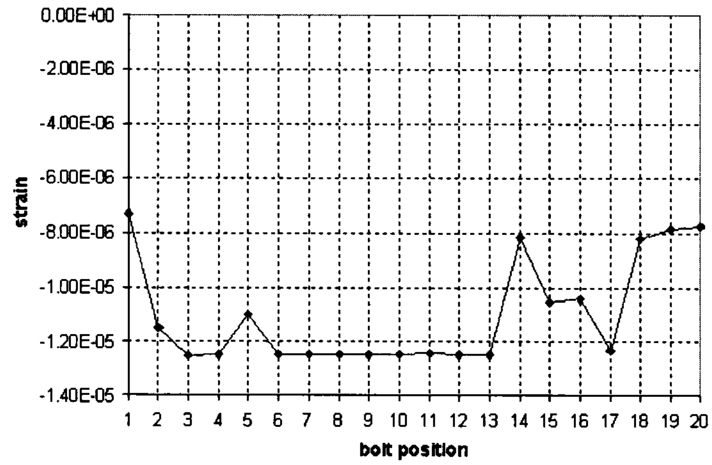

Figure 3.18 Average strains in θ direction of the top surfaces of the left liner bolt holes

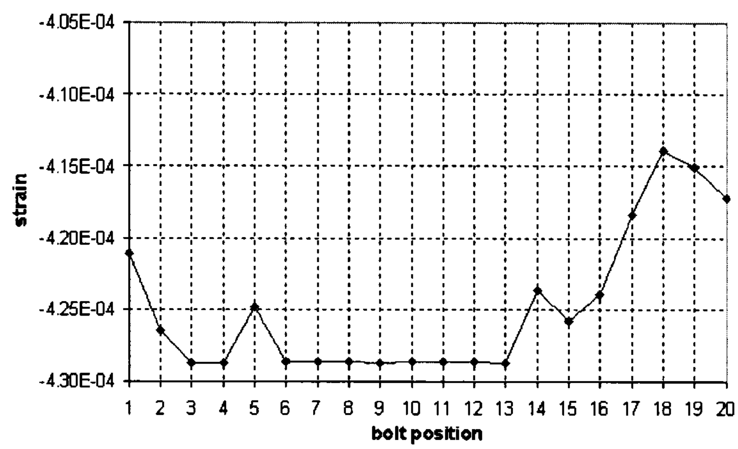

Figure 3.19 Average strains in r direction of the middle surfaces of the left liner bolt holes

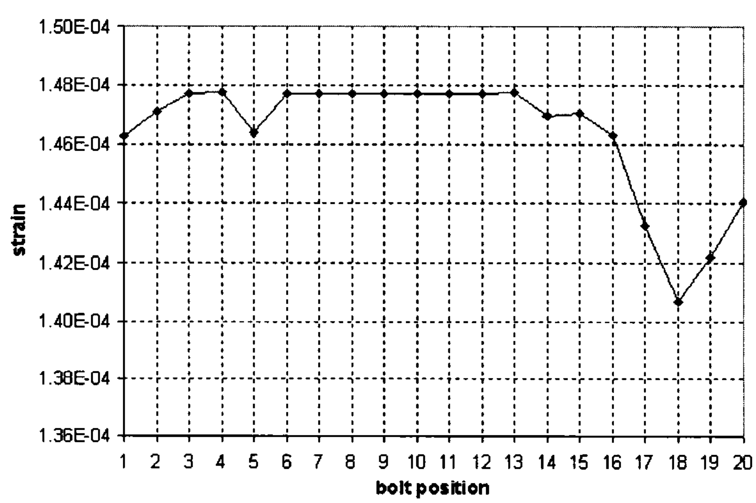

Figure 3.20 Average strains in θ direction of the middle surfaces of the left liner bolt holes

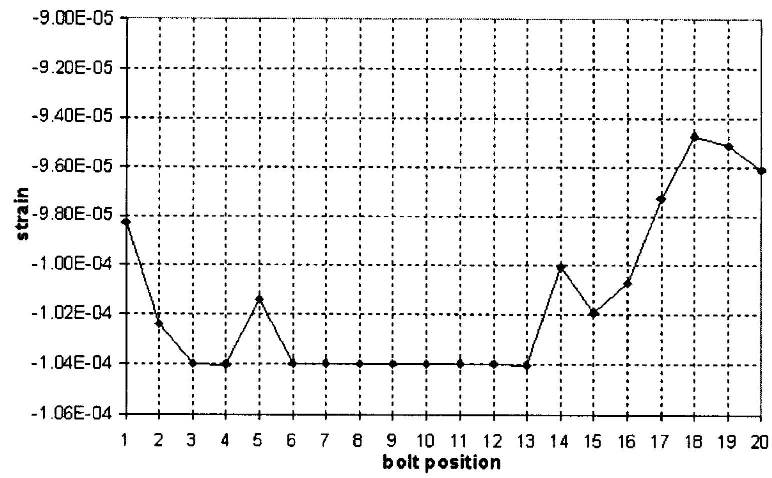

Figure 3.21 Average strains in r direction of the bottom surfaces of the left liner bolt holes

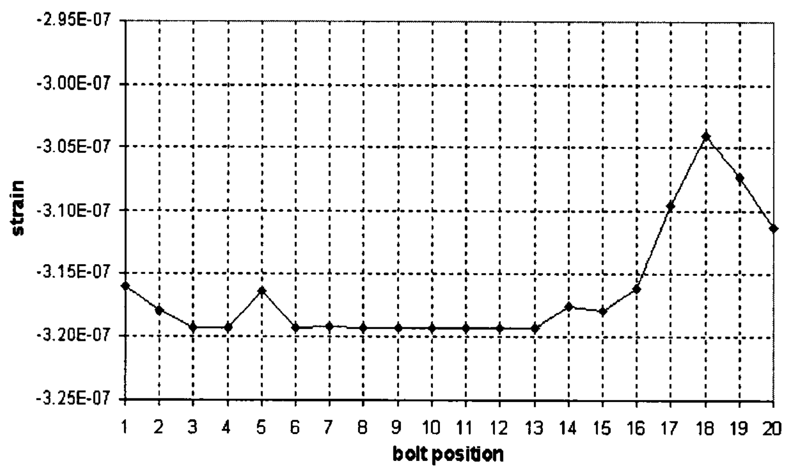

Figure 3.22 Average strains in θ direction of the bottom surfaces of the left liner bolt holes

From the results of left liner bolt holes shown above, we can draw the following conclusions:

(1) Between bolt positions 3 to bolt position 13, the values of strains are almost the same or just have a little difference except bolt position 5. From the bolt position definition in Figure 3.10, we know that the zone of the mill located between bolt position 3 and 13 is free of ore's action.

(2) The maximum strains (absolute value) occur at around bolt position 18. This position is also where the mill affords the maximum force coming from ore.

(3) Stain values at bolt position 5 have a little difference compared to its neighbors. The reason is the same as that mentioned in the conclusion (3) of page 40.

Figure 3.23 to Figure 3.28 illustrate the strain distributions of the three different surfaces of the right liner bolt holes in r and θ direction of the cylindrical system. In the figures, the horizontal axes represent the bolt positions defined by above figures; the vertical axes represent the strain values. Among them, Figure 3.23 and Figure 3.24 are for the top surfaces; Figure 3.25 and Figure 3.26 are for the middle surfaces; Figure 3.27 and Figure 3.28 are for the bottom surfaces.

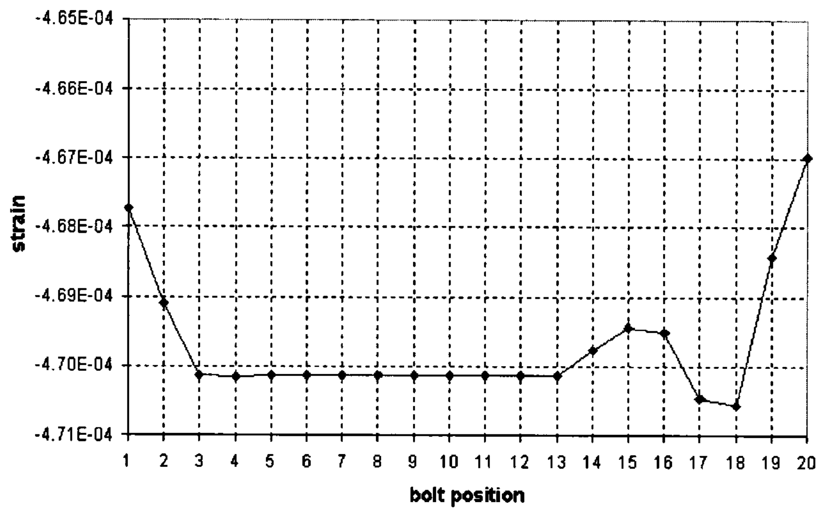

Figure 3.23 Average strains in r direction of the top surfaces of the right liner bolt holes

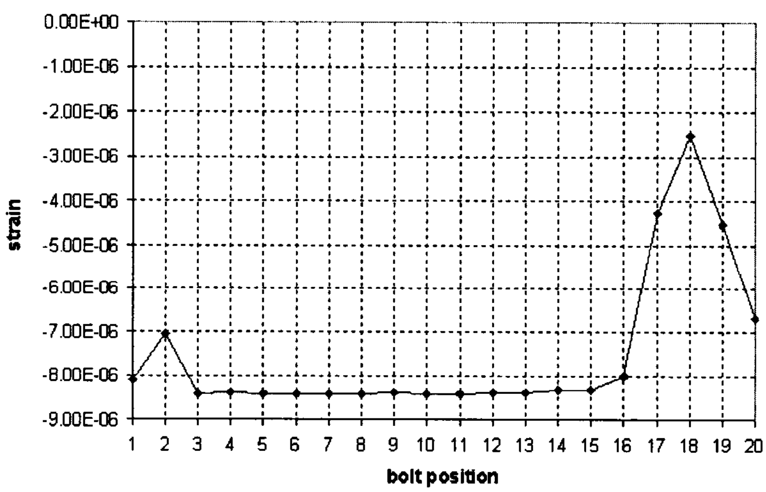

Figure 3.24 Average strains in θ direction of the top surfaces of the right liner bolt holes

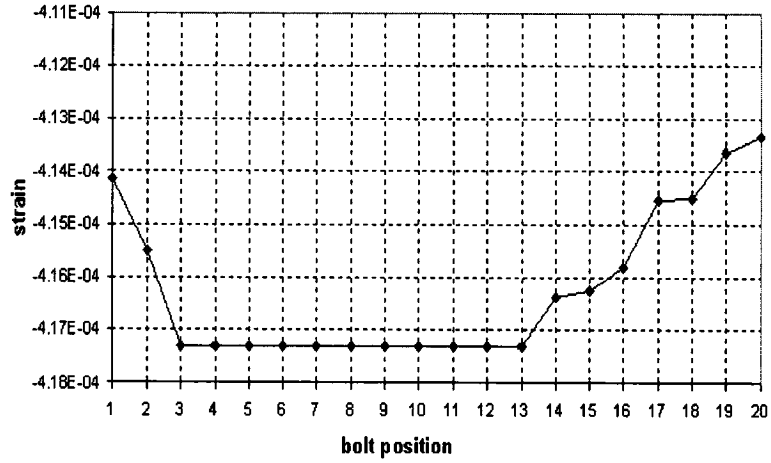

Figure 3.25 Average strains in r direction of the middle surfaces of right liner bolt holes

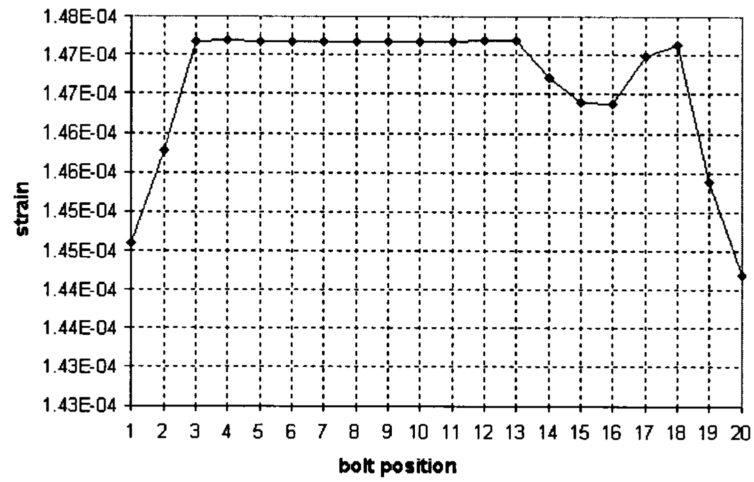

Figure 3.26 Average strains in θ direction of the middle surfaces of right liner bolt holes

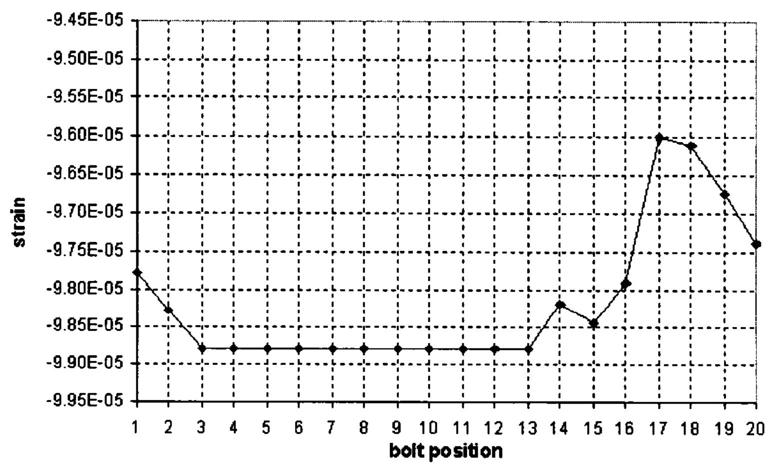

Figure 3.27 Average strains in r direction of the bottom surfaces of right liner bolt holes

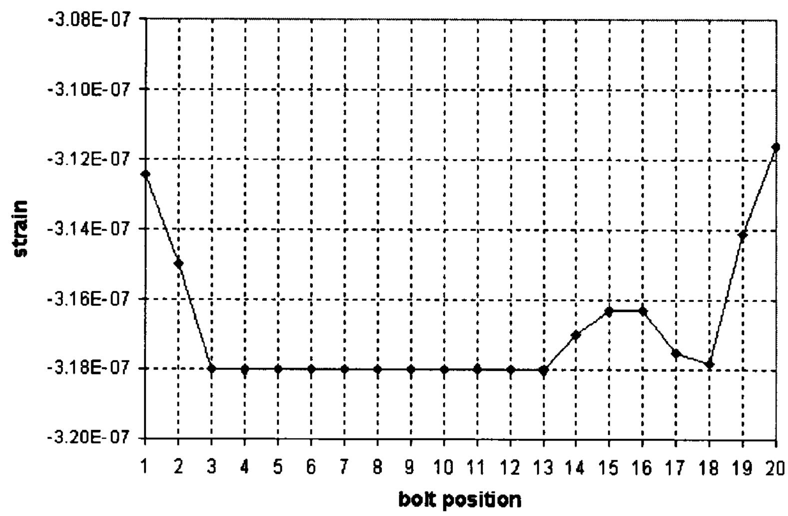

Figure 3.28 Average strains in r direction of the bottom surfaces of right liner bolt holes

From the results of right liner bolt holes shown above, we can draw the following conclusions:

(1) Between bolt positions 3 to bolt position 13, the values of strains are almost the same or just show a little difference. From the bolt position definition in Figure 3.10, we know that the zone of the mill located between bolt position 3 and 13 is free of ore's action.

(2) The maximum strains (absolute value) occur at around bolt position 18 or 20. This position is around where the mill affords the maximum force coming from ore. Because of the structurally asymmetric property of the lifter, along with the force acting form, the force acting on the lifter's face side (the same side as right liner bolt side) makes the lifters show a turning tendency toward the other side. As a result, the strain of the bolt hole is the combined results from the pressing and turning effect.

(3) Since the right liner bolts are double in number compared to that of the left side, at bolt position 5, there is no obvious strain value change.

3.7 Conclusions

This chapter gives the detailed strain analysis of the mill bolts and bolt holes. From the comparison of the figures showing the strain changing at different bolt positions, we can summarize that the strain of the bolts, no matter whether it is at the lifters, left liners or right liners, all has comparatively obvious rules depending on different bolt positions.

(1) Above figures clearly show that all the strain curves in r and θ direction have extreme values at the position around bolt position 18. Bolt Position 18 is almost in the middle between toe position and shoulder position (refer to Figure 3.9).

(2) At toe angle, which is about bolt position 3, and at shoulder angle, which is about bolt position 14-15, the strain curves of bolts in liners (both left and right) undergo great changes.

(3) At toe and shoulder position, the strain curves of bolts in the lifters do show some changes, but the changes are not as conspicuous as the curves of bolts in liners.

(4) The variations between strains at different bolt positions are exist but are very small.

For bolt top surface, the variation of no-ore-acting zone is less than 0.3%
For bolt top surface, the variation of ore-acting zone is less than 1.5%
For bolt middle surface, the variation of no-ore-acting zone is less than 0.4%
For bolt middle surface, the variation of ore-acting zone is less than 2%
For bolt bottom surface, the variation of no-ore-acting zone is less than 0.8%
For bolt bottom surface, the variation of ore-acting zone is less than 3.8%

(5) Bolt stress/strain can possibly be used but the variation is very small. When the vibration noise exists, the measurement will be a problem. Deducing torque preload in instrumented bolts may be a method worthy of consideration and will be further investigated in the future.

CHAPTER 4

LIFTER/LINER STRESS ANALYSIS

Mill lifters/liners are very important components of tumbling mills. Their geometry profile and mechanics properties greatly influence the mill operating behavior. Wear is the main failure form of lifters/liners. Changing lifters/liners which reach the wearing limit is really time consuming and money consuming. Liter/liner sensors are widely developed and used since they can provide real time monitor of the mill operating state.

This chapter sets out to determine the effect of the liner wear sensor, which is developed by Martin, Li and Radziszewski [33], on the liner structural strength. In this chapter, the influence of the number, position, height of sensor, and liner thickness on the mill strength are also investigated.

4.1 Introduction

Lifter/liner sensors are now widely adopted as an effective way of controlling mill operation. Lifter/liner sensors with different structures, different shapes and different functions are used. Since the sensors need to be installed inside the lifter/liner, the strength property of the lifter/liner will be changed. Many researches have been devoted to the sensor design and few attentions were paid to the lifter/liner strength variation. Based on the liner wear sensor developed by Martin, Li and Radziszewski [33], this chapter performs detailed FEA analysis on the lifer/liner strength behavior with lifter/liner sensor installed inside. The analysis will provide strong foundation for the practical utilization of this kind of liner wear senor.

Besides, the liner thickness is a very important mill design parameter. A lot of mill liners are made of steel. Thinner mill liner design will save a lot of material and will make liner changing much easier.

4.2 Background

Direct monitoring of the comminution process is not feasible due to the hostile environment inside the mill. However, information such as mill load, charge position or slurry properties is directly related to the mill operating state and can be used to control and optimize the mill operations. In this case, sensors are of great value since they are capable of delivering such information. The difficulty of investigating charge motion inside the mill by using sensors is that the complex motion of a grinding charge is determined by both mill design variables such as liners, lifter profile, discharge mechanism, and process operating variables such as solid content, size distribution and slurry viscosity. In recent years, a lot of research work has been done using different kinds of sensors to investigate the behavior of the mill.

The wear of tumbling mill liners influences the load behavior and consequently the performance and efficiency of tumbling mills. Since liners wear and change profiles, mill performance will correspondingly vary over the useful liner life. The ability to simulate

Kalala, Bwalya, Moys [36] use a two-dimensional mill with one instrumented lifter bar to obtain the normal and tangential forces exerted on it. They compared their measured results to the DEM simulated results. Their experimental two-dimensional mill had an internal diameter of 0.55 m for a length of 0.023 m. The length of the mill was chosen to allow the motion of balls of 0.0222 m in diameter to move only in two dimensions. The mill was equipped with 12 equally spaced square lifters of 0.022 * 0.022 m. One of the lifters (Figure 4.3) was instrumented using strain gauges in order to record the normal and tangential forces exerted on it.

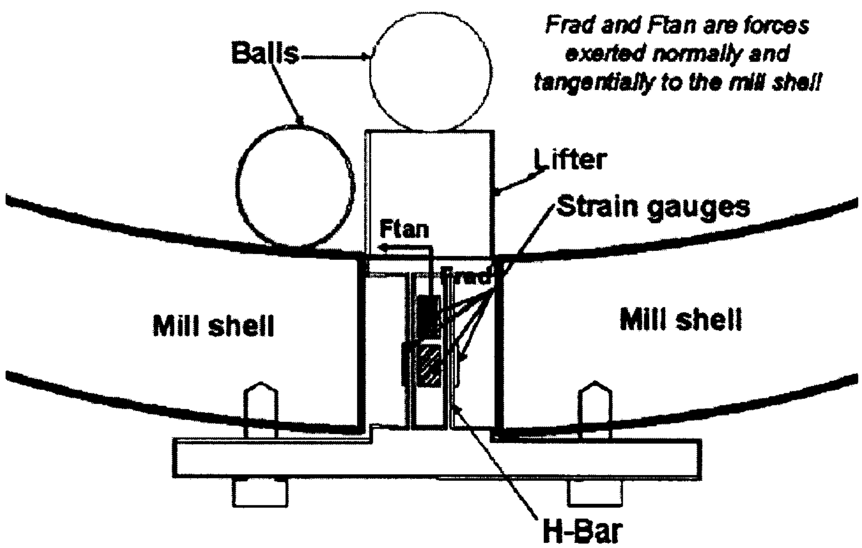

Figure 4.3 Instrumented lifter bar [36]

Besides, surface vibration of the external shell has also been traced by sensors to monitor the mill process and performance variables. The collision events associated with the mill charge motion during the comminution processes strongly contribute to acoustic emissions. Accelerometers are often used to detect the component of surface displacement normal to the mill shell, predominantly due to the propagation of surface vibration waves. The key problem with this method is the localization and characterization of sources that emit the detected vibrations in circumstances of low wave attenuation characteristics [4].

Liner wear will result in a gradual decrease in liner height. Wear occurs as a result of the application of shear and normal stresses to the liners by the contacting particles as liners travel through the charge. Additional stresses will occur where, due to a high rotational velocity, falling rock fragments or steel balls impact the lifters and mill liner.

4.3 Liner Wear Sensor Development

Although many kinds of liner sensors are developed, each kind of sensor has its disadvantage in installation, tolerance and efficiency limitation. Being a real-time, on-line measurement system that is used to investigate the wear inside the mill, the liner sensor should be simple for installation, and bring minimal change to the liner structure and have the property of fault tolerance. Martin, Li and Radziszewski [33] developed a kind of instrumented liner for tumbling mill wear monitor. The basic purpose of this method is to indicate the position at which the liner will wear as well as the time at which this will occur by installing sensor/sensors inside the lifter/liner. The instrumented liner is a collection of sensing wires that are permanently fixed to the lifter. Figure 4.4 illustrates the possible sensor positions and Figure 4.5 shows the basic DAQ (Data Acquisition) board prototype. This kind of small and low-cost real-time, on-line measuring wear sensor has been proved to be effective in the dry lab tests and wet tests. Test results show that multiple sensors and multiple boards can increase the test reliability. If a liner wear model is to be used in conjunction with the instrumented lifter, a larger number of sensors are necessary.

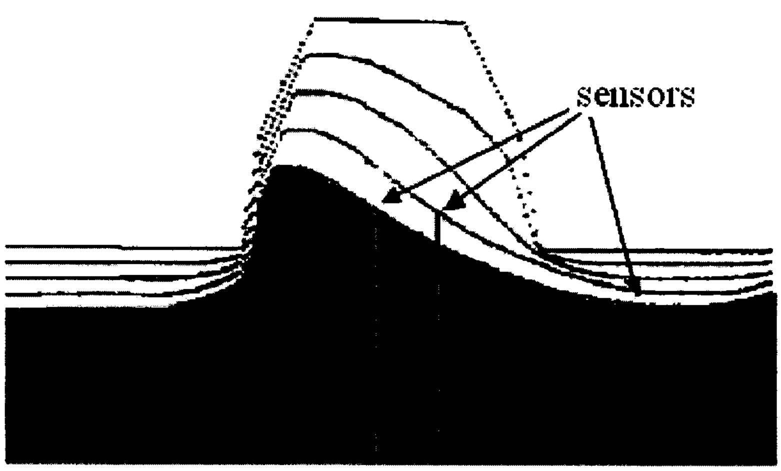

Figure 4.4 Possible sensor positioning [33]

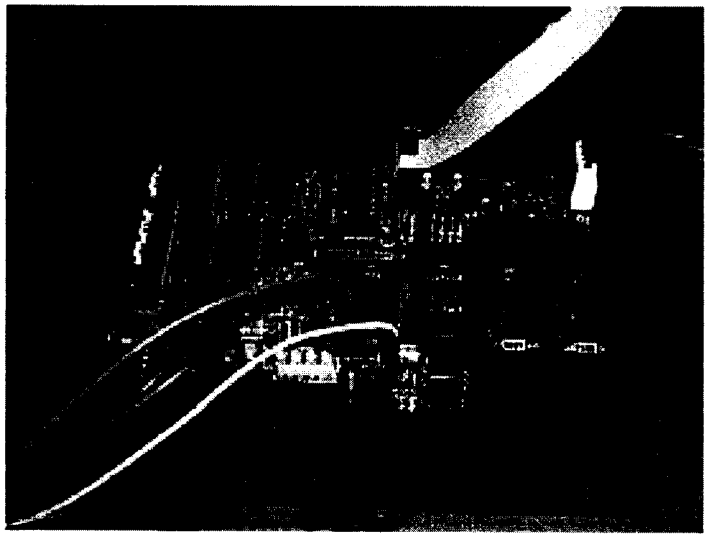

Figure 4.5 Wear sensor's prototype [37]

One of the necessary and important steps of this kind of wear sensor installation is that some holes must be machined in order to install the wire sensors. In the prototype lab test, six blind holes were machined in a block of mild steel and two sensor wires were inserted in three of the six holes at variable depths. The Permatec Cerbide epoxy was used to fix the wires in place [33]. Then the problem of whether such kind of installed wires inside the lifter will influence the strength of the lifter will rise. And the influence of their positioning on the lifter strength is also worthy of consideration.

4.4 Liner Stress Analysis

In this chapter, two kinds of FEA analysis are involved. One is dynamic analysis and the other is structural static analysis. The dynamic FEA analysis is performed with the aid of ANSYS/LS-DYNA for calculating the charge impact force and the structural static FEA analysis is executed for liner (liner wear sensor installed) stress analysis by ANSYS, where contact analysis is also included.

4.4.1 Impact Force Estimation

In the mill working process, the charge will rotate along with the mill because of the lifting action of liners and the friction between the mill liner and the charge. When the charge is raised to a certain altitude, it will fall down and impact on the mill liner or on the other charges because of its gravity. In order to decide the value of the impact force, an impact FEA analysis with ANSYS/LS-DYNA is carried out. In the current work, a mill with a diameter of 8530mm and a length of 4920mm is used. The outline of the mill is shown in Figure 4.6. Figure 4.7 shows a part of the detailed FE model. The grids of the piece of liner that the charge will fall on are much finer than the others. In the calculations, the charge is simulated as a ball with a diameter of 100mm.

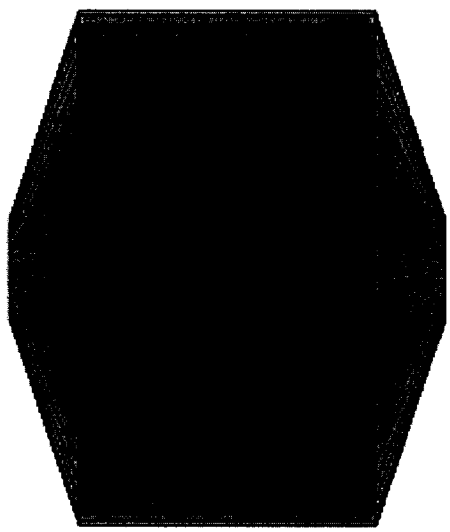

Figure 4.6 Mill Profile

The charge impact calculation is a dynamic contact analysis. The impact force can be obtained through the contact force between the charge and the liner. In the calculations, the impact actions coming from one ball, two balls, three balls and other multiple balls (same size, different axial direction position) are calculated. The average impact force of all these calculations is used as the charge impact force. At the same time, we can also get the node time history stress/displacement curves. Figure 4.8 and Figure 4.9 demonstrate respectively the time history mises stress and displacement in y direction (coordinate system refers to Figure 4.7) of the node in the middle of the impact area. The unit of the stress (Figure 4.8) is 10^{-3} MPa and the unit of the displacement (Figure 4.9) is 10^{-4} m.

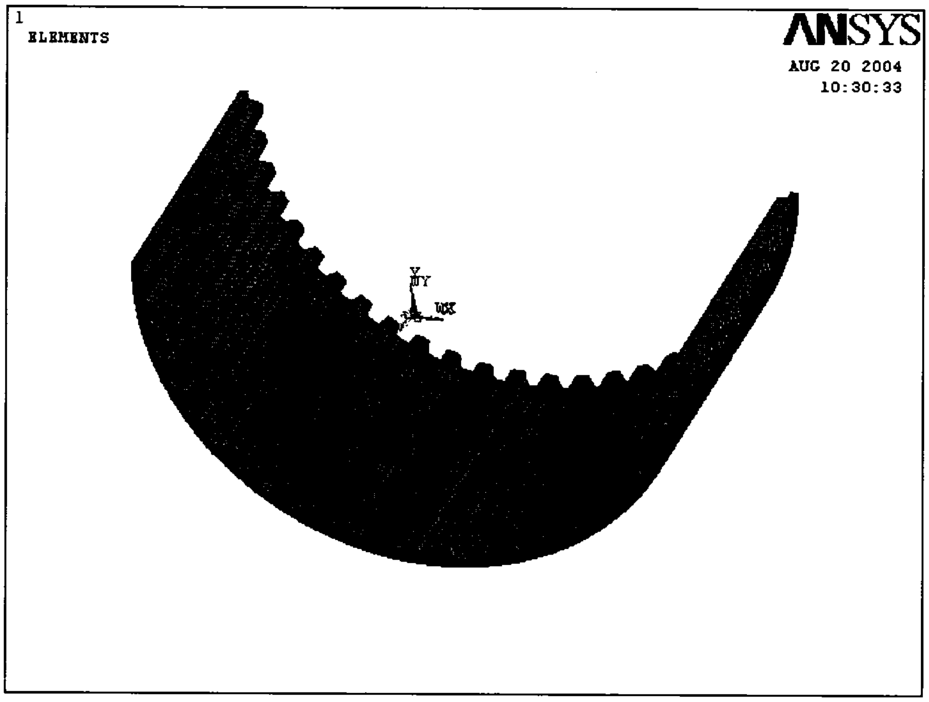

Figure 4.7 Part of the FE model of the mill

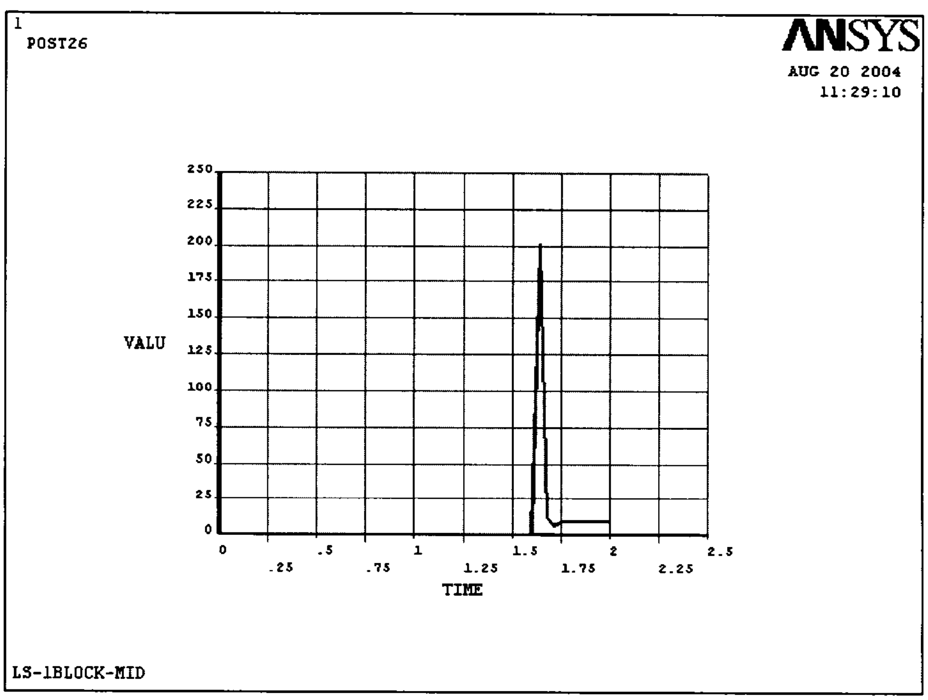

Figure 4.8 Time history node mises stress

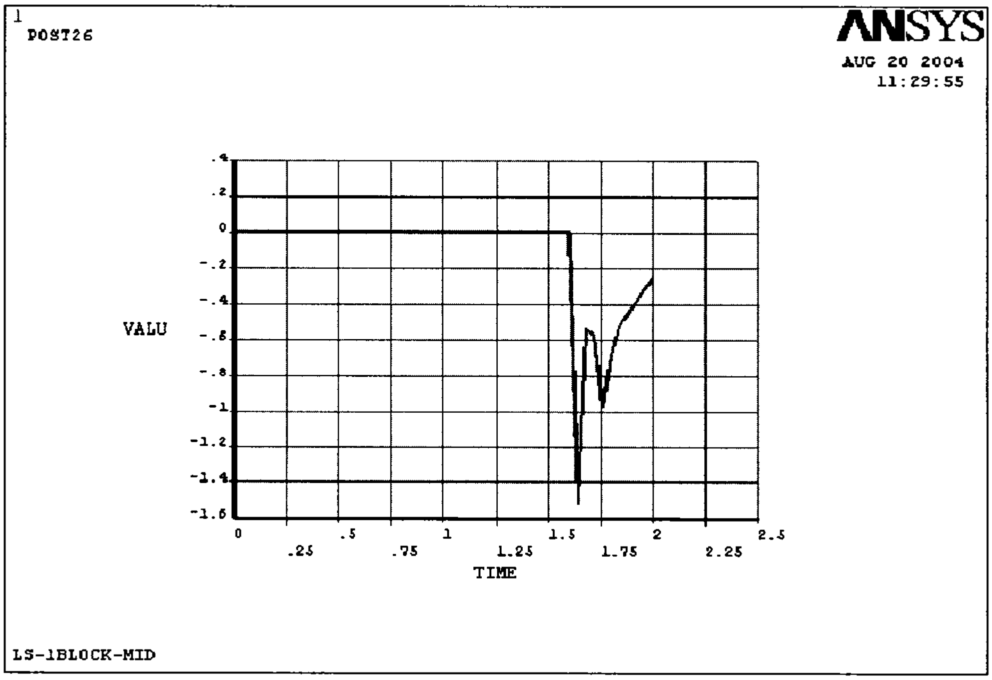

Figure 4.9 Time history node displacement

4.4.2 3D Mill Model

Since the part of liner sensor inserted into the lifter is actually composed of wires, which has a diameter of nearly 1-2mm, it is too complex to establish the 3D FE model for the whole mill. To simplify, we will only set up the FE model for one piece of liner (through the whole mill chamber length). Accordingly, the calculation time will be greatly decreased. Then the question of which piece of liner of the analyzed mill type will be chosen to generate FE model must be solved first. In this chapter, the stress and strain of all single pieces of liners (with sensor) located in the ore-acting zone (lying between the toe angle and the shoulder angle) of the charge profile in stable working conditions are compared. All these liner models have the same FE grids and have the same kind of sensor. The only difference is that they occupy different mill circumferential positions. And the piece of liner which has the maximum stress will be selected as the final calculation position.

In the current calculations, the charge volume is 40% of the mill volume and the mill rotation speed is 75% of the mill critical speed. The charge profile is showed in Figure 4.11, which refers to the charge profile coming from Granulair Technologies [38] (see Figure 4.12). Altogether, 21 pieces of liners are compared and they are numbered as shown in Figure 4.11. For the boundary conditions of the FE models, we'll define them in cylindrical system since the model is in cylindrical shape. The cylindrical system is defined in Figure 4.10. The translations in Z and R directions of the two mill shell ends, which related to the feed end and the discharge end of the mill, are constrained. The θ directions for the left and right side of the single piece of liner are also constrained. Figure 4.13 is the liner FE model.

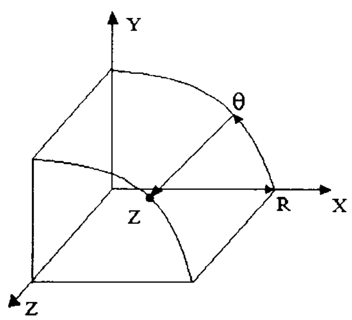

Figure 4.10 Cylindrical system (R,θ, Z) [23]

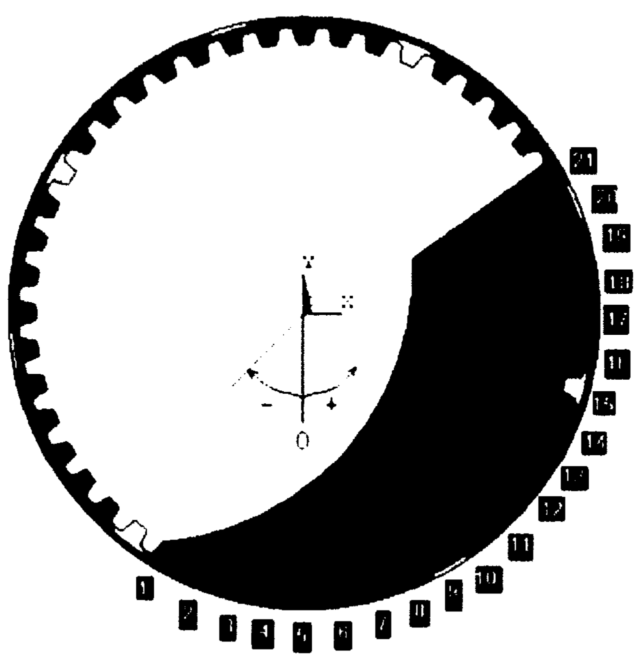

NO.	Angle (Degree)	NO.	Angle (Degree)
1	-30	12	52.5
2	-22.5	13	60
3	-15	14	67.5
4	-7.5	15	75
5	0	16	82.5
6	7.5	17	90
7	15	18	97.5
8	22.5	19	105
9	30	20	112.5
10	37.5	21	120
11	45		

Figure 4.11 Charge profile with 40% charge volume and 75% mill critical speed

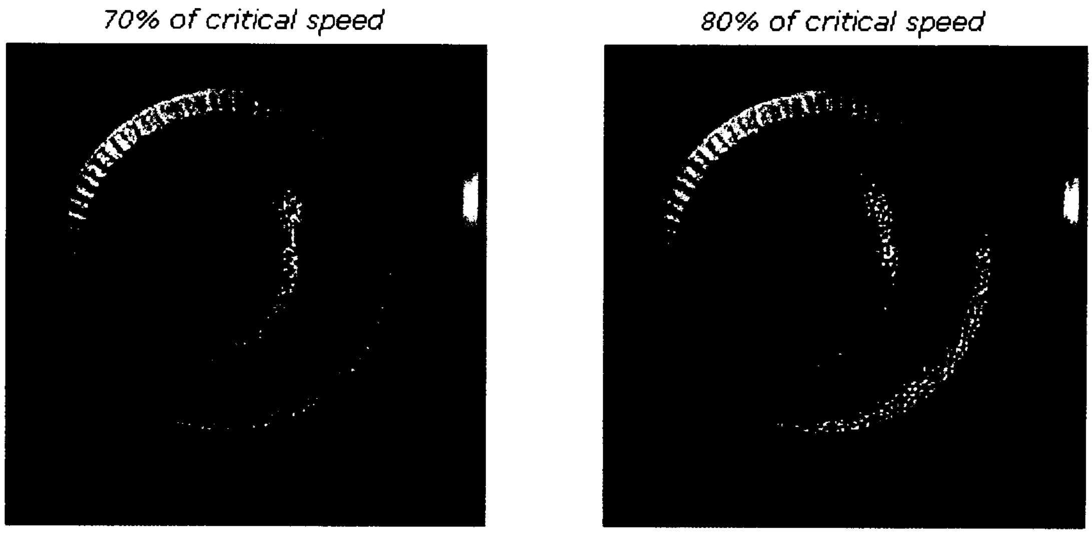

Figure 4.12 Charge Profile [39]

All these 21 liner models are calculated and the maximum and minimum mises stresses of each liner are listed in Table 4.1. The angles in the table are defined according to the cylindrical system (Figure 4.10), its positive/negative direction is also defined in Figure 4.11.

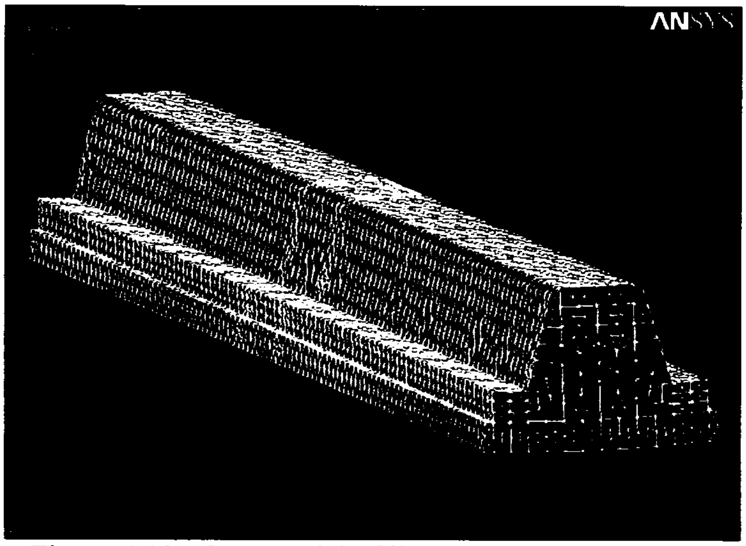

Figure 4.13 FEA model of liner wear sensor analysis

The displacement distributions of the liners at different positions can also be obtained by FEA analysis. Figure 4.14 to Figure 4.19 show the displacement distributions of liners at different positions in theta direction under cylindrical system.

No.	Angle (degree)	Min Mises Stress (N/m^2)	Max Mises Stress(N/m^2)
1	-30	6393	1.44e6
2	-22.5	21177	5.95e6
3	-15	72410	1.03e7
4	-7.5	100458	1.45e7
5	0	126074	1.85e7
6	7.5	152477	2.29e7
7	15	177522	2.74e7
8	22.5	229305	3.6e7
9	30	327015	3.87e7
10	37.5	340198	3.46e7
11	45	301936	3.19e7
12	52.5	223928	2.79e7
13	60	239979	2.4e7
14	67.5	170630	1.84e7
15	75	63076	1.25e7
16	82.5	73393	1.22e7
17	90	79777	1.17e7
18	97.5	71240	1.15e7
19	105	65054	1.17e7
20	112.5	64963	1.13e7
21	120	19.877	6.68e6

Table 4.1 Maximum and Minimum Mises stress of lifter/liner at each position

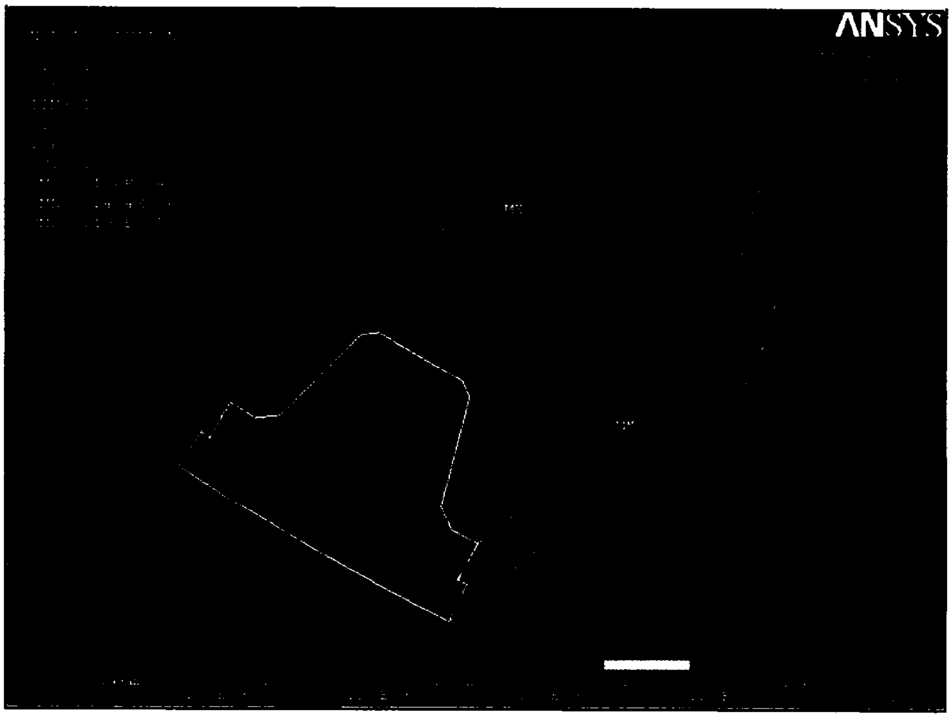

Figure 4.14 Displacement in theta direction at position 1 (-30°)

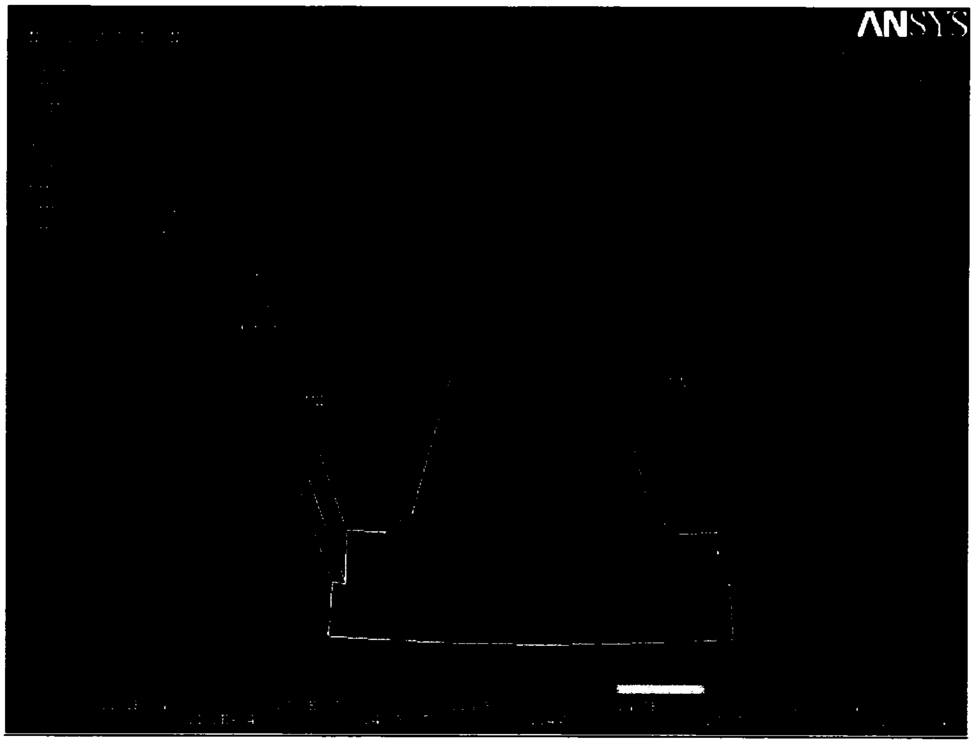

Figure 4.15 Displacement in theta direction at position 5 (0 °)

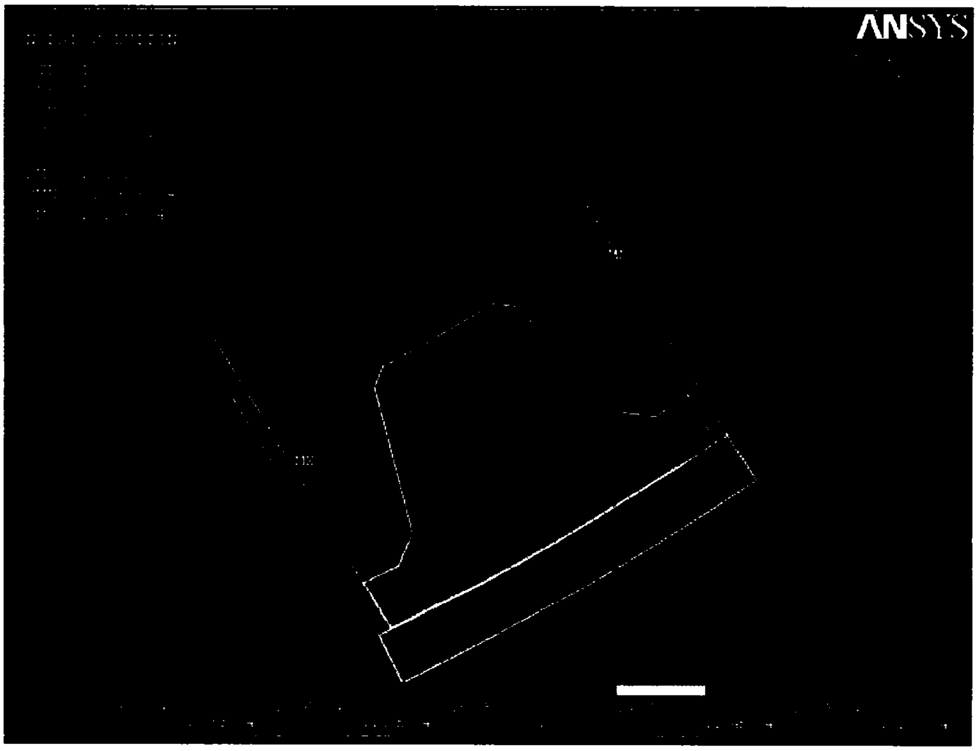

Figure 4.16 Displacement in theta direction at position 9 (30 °)

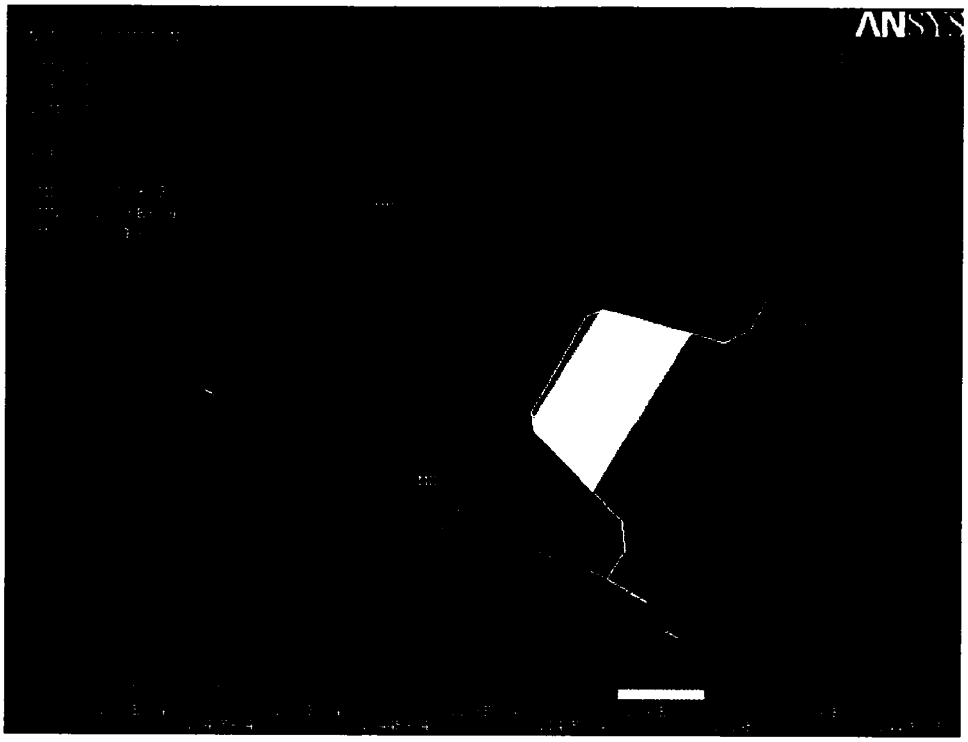

Figure 4.17 Displacement in theta direction at position 13 (60°)

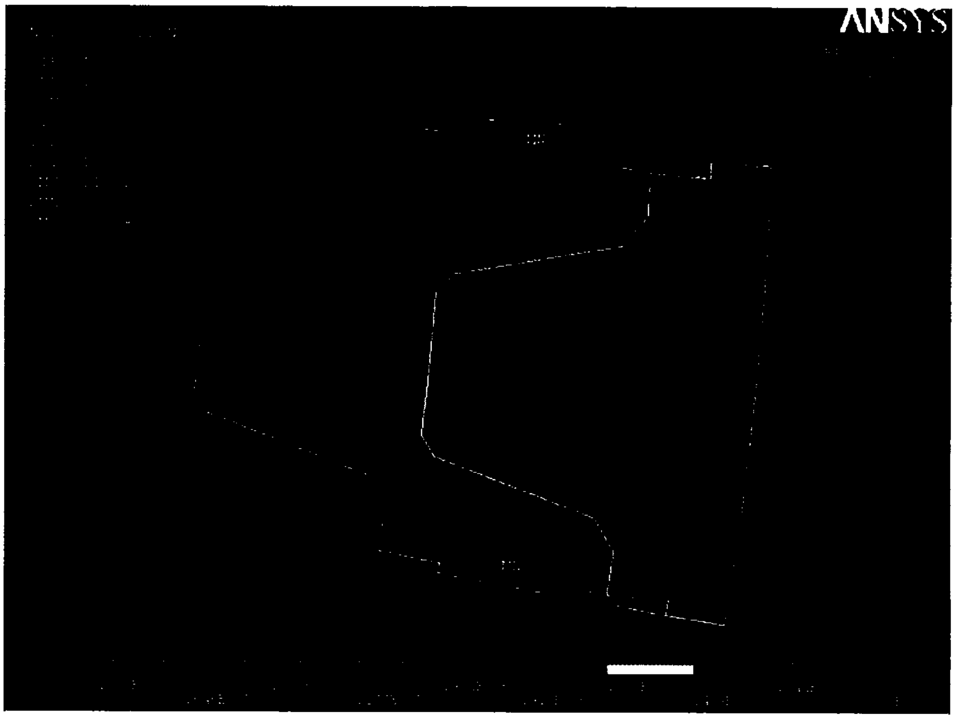

Figure 4.18 Displacement in theta direction at position 17 (90°)

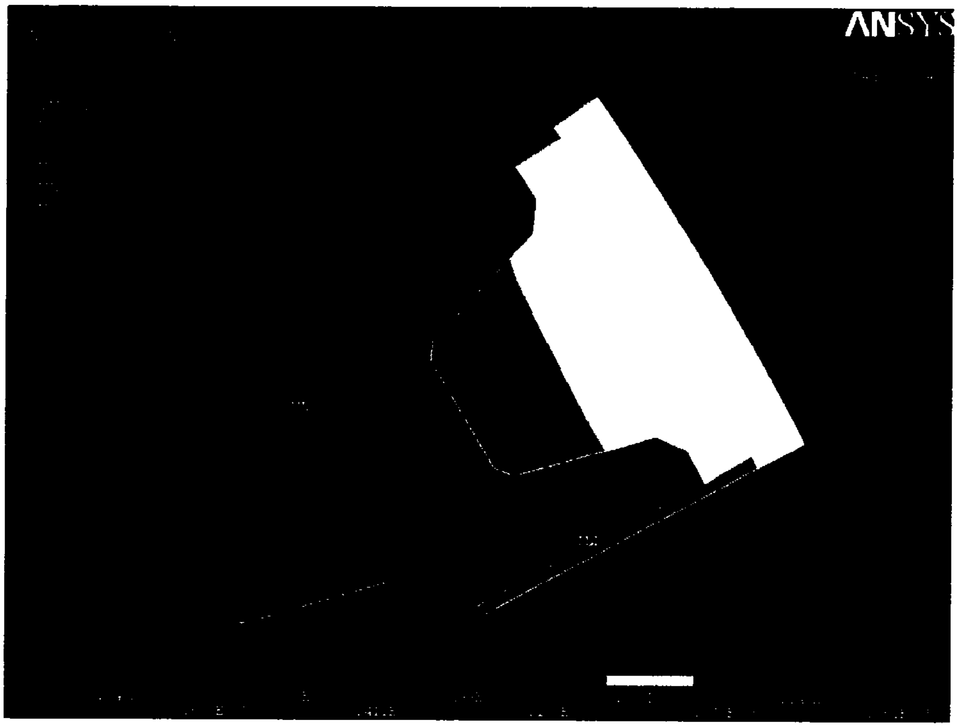

Figure 4.19 Displacement in theta direction at position 21 (120°)

4.4.3 Effect of the Wear Sensor on Liner Stresses

Along the profile of the lifter, different positions have different degrees of wear. Single and multiple sensors will be used to measure the liner wear. Accordingly, different FE models are established to investigate the stress and strain distributions inside the liner. In the present work, five kinds of sensor positions are considered, as shown in Figure 4.20. For single sensor, we calculate the cases when the single sensor is posed in the five positions separately. For multiple sensors, we calculate the case when positions 1, 2, 3, 4, 5 all have sensors seated. As to the height of the sensor, two kinds of sensor heights, which are shown as Figure 4.20 and Figure 4.21, are considered. Concretely, the H2 at position p1, p2, and p3 is almost 85% of the H1 at corresponding positions; the H2 at position p4 and p5 is almost 80% of the H1 at corresponding positions. H1 at position p1 is 0.4052m and H1 at position p4 and p5 is 0.3496m.

Similar FE models as shown in Figure 4.13 are established for FEA simulations. In the models, mill shell, lifter, and liner sensor are of different material properties separately.

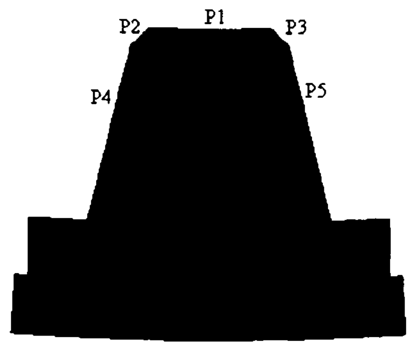

Figure 4.20 Sensor position of P1, P2, P3, P4, and P5 with height H1

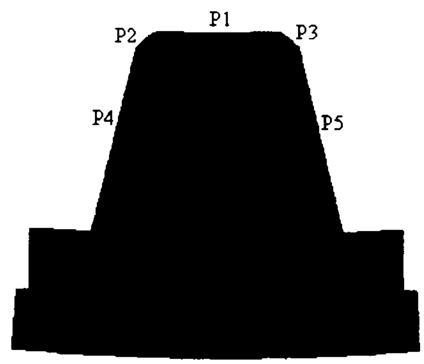

Figure 4.21 Sensor positions of P1, P2, P3, P4 and P5 with height H2

Table 4.2 lists the maximum mises stresses of the liners when the single sensor is at different positions with different heights. From the values, we can see that different cases have different stress values. But the differences between the values are very small; the variation is less than 4%. It clearly demonstrates that the single liner sensor will not obviously change mill strength.

Sensor Position	Sensor Height	Maximum Mises Stress (N/m^2)
P1	H1	3.87e7
	H2	3.74e7
P3	H1	3.86e7
	H2	3.85e7
P5	H1	3.88e7
	H2	3.84e7

Table 4.2 Maximum mill stress with single sensor at different positions

Table 4.3 shows the liner maximum stresses when multiple sensors are installed in the liner with different heights. Similar to the single sensor cases, the difference of the values is still very small.

Sensor Position	Sensor Height	Maximum Mises Stress (N/m^2)
P1, P2, P3, P4, P5	H1	3.83e7
P1, P2, P3, P4, P5	H2	3.82e7

Table 4.3 Maximum stress with multiple sensors with different height

4.4.4 Effect of Linear Thickness on Linear Stresses

Liner thickness is very important since it has direct relationship with the mill manufacturing cost and convenience of changing liners. So, the influence of liner thickness on the mill strength needs to be further considered. In the present work, three kinds of liner thicknesses are considered and the stress distributions of these three different models are compared. The three kinds of liner thickness are shown in Figure 4.22. Concretely, L1 is the original liner thickness; L2 is 2/3 of the original thickness; L3 is 1/3 of the original thickness. The original liner thickness is 0.0762m.

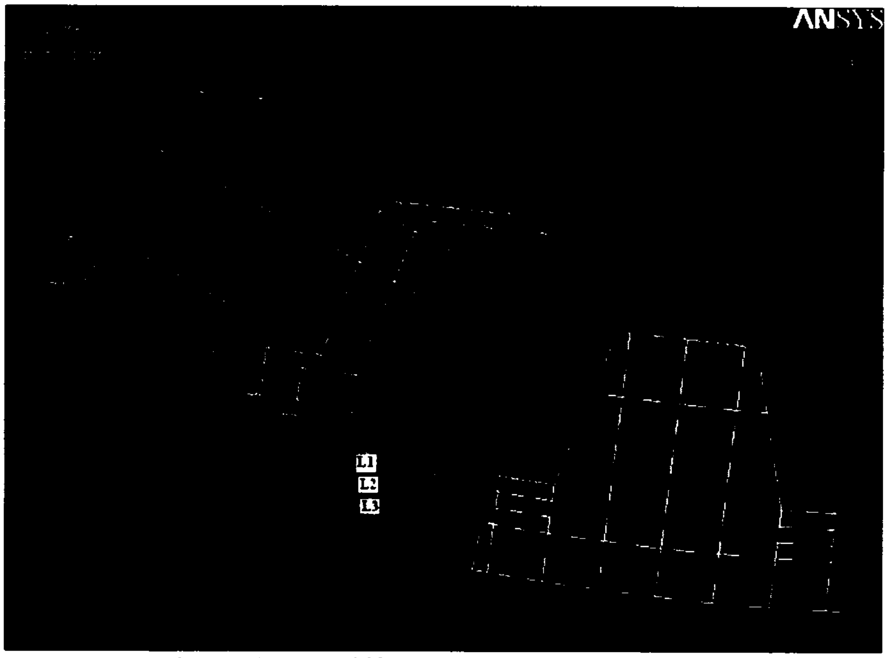

Figure 4.22 Different liner thickness profile

By FEA analysis, we can also get the stress distributions of the liners with different liner thicknesses, different sensor positions, and different sensor heights. The maximum mises stresses of the liner are shown in Table 4.4.

Liner Thickness	Sensor Position	Sensor Height	Maximum Mises Stress (N/m^2)
L1	P1	H1	3.87e7
		H2	3.72e7
	P3	H1	3.86e7
		H2	3.85e7
	P5	H1	3.88e7
		H2	3.84e7
L2	P1	H1	3.89e7
		H2	3.81e7
	P3	H1	3.88e7
		H2	3.86e7
	P5	H1	3.91e7
		H2	3.9e7
L3	P1	H1	4.34e7
		H2	4.31e7
	P3	H1	4.33e7
		H2	4.32e7
	P5	H1	4.36e7
		H2	4.35e7

Table 4.4 Maximum stress of single sensor at different positions

Table 4.4 clearly shows that the liner thickness does have influence on the mill strength. The thinner the liner is, the higher the maximum stress is. And the stress increase from L2 to L3 is quite bigger than that from L1 to L2. Figure 4.23 clearly demonstrates this behavior. In Figure 4.23, horizontal axis represents the liner thickness and the vertical axis represents the ratio of maximum mises stress of liner thickness L1, L2, L3 to the maximum stress of liner thickness L1.

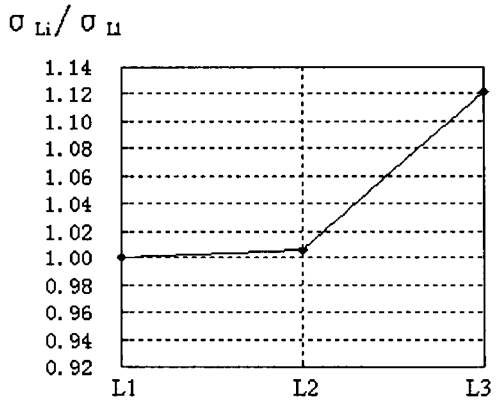

Figure 4.23 Maximum stress changing related liner thicknesses

4.5 Conclusions

From the above analysis, we can reach the following conclusions:

(1) The material of the mill used in the simulations is cast iron. The yield stress of cast iron is in the range: 1.2-2.9e8 N/m2 [40], and the calculated maximum stress is between 3.72e7-4.36e7 N/m2. So, we can come to the conclusion that this kind of liner sensor is accessible from the point of material strength.

(2) The installation of sensor/sensors will not cause specious stress focus. And this kind of liner sensor will not change the liner's mechanical property. That is, this kind of real-time liner wear measure method is accessible.

(3) The thickness of the liner does influence a lot the stress distribution of the mill, and the thinner the liner is, the higher the stress is. When liner thickness is changed from L2 to L3, the maximum stress increases greatly.

CHAPTER 5

EXPLORING TUMBLING MILL RESONANCE

Resonance is so important that it becomes an unavoidable issue that engineers must face. Accurate prediction of resonant behavior of rotating machinery is of great importance to designers and many attempts have been made to calculate exactly. Being rotating machinery, tumbling mills have quite different resonant behavior from the stationary machinery. The main reason for this difference is known to be the gyroscopic momentum. Their natural frequencies vary along with the rotation speed of the mill. When mill resonance happens, the mill shakes greatly and it cannot work properly. The common ways in which milling industry used to deal with this situation bring about extra mill downtime and cost.

In this chapter, the resonance of tumbling mills as a function of mill aspect ratio and mill operating speed is thoroughly explored by using six different kinds of mill FE models. FEA modal analyses are performed to investigate their mode shapes and natural frequencies at different mill rotation speeds. Besides, the influence of rotation speeds on the natural frequencies; the influence of the mill parameters on the mill natural frequencies are also discussed.

5.1 Introduction

Different from the stationary machinery, the resonant behavior of tumbling mills is related to mill rotation speed. In the case of resonance, the mill shakes greatly and cannot work properly. Usually, the ways to overcome this state is either to change the volume of the ore in the mill or to change the mill speed. Although mill resonance in most cases does not occur, when it does, it causes operating problems. Moreover, modern comminution requires large and reliable electrical systems for operation in mining environments. The resonance and transient behavior caused by those low-damped electrical systems increases the probability of over-voltages caused by resonance. Therefore, comprehensive investigation of mill resonance becomes even more important. It will help us decide which component and which parameters are the key reasons for resonance so as to provide guidance for mill system design.

In this chapter, six different tumbling mill FE models are generated and detailed FEA modal analyses are carried out in order to investigate the mill resonant behavior. As we all know, mill system is a very complex system, which includes many mechanical and electrical components. In order to get the accurate vibration behavior of the mill system, we should include all the components in the model and the connection between the components. But being the first step of the detailed modal analysis of the tumbling mill system, the present work only considers the mill itself to simplify the simulation. More parts will be considered and the model will be further developed in the future.

5.2 Background

Resonance is something engineers always have to bear in mind. In 1940, the Tacoma Narrows Bridge, now better known as "Galloping Gurdy", collapsed because a steady wind made the bridge oscillate at its resonance frequency. The amplitude of the oscillation increased continuously and caused the bridge to twist and eventually resulted in its collapse. Now we all know that the reason of the collapse of bridge is that the frequency of the wind happened to be consistent with the resonant frequency of the bridge. Although resonance is very useful for musical instruments, it is always very harmful for engineering and tried to be avoided by engineers by adjusting their designs. The vibrations of mechanical systems are caused by sudden or continuous disturbances. The energy contained in the disturbances is transmitted to the mechanical systems and finds its way to propagate throughout the system. Therefore, the assessments of whether any component of the mechanical system will break during the initial violent disturbance stages, subsequent steady-state vibrations, degradations of system performance during the post-disturbance period, and potential fatigue failure due to prolonged vibrations are very important for designers.

Mill equipment can be quite large; it includes motor, bearings, gearbox, chain drive, axle, charge and so on [41]. All these parts are connected to each other and affect each other. Its resonant property is related to different parts that compose the whole system and the linkage between them. Furthermore, the foundation also plays a very important role. For example, Penta Engineering Corporation evaluated and provided solutions for a vertical mill foundation with excessive vibrations [42]. They studied the dynamic behavior of the mill foundation and the interaction with the soil. Their analysis also included Foundation Finite Element Models and a study of frequencies and resonance. They performed a dynamic analysis that included a 3D model of the mill foundation and the surrounding soils. Meanwhile, the transmitted loads from the mill to the foundation are considered in the model. By evaluating the main frequencies of the foundation system, they determined that the resonant problems in the plant were due to the poor isolation capabilities of the mill foundation.

A very important feature of the frequency behavior of rotating machinery is the frequency dependency of the rotation speed. Figure 5.1 shows the resonant behavior related to mill rotation speed. To a stationary observer, there are two kinds of traveling waves: forward traveling wave and backward traveling wave. Frequencies associated with the natural frequencies of the structure are typically measured by using sensors. These frequencies often vary with speed of rotation due to gyroscopic and centrifugal effects. Take shafts for example. Whirling motion of shafts causes the centre of gravity of a shaft cross-section to move in an elliptical orbit around the centre of rotation. The gyroscopic forces have a stiffening effect on forward whirl of shafts and a softening effect on backward whirling rotors. Usually, the vibration behavior of rotating machinery is recorded and plotted on a time-frequency distribution diagram [38] or a Campbell diagram [40] or, more recently, using wavelet maps [43]. Both time-frequency and Campbell diagrams provide important information about the evolution of the frequency spectrum of the response with time or with speed of rotation. This information assists us considerably in detecting changes in structural resonance frequencies, and is useful for detecting structural changes or possible damages.

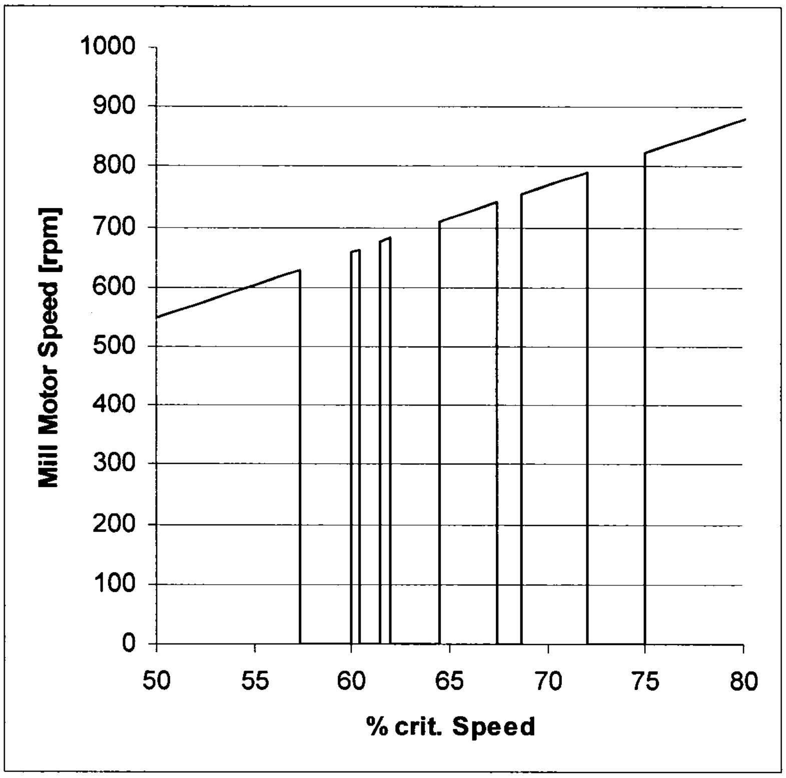

Figure 5.1 Mill resonance behavior related with mill rotation speed [2]

With regard to rotating systems, the equations of motion may involve significant gyroscopic, Coriolis, and centripetal accelerations [44]. Also, the stiffness characteristics of the structure may be modified by the steady state internal loads induced by the centrifugal forces. The main parameters that affect the nature of the response include speed of rotation, external loading, and asymmetric in both rotating and non-rotating parts of the structures. The unbalance response resulting from the combined effect of very small imperfections and structural asymmetries manifests itself in both the amplitude and frequency of the response. The gyroscopic forces have a stiffening effect on forward (co-rotating) whirl of shafts and a softening effect on backward (counter-rotating) whirling rotors.

External loads can also change the natural frequencies of rotating machinery. Behead and Bastami investigated the effect of centrifugal force on natural frequencies of lateral vibration of rotating shafts, and he obtained the curves shown in Figure 5.2 and Figure 5.3 [45].

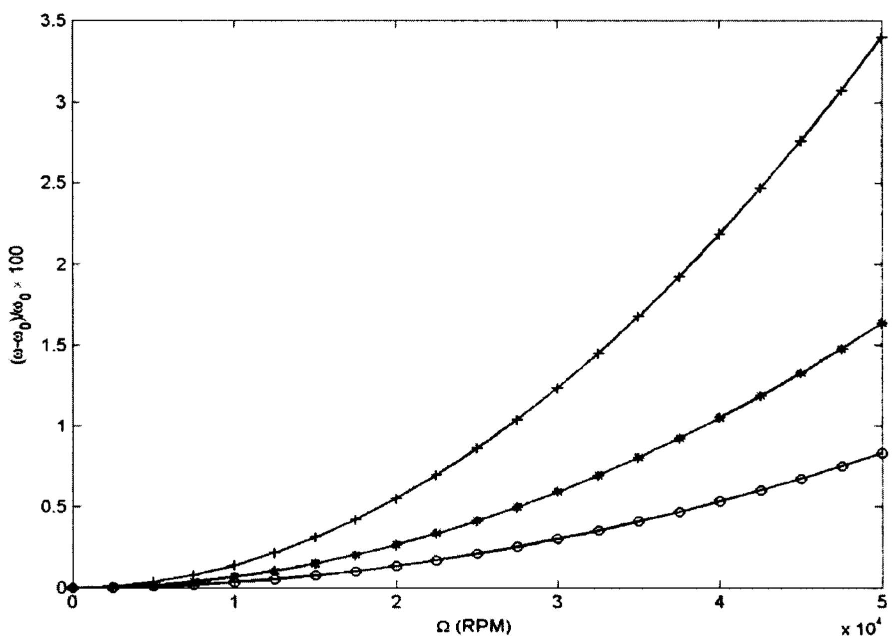

Figure 5.2 Relative change of natural frequency versus shaft speed with different boundary conditions with 1m length

. —+—, pin-pin; —*—, pin-clamp; —O—, clamp-clamp [45]

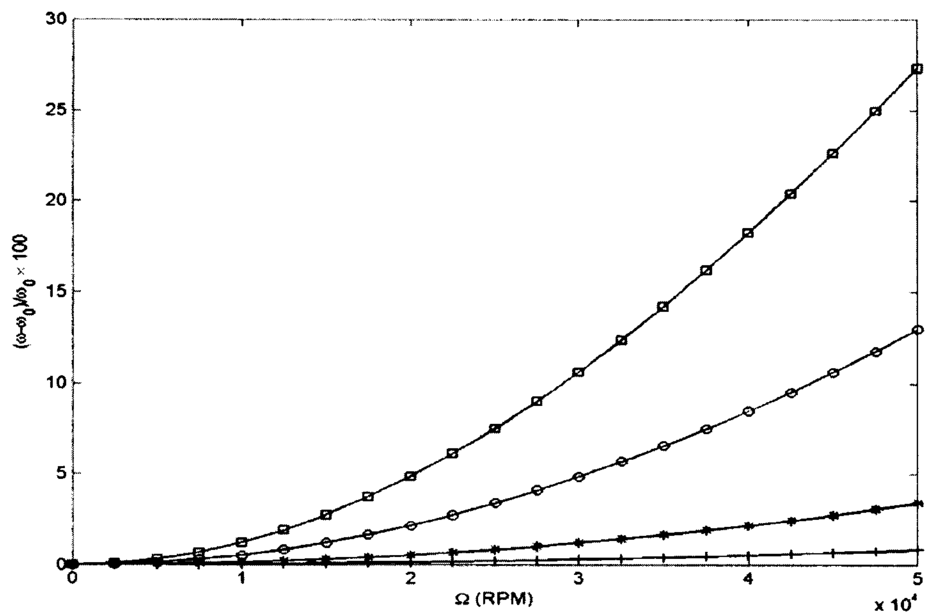

Figure 5.3 Relative change of natural frequency versus shaft speed for a pin-pin steel shaft: –+–, L=0.5m; –*–, L=1m; –O–, L=2m; – –, L=3m [45]

Although damping has a great effect on the amplitude and energy dissipation of a vibrating system, for most mechanical structures, the damping ratio is small. Even for the extreme case that damping ratio is as high as 0.2, the difference between undamped natural frequency (ω_n) and damped natural frequency (ω_d) is still only 2% [46]. It means that, for a modal analysis, the increased complexity of the computation involving damping has virtually very little effect on its numerical results for natural frequencies. Hence, damping is generally not taken into account in the following modal analyses.

Tumbling mills have some similarity to circular cylinders by having cylindrical chambers. Since the first cylindrical shell problem was investigated by Aron in 1974, many efforts have been devoted to investigate how the Coriolis accelerations and large deformations affect the vibration modes of high speed rotating hollow cylindrical. Chen et al. used a nine nodes curvilinear super-parametric finite element method to solve the problems of vibrations of high-speed rotating shells of revolution [47]. They also gave the formulas of calculating the resonance frequencies of cylindrical shells. The two low resonance frequencies are shown in (5-1):

$$\omega_n = \frac{2n}{n^2+1}\Omega \pm \sqrt{\frac{n^2(n^2-1)^2}{n^2+1}\frac{Ek}{\rho(1-\mu^2)} + \frac{n^4+3}{(n^2+1)^2}\Omega^2} \qquad (5\text{-}1)$$

In this equation, the first term shows the effect of the rotation speed on the frequencies. The second is due to the normal bending stiffness, and the third caused by the Coriolis force and large deformation [47].

It should be noted that this relationship is applicable to thin shelled cylinders that are defined as (5-2) [49]:

$$t / r <= 1/20 \ (5\ \%) \qquad (5\text{-}2)$$

where t is the shell thickness and r is the cylinder radium.

For the present modal analyses, the following two cases are considered:

(1) Although the tumbling mills have symmetric feature, we still use the whole model to do the modal analyses. If the symmetric models are chosen, some asymmetric modal will be lost.

(2) In this modal analysis, the pre-stress caused by the centrifugal force is included since the pre-stress will affect the natural frequencies.

5.3 Mode shapes

In Figure 5.4, Figure 5.5, Figure 5.6, and Figure 5.7, the mode shapes at mill circumferential vibration wave number (defined in chapter 2) m= 1, 2, 3 are illustrated respectively.

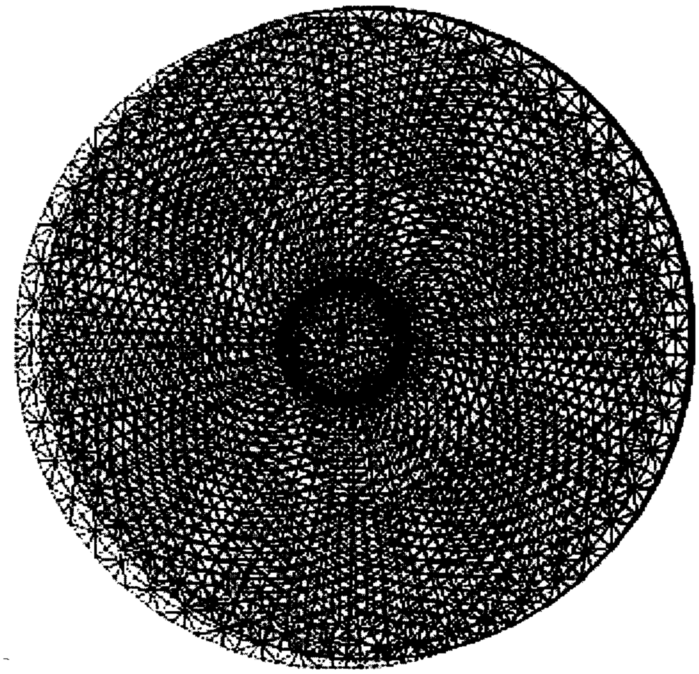

Figure 5.4 Mode shape at m=1

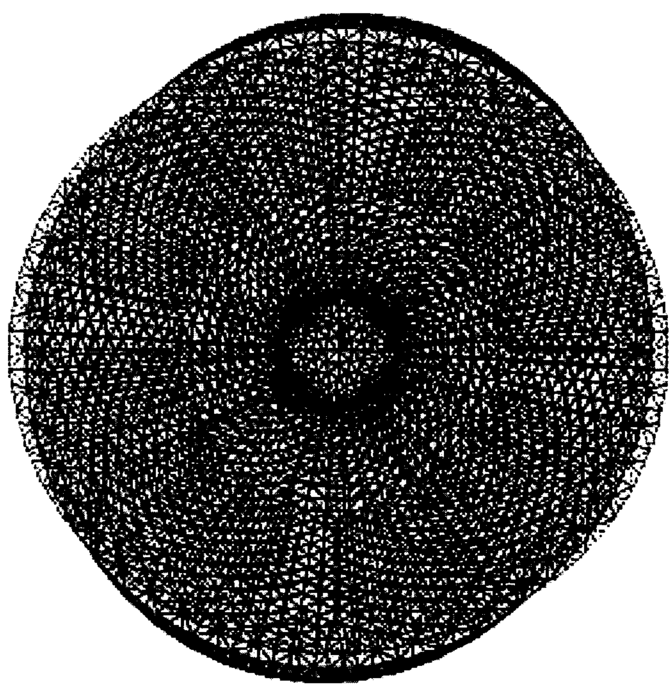

Figure 5.5 Mode shape at m=2

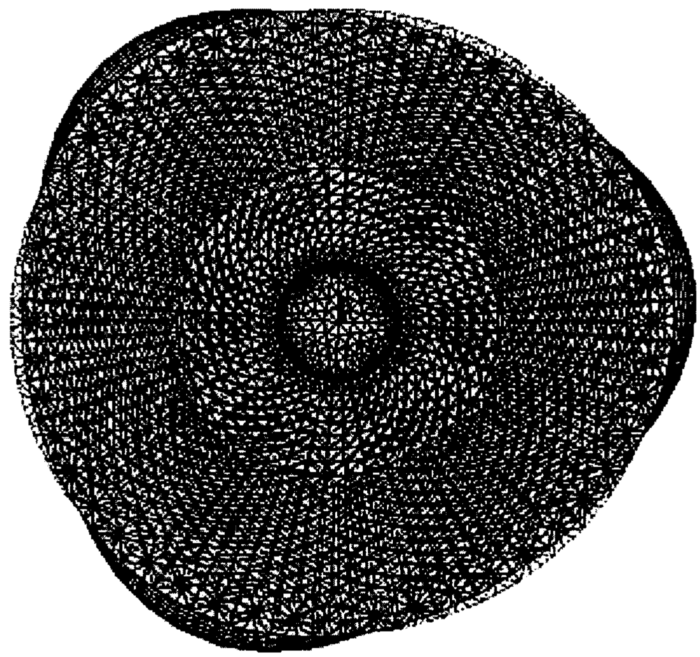

Figure 5.6 Mode shape at m=3

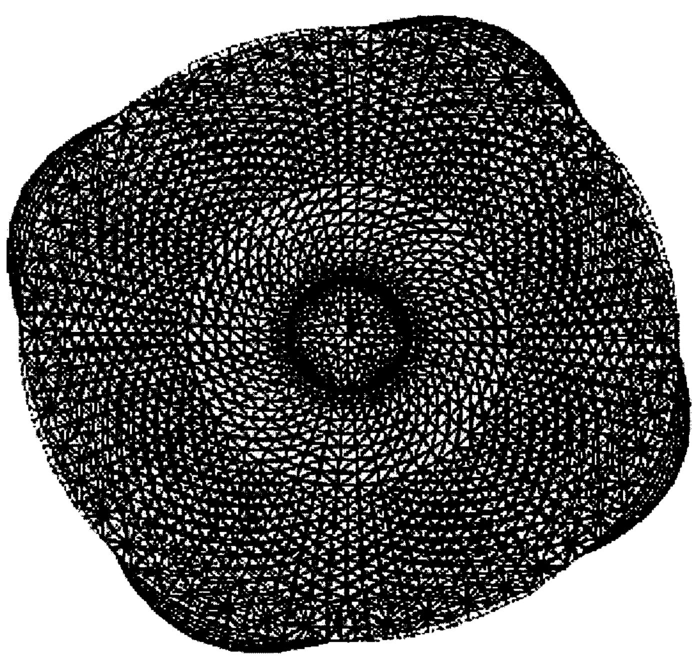

Figure 5.7 Mode shape at m=4

5.4 Resonant frequency as a function of mill aspect ratio

In this part, mill resonance as a function of mill aspect ratio and mill operating speed is thoroughly explored by FEA modal analysis. Block Lanczos method is used to obtain the eigenvalues and eigenvectors. SOLID92 elements are used to generate the FE models in order to adapt to the irregular geometry inside the mill. Moreover, the resonant properties of six different tumbling mill models are compared to explore the effects of mill parameters on the mill resonance. At last, the forward and backward waves are discussed and compared.

5.4.1 Mill FE Models

In order to explore the mill resonance as a function of mill aspect ratio (D/L) and operating speed, six mill models listed in Table 5.1 are analyzed. The details of the models are shown in Figure 5.8, Figure 5.9, Figure 5.10, Figure 5.11, Figure 5.12, and Figure 5.13 respectively.

	Model 1*	Model 2	Model 3	Model 4	Model 5	Model 6
D (mm)	8530	6150	4920	4265	2460	2132.5
L (mm)	4920	4920	4920	4920	4920	4920
D/L	1.7337	1.25	1	0.8669	0.5	0.4334

*: Brunswick tumbling mill

Table 5.1 Parameters of six different mill models

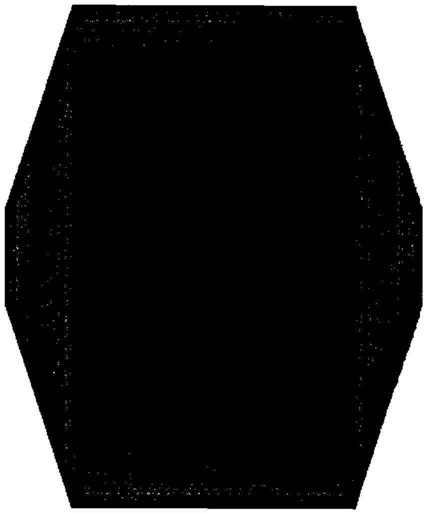

Figure 5.8 FEA model of model 1

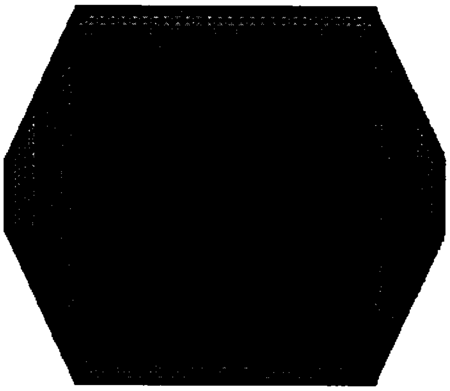

Figure 5.9 FEA model of model 2

Figure 5.10 FEA model of model 3

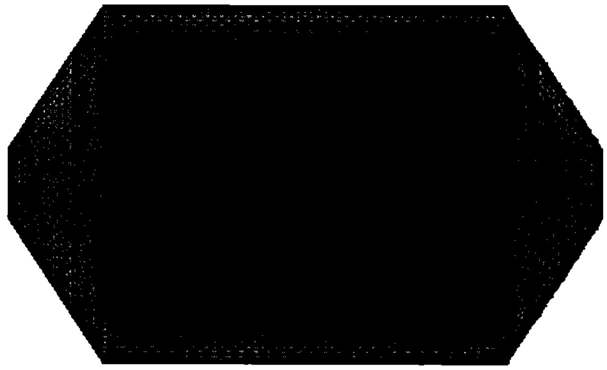

Figure 5.11 FEA model of model 4

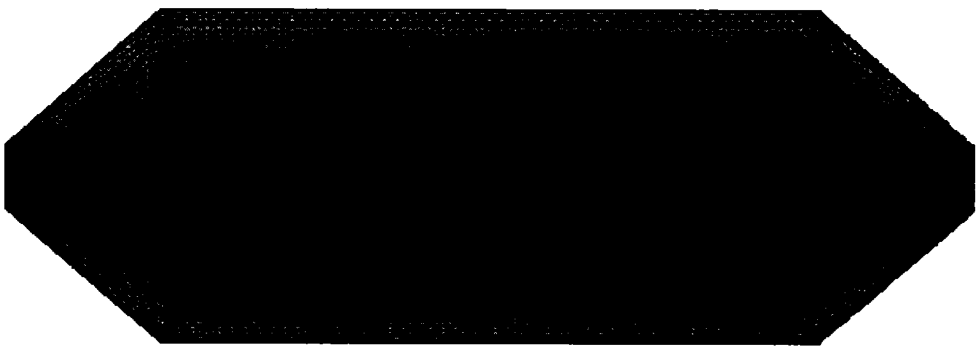

Figure 5.12 FEA model of model 5

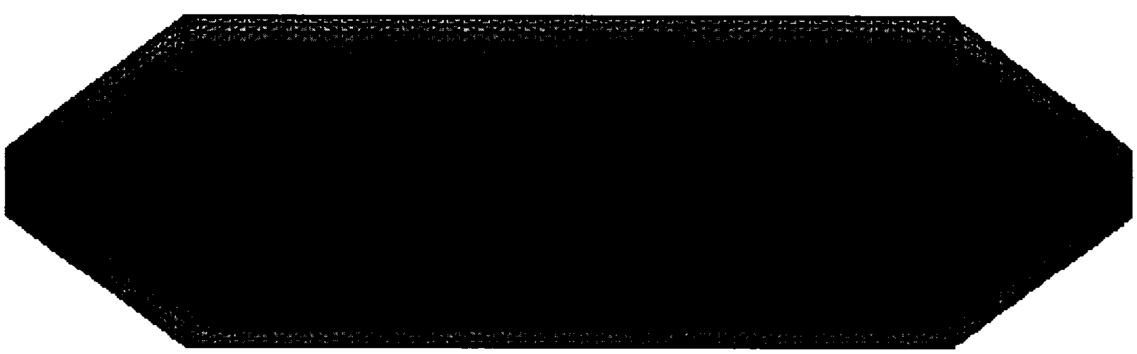

Figure 5.13 FEA model of model 6

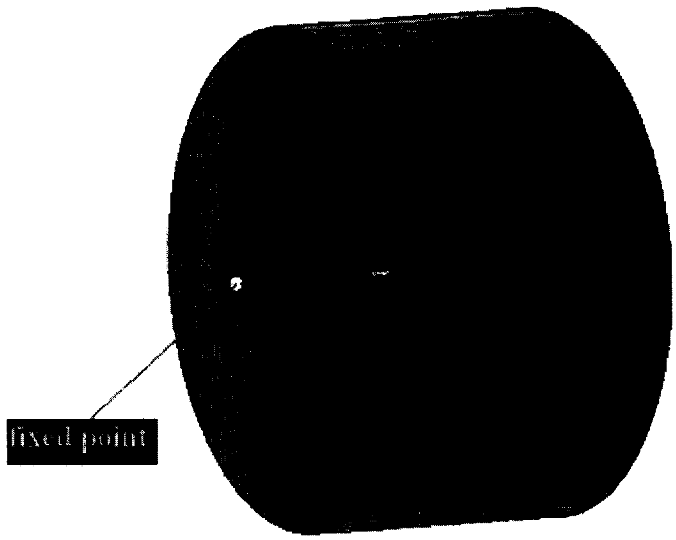

Figure 5.14 Translation-fixed mill

Different boundary conditions will induce different structural natural frequencies. This point is demonstrated in chapter 2. Meanwhile, under different boundary conditions, the relation between the natural frequencies and the mill velocities is different. In the present work, the translation-fixed-end boundary conditions are used, considering that the mill can only rotate about its central axis in its working state. With these kinds of boundary conditions, the two center points of the two ends of the mill models are fixed, as shown in Figure 5.14.

5.4.2 Model Results

In the present work, ANSYS software is used to calculate the natural frequencies of the six models. In Table 5.2, Table 5.3, Table 5.4, Table 5.5, Table 5.6, and Table 5.7, the natural frequencies, when the circumferential vibration wave numbers m= 0, 1, 2, 3, 4 and at rotation speed equals to 0, 5, 10, 15 and 20 rad/s, are listed. The corresponding curves are illustrated in Figure 5.15, Figure 5.16, Figure 5.17, Figure 5.18, Figure 5.19, and Figure 5.20. In the figures, the vertical axel represents the values of ratio f/f_0. f is the natural frequency at different rotation speeds, and f_0 is the natural frequency without considering rotation speed.

	m	Mill rotation speed (rad/s)				
		0	5	10	15	20
Frequency (HZ)	m=0	2.84E-02	2.84E-02	2.84E-02	2.84E-02	2.84E-02
	m=1	22.995	22.982	22.942	22.876	22.784
	m=1	23.046	23.033	22.993	22.928	22.835
	m=2	51.765	51.769	51.781	51.801	51.829
	m=2	51.825	51.829	51.841	51.862	51.89
	m=3	66.479	66.501	66.567	66.677	66.83
	m=3	66.533	66.554	66.62	66.73	66.883
	m=4	77.998	78.041	78.168	78.38	78.675
	m=4	78.147	78.19	78.317	78.528	78.823

Table 5.2 Mill frequencies at different speeds of model 1(D=8530mm, L=4920mm)

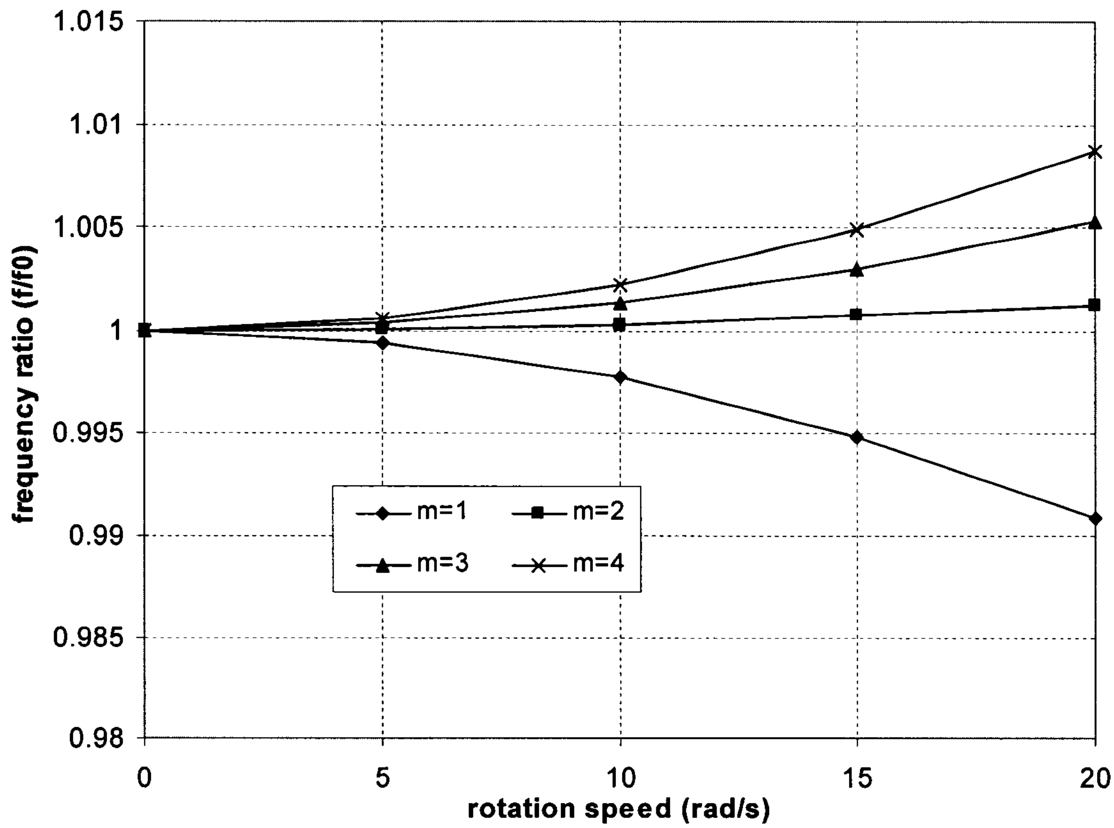

Figure 5.15 Speed related frequencies of model 1

	m	Mill rotation speed (rad/s)				
		0	5	10	15	20
Frequency (HZ)	m=0	4.55E-02	4.55E-02	4.55E-02	4.55E-02	4.55E-02
	m=1	27.154	27.143	27.108	27.051	26.97
	m=1	27.186	27.175	27.14	27.083	27.003
	m=2	52.613	52.617	52.63	52.652	52.683
	m=2	52.619	52.624	52.637	52.659	52.69
	m=3	52.174	52.204	52.292	52.44	52.644
	m=3	52.182	52.211	52.3	52.447	52.653
	m=4	54.86	54.923	55.113	55.428	55.866
	m=4	54.876	54.94	55.13	55.445	55.882

Table 5.3 Mill frequencies at different speeds of model 2 (D=6150mm, L=4920mm)

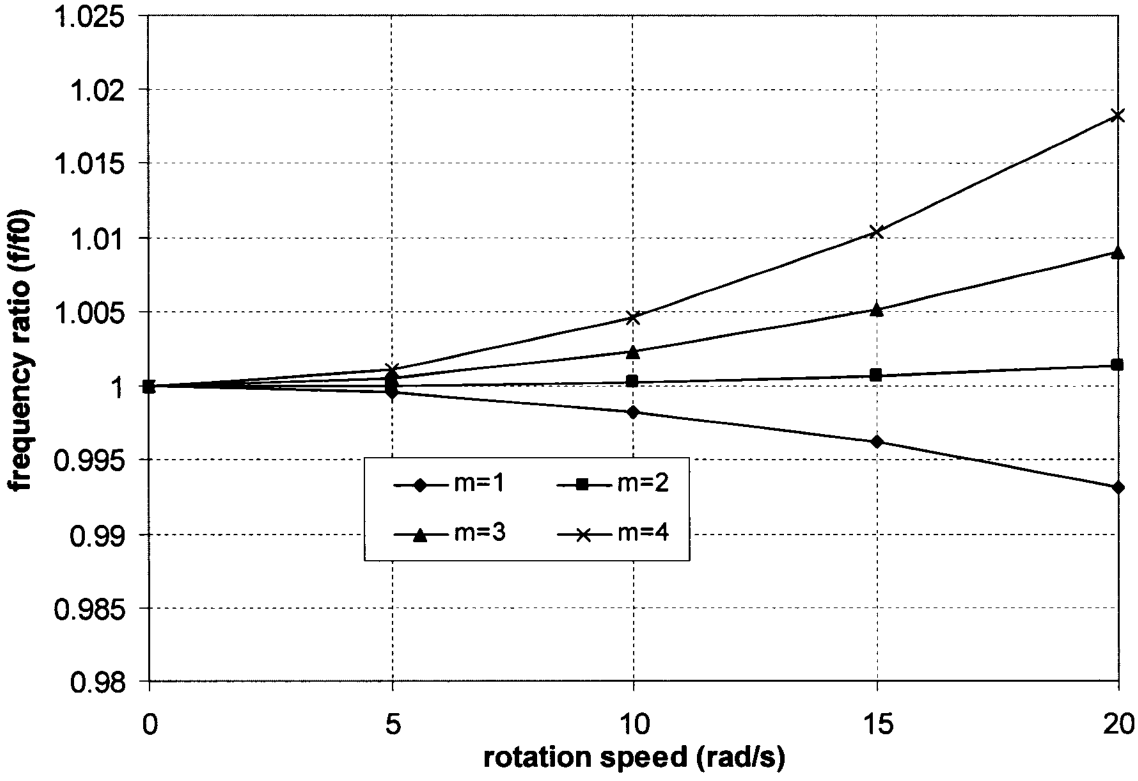

Figure 5.16 Speed related frequencies of model 2

	m	Mill rotation speed (rad/s)				
		0	5	10	15	20
Frequency (HZ)	m=0	2.09E-03	2.10E-03	2.09E-03	2.10E-03	2.09E-03
	m=1	28.727	28.716	28.684	28.63	28.554
	m=1	28.741	28.73	28.698	28.644	28.568
	m=2	52.994	53.002	53.194	53.52	53.975
	m=2	53.017	53.022	53.195	53.522	53.976
	m=3	49.168	49.199	49.293	49.449	49.666
	m=3	49.173	49.204	49.297	49.453	49.67
	m=4	52.93	52.992	53.011	53.032	53.062
	m=4	52.932	52.998	53.034	53.056	53.085

Table 5.4 Mill frequencies at different speeds of model 3 (D=4920mm, L=4920mm)

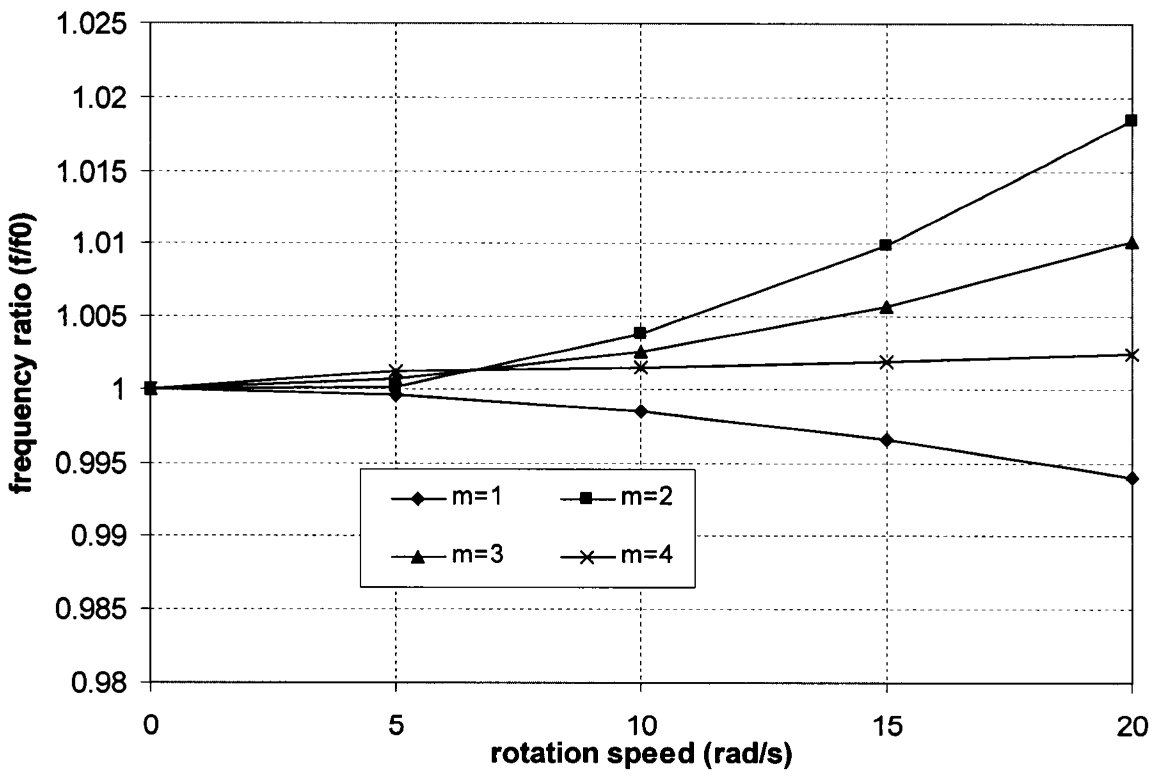

Figure 5.17 Speed related frequencies of model 3

	m	Mill rotation speed (rad/s)				
		0	5	10	15	20
Frequency (HZ)	m=0	5.37E-02	5.37E-02	5.37E-02	5.37E-02	5.37E-02
	m=1	34.19	34.181	34.153	34.107	34.042
	m=1	34.214	34.204	34.177	34.131	34.066
	m=2	66.783	66.786	66.795	66.81	66.832
	m=2	66.942	66.945	66.954	66.969	66.991
	m=3	87.381	87.399	87.451	87.537	87.659
	m=3	88.413	88.43	88.482	88.567	88.687
	m=4	119.41	119.44	119.53	119.67	119.87
	m=4	120.21	120.24	120.32	120.47	120.67

Table 5.5 Mill frequencies at different speeds of model 4 (D=4625mm, L=4920mm)

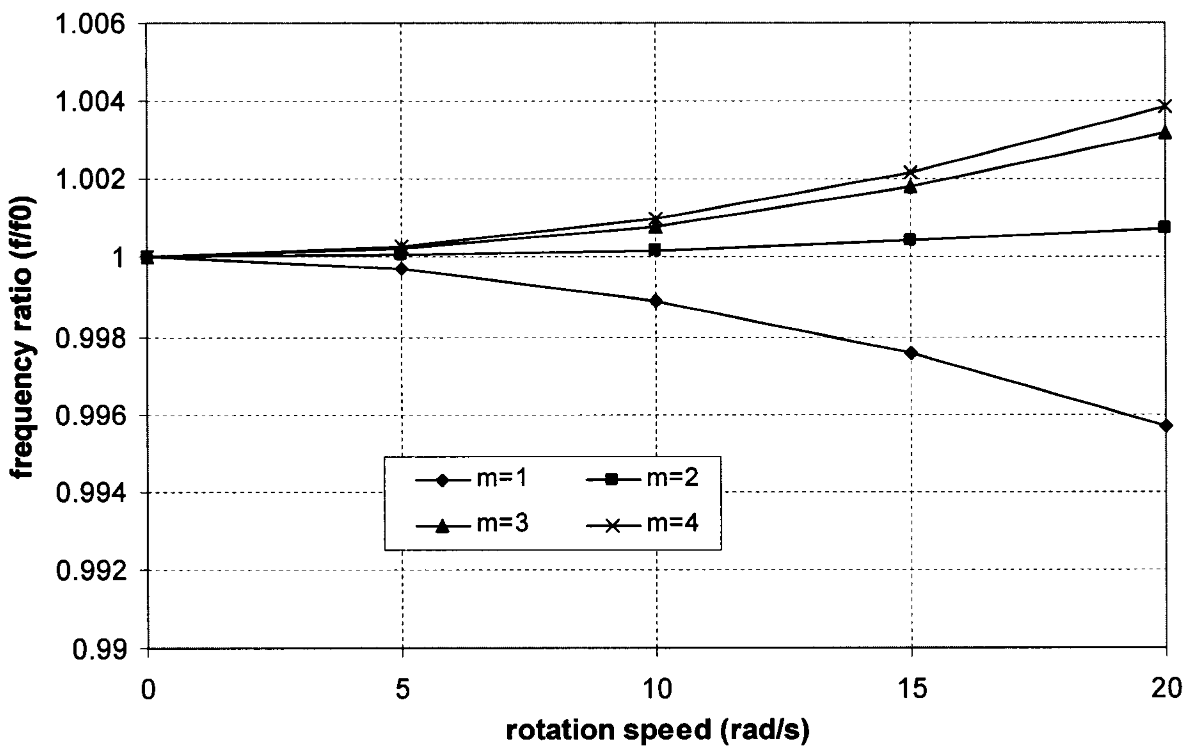

Figure 5.18 Speed related frequencies of model 4

	m	Mill rotation speed (rad/s)				
		0	5	10	15	20
Frequency (HZ)	m=0	4.81E-02	4.81E-02	4.81E-02	4.81E-02	4.81E-02
	m=1	36.88	36.871	36.846	36.803	36.743
	m=1	36.894	36.885	36.86	36.817	36.757
	m=2	45.897	45.902	45.915	45.938	45.971
	m=2	45.906	45.91	45.924	45.947	45.979
	m=3	52.156	52.185	52.273	52.419	52.623
	m=3	52.164	52.194	52.282	52.428	52.632
	m=4	83.158	83.2	83.326	83.535	83.827
	m=4	83.194	83.236	83.361	83.571	83.863

Table 5.6 Mill frequencies at different speeds of model 5 (D=2460mm, L=4920mm)

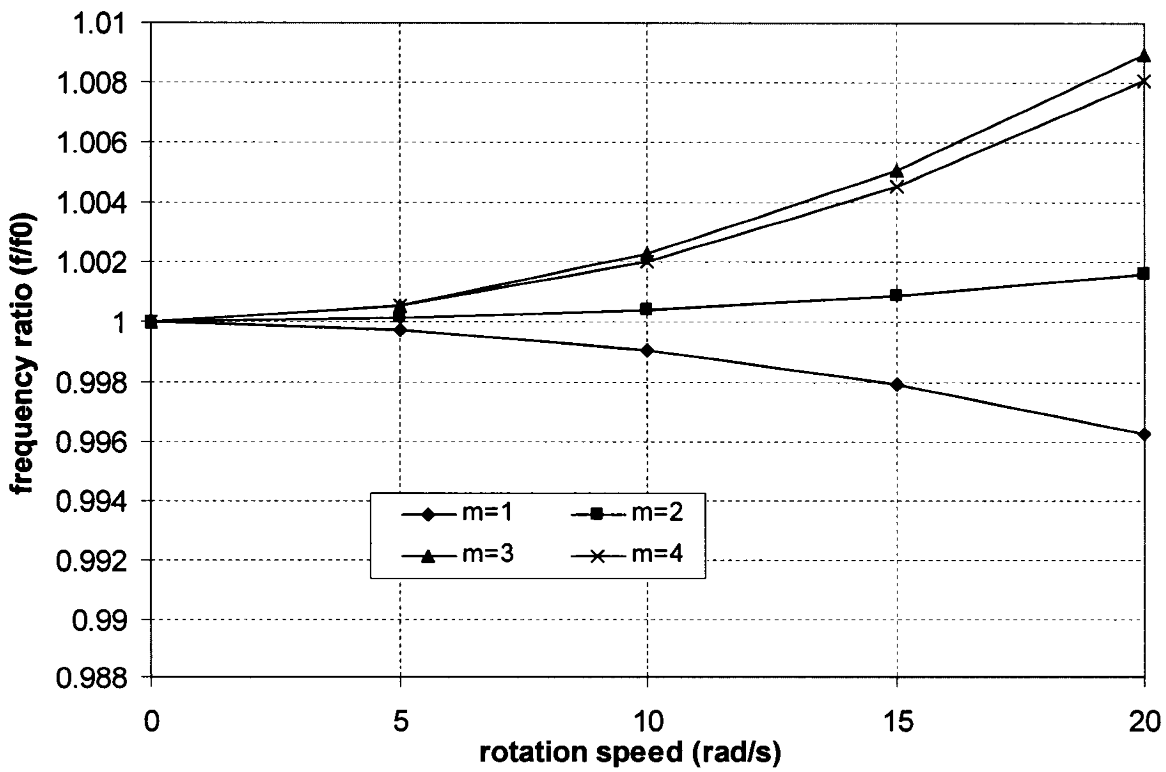

Figure 5.19 Speed related frequencies of model 5

	m	Mill rotation speed (rad/s)				
		0	5	10	15	20
Frequency (HZ)	m=0	7.64E-02	7.64E-02	7.64E-02	7.64E-02	7.64E-02
	m=1	38.433	38.425	38.4	38.359	38.302
	m=1	38.447	38.438	38.414	38.373	38.316
	m=2	43.07	43.075	43.09	43.114	43.148
	m=2	43.077	43.082	43.097	43.121	43.155
	m=3	55.435	55.462	55.545	55.683	55.875
	m=3	55.452	55.48	55.562	55.7	55.892
	m=4	93.3	93.337	93.449	93.636	93.897
	m=4	93.342	93.379	93.491	93.678	93.938

Table 5.7 Mill frequencies at different speeds of model 6 (D=2132.5mm, L=4920mm)

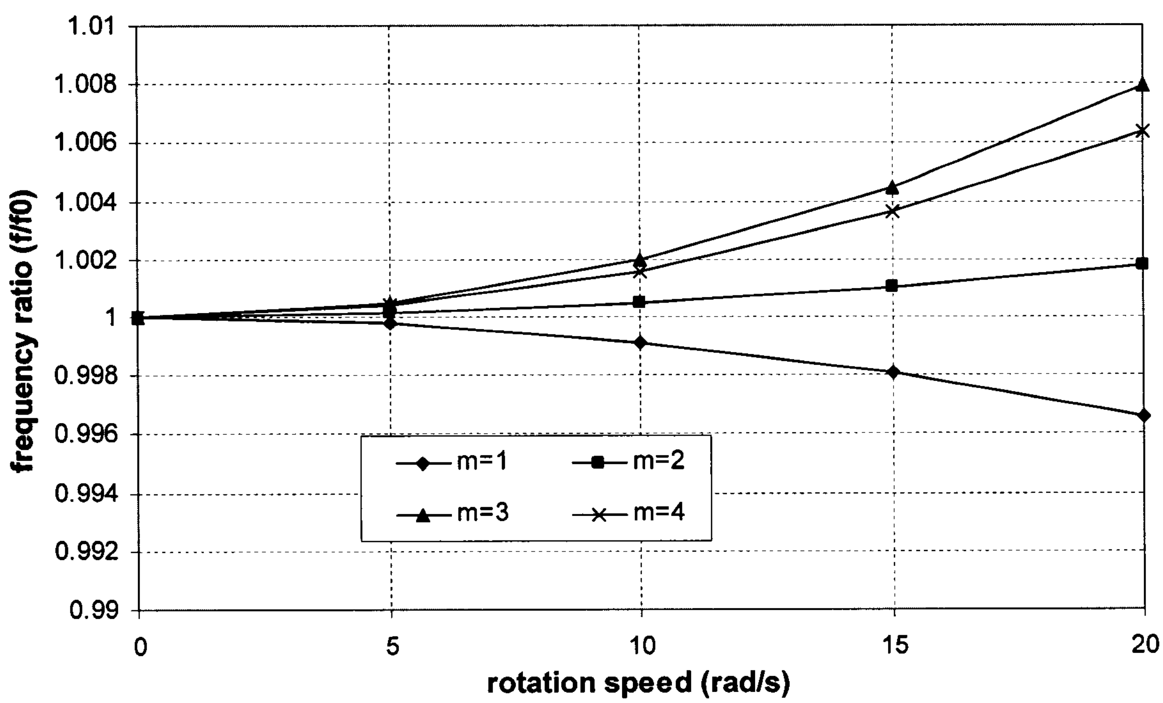

Figure 5.20 Speed related frequencies of model 6

From the above tables and figures, we can see that for all these six models, the natural frequencies of the models change with the mill's rotation speed and they have almost the same rules. But as to different circumferential vibration wave numbers, the natural frequencies changing tendencies are different. That is, for m=1, the higher the rotation speed of the mill is, the lower the frequency is. But for m=2, 3, 4, the higher the rotation speed is, the higher the frequency is. For the above six models, we consider the situations when the rotation speed varies in the range from 0 to 20 rad/s. This range is far over the mill running range, which is usually below 2 rad/s. In the mill working speed range, namely, 0~2 rad/s, the frequencies change not too much related to the rotation speeds. And the value of the natural frequencies gained from the FEA analyses are little different from the practical measured results. Why?

The reasons perhaps come from two aspects. First, as we mentioned before, the grinding system is a huge system. A system is a set of interactive and interdependent elements that work together to accomplish some desired goal. The mill system does not only include the mill itself. The other parts, such as motor, chain, gear box are all unneglectable. Besides, ground also has great influence on the system's vibration behavior. In order to get the exact frequency of the mill system, the model of the system must include all interactive and interdependent elements that work together to accomplish comminution. But as the first step of such an investigation, we cannot include all these into the model since the model will be too complex in that case and many parameters are too hard to decide at present. So the current research just gives us perceptual knowledge of how rotation speed will influence the structural natural frequencies. From this point, more work can be done to further investigate the exact system natural frequencies. Second, inside the mill, there are ores undergoing complex movement. How and to which degree the ores will influence the mill natural frequencies still needs to be investigated. In the next step, some corresponding experiments are needed to provide the necessary parameters for the FEA models.

Next, the relation between the frequencies and the rotation speeds of different models will be discussed. In Figure 5.21, Figure 5.22, Figure 5.23, and Figure 5.24, the vertical axis represents the frequency ratio of the mill natural frequencies at different rotation speeds to the natural frequency without considering rotation speeds

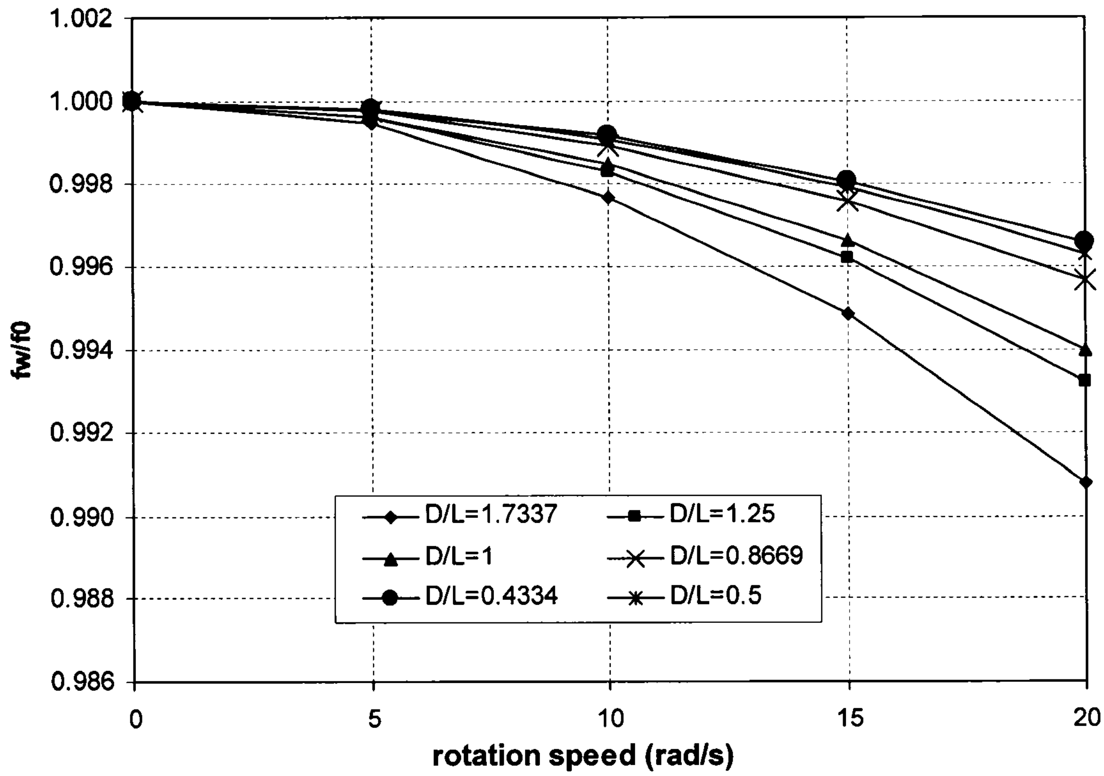

Figure 5.21 The relations between rotation speeds and frequencies at m=1

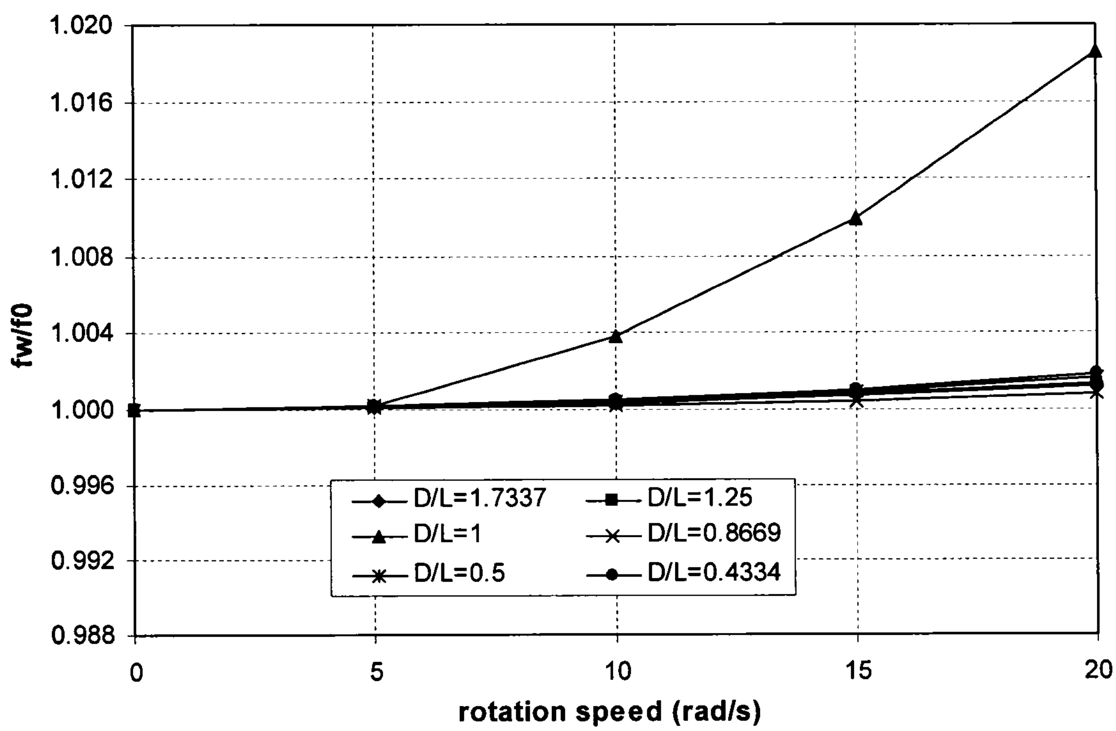

Figure 5.22 The relations between rotation speeds and frequencies at m=2

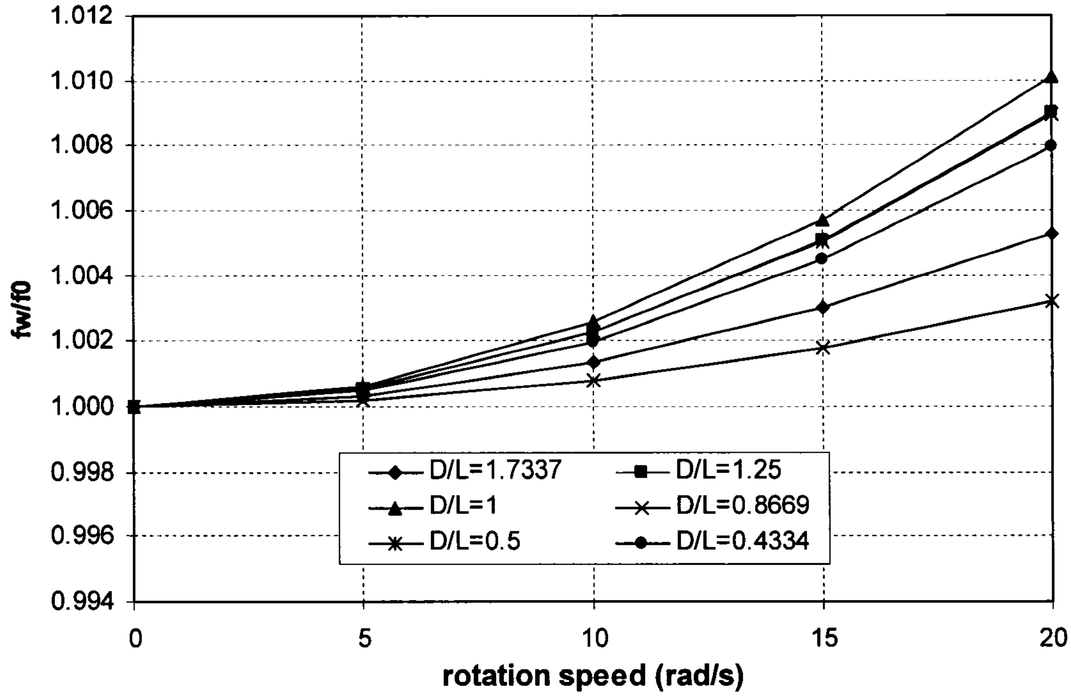

Figure 5.23 The relations between rotation speeds and frequencies at m=3

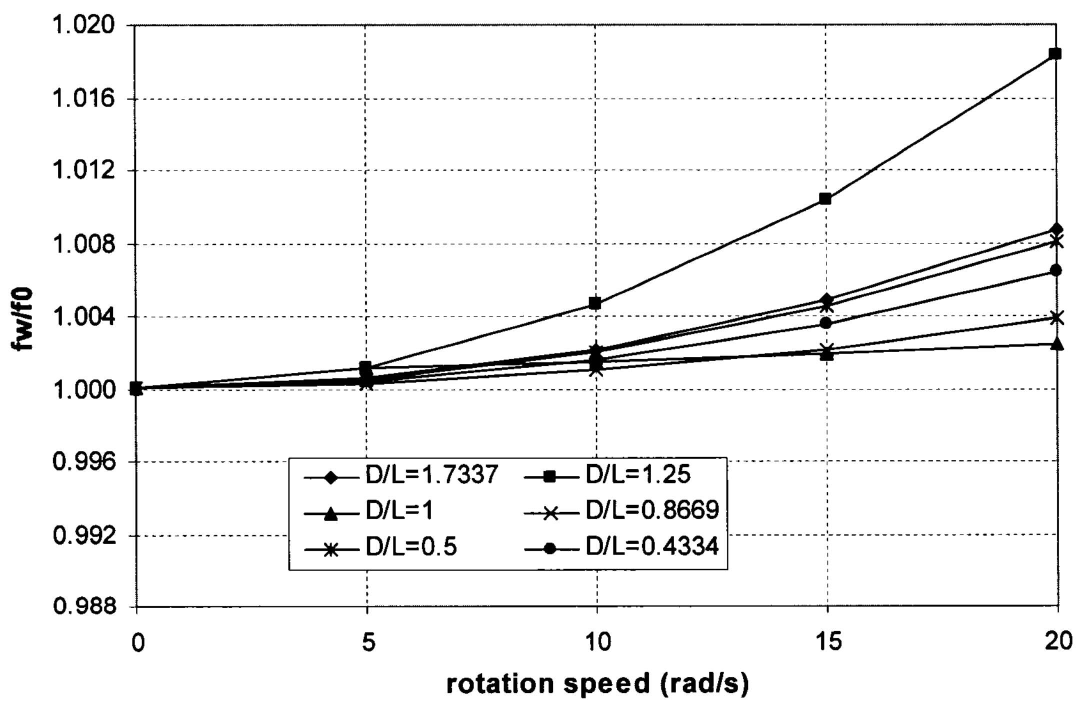

Figure 5.24 The relations between rotation speeds and frequencies m=4

From the above figures, we can draw the following conclusions:

(1) Different models show different speed-dependent tendencies. At m=1, the frequencies of model 1 (D/L=1.7337) have the greatest speed-related frequency feature and the frequencies of model 6 (D/L=0.4334) have the least speed-related frequency feature. At m=2, the model 3 (D/L=1) shows the greatest speed-related frequency feature and model 4 (D/L=0.8669) shows the least speed-related frequency feature. At m=3, model 3 (D/L=1) shows the greatest speed-related frequency feature and model 4 (D/L=0.8669) shows the least speed-related frequency feature. At m=4, model 2 (D/L=1.25) shows the greatest speed-related frequency feature and model 3 (D/L=1) shows the least speed-related frequency feature.

(2) Some models express stable speed-related frequency behavior while some models express opposite speed-related frequency behavior at different circumferential vibration numbers. For example, the frequencies of model 2 (D/L=1.25) always have obvious speed-related feature and the frequencies of model 4 (D/L=0.8669) are always less speed-related. But in contrast, model 3 (D/L=1) shows opposite speed-dependent tendencies at m=2 and m=4.

(3) From the results, we can arrive at such conclusion that each model possesses different speed-frequency relations at different order of vibration mode. For example, the natural frequencies of model 3 are remarkably related to rotation speed when m=2 while it has least relation to rotation speed when m=4. This point is very useful for mill structure optimization design.

5.5 Forward and Backward Wave

Using equation (5-1), the backward and the forward wave frequencies can be calculated. Figure 5.25 shows the backward and forward wave at circumferential vibration wave number m=1. It should be noted that in this case, the t / r ratio of equation (5-2) is equal to 0.095 (9.5%) which is greater that the thin shell definition (5%). In Figure 5.25, there are 2 forward waves and 2 backward waves since there are 2 mode shapes at m=1.

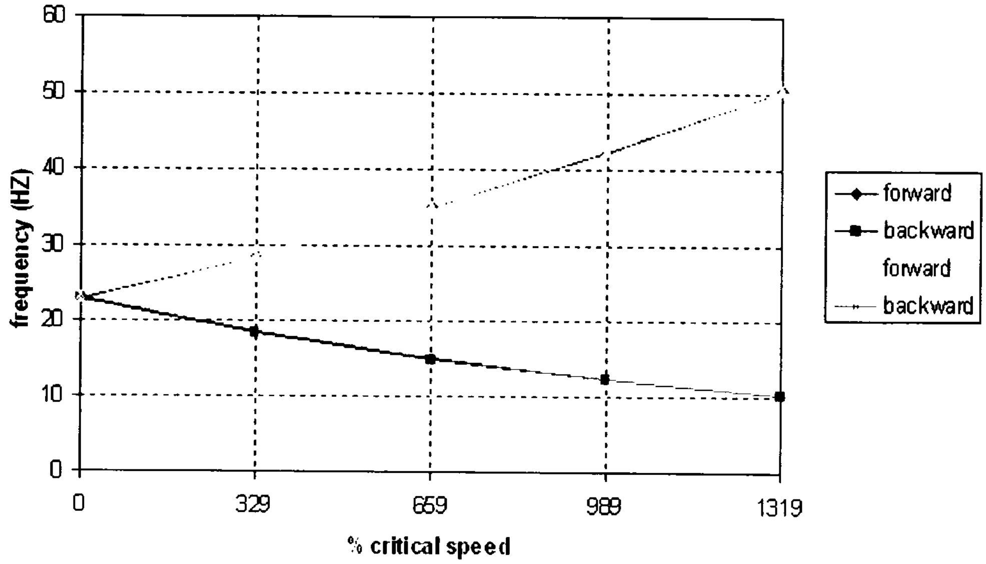

Figure 5.25 Backward and forward wave at m=1

5.6 Conclusions

The tables and figures shown above demonstrate that the rotation speeds of the mill and the mill parameters do relate to the mill resonant behaviour, while the calculated natural frequencies are higher than the practical ones. The main reason of this situation is that the simulation model used here only includes the mill tube and its covers while the other parts of the mill system are not taken into consideration. Although the tendencies in mill natural frequencies as a function of mill design (aspect ratio) and rotation speed are promising, further work is needed. Here, one can cite completing the mill model to integrate pulp lifters and mill charge. Also, experimentation on a real mill to determine and validate vibration modes is needed. Once this work is completed and validated, it will become possible to address avenues to correct mill resonance in existing mills or to prevent the design and fabrication of mills that would show unwanted resonant behaviour.

CHAPTER 6

CONCLUSIONS AND RECOMMENDATIONS

6.1 Conclusions

In this thesis, three aspects are discussed and studied by means of finite element analysis: tumbling mill liner bolt stress and strain; tumbling mill liner stresses with the liner wear sensors considered; and tumbling mill resonance exploration. The following conclusions can be drawn by the previous analyses:

(1) The liner bolt strain analysis gives us some clue that the strains of liner bolts can definitely reflect the charge motion inside the mill, while the numerical variations are small. All the variations are no more than 4%. The main reason is that the bolt preload is so big that it usually reaches 75%-95% of the bolt proof stress. Thus, the stress and strain distributions at the bolts and their surrounding areas are greatly influenced by bolt preload.

(2) The liner stress analysis provides strong theoretical basis for the application of liner wear sensor which was developed by Sudarshan Martin, Wei Li and Prof. Peter Radziszewski. The effect of liner wear sensor placement on liner structural strength is analyzed by FEA impact analysis and structural analysis. The results show that calculated maximum stress is much lower than the yield stress of liner material. That is, this kind of liner sensor is accessible from the view point of material strength. Besides, the effect of liner thickness on the liner stress is also analyzed. The analysis shows that when the liner thickness is reduced below a certain value, it has great influence on stress distribution.

(3) The tumbling mill resonance analysis explores the relation between the mill resonance and the mill aspect ratio; the relation between the resonance and the mill operating speed. The FEA modal analysis results demonstrate that the rotation speeds of the mill and the mill parameters do relate to the mill resonant behaviour. But, since the FE models do not consider the other components of the mill system except the mill itself, the calculated natural frequencies are higher than the practical ones. By comparing the natural frequencies of six different mill models defined in chapter 5.4.1, the effects of mill

parameters on the mill resonance are clearly reflected. Mill parametric design is very important for designers to avoid mill resonance.

6.2 Recommendations

The research in the three aspects studied above in this thesis provides us a lot of useful information. While as mentioned in the conclusions and the corresponding chapters, for liner bolt and mill resonance analyses, there is still a lot of work to be carried on in the future:

(1) The stresses and strains of liner bolts and surrounding areas are greatly influenced by bolt preload. If we can reduce the torque preload in instrumented bolts, we can get more obvious rules of the liner bolt stress change depending on different liner positions. Then this research will be very valuable for industry utilization of bolt strain sensors. This possibility will be further investigated in the future.

(2) For mill resonance analysis, a lot of work needs to be done. First, a complete tumbling mill FE description is needed. In the current research, the mill FE model only includes the mill tube and its covers while the other parts of the mill system are not taken into consideration. Although the tendencies in mill natural frequencies as a function of mill design (aspect ratio) and rotation speed are obtained, numerical error still exists. Second, practical experiments are needed to decide the related mill system parameters. A good FE model cannot separate from believable parameter data. The reason for choosing such a simple model in the current work is partially because of the incomplete parameters. Third, experimentation on a real mill to determine and validate vibration modes is needed. The FEA analysis needs to be improved and validated by experiments. Once these points are fulfilled, the mill FEA resonance analysis will provide powerful tools for avoiding mill harmonic and provide useful suggestions for mill structural design.

REFERENCES

[1] T. A. Apelt, S. P. Asprey, N. F. Thornhill, "*Inferential measurement of SAG mill parameters II: state estimation*", Minerals Engineering, Volume 15, Issue 12, December 2002, Pages 1043-1053

[2] P. Radziszewski, Y. Y. Quan, J. Poirier, "*Design parameters affecting tumbling mill natural frequencies*", CDEN Conference, 2005, Montreal, Canada

[3] David J. Dunn, "*Optimizing ball mill liners for production and economy*", Climax Molybdenum Co.

[4] N. Djordjevic, "*Discrete element modeling of lifter stresses in tumbling mill*", Mineral Processing and Extractive Metallurgy : IMM Transactions section C, August 2003, vol. 112, no. 2, pp. 115-119(5)

[5] R.K. Rajamani, B.K. Mishra, P. Songfack and R. Venugopal, "*Millsoft—simulation software for tumbling-mill design and trouble shooting*", Mining Engineering, 1999

[6] Radziszewski, P., Tarasiewicz, S., "*Simulation of ball charge and liner wear*", Int'l J. on WearFriction and Lub., 169, 2003, pp 77-85.

[7] Herbst, J.A., Nordell, L.K. (2001), "*Optimization of Ball Charge and Liner Wear*", Int'l J. on Wear, Friction and Lub., 169. 77-85

[8] R. P. KING: "*Modeling and simulation of mineral processing systems*", 2001, London, Butterworth- Heinemann.

[9] P. Radziszewski and S. Morrell, "*Fundamental discrete element charge motion model validation*", Minerals Engineering, Vol.11, No.12, pp.1161-1178, 1998

[10] Inoue, Okaya, "*Grinding mechanism of centrifugal mills-A batch ball mill simulator*", Int'l J. Mineral Processing, 1996, 44-45, 425-435

[11] Mishra, Rajamani, "*Simulation of charge motion in ball mills, Part 2: numerical simulations*", Int'l J. mineral processing, 1994, 40, 187-197

[12] http://www.cmis.csiro.au/cfd/dem/ballmill_3D/index.htm

[13] Moys, M.H., "*The measurement of parameters describing the dynamic behaviour of the load in a grinding Mill*", MINTEK 50 International Conf. on Recent Advances in Mineral Sciences and Technology, Sandton, March 1984

[14] Herbst, J.A., Rajamani, K., "*The application of modern control theory to mineral processing operations*", In: Glen, H.W. (Ed.), Proc. of the 12th CMMI Congress, Vol. 2. S. Afr. Inst. Min. Metall., Johannesburg, 1982, pp. 779–792.

[15] Herbst, J.A., Hales, L.B., Gabardi, T.L., "*Continuous measurement and control of charge volume in tumbling mills*", In: Rajamani, R.K., Herbst, J.A. (Eds.), Control _90—Mineral and Metallurgical Processing. SME Littleton, CO, 1990, pp. 163–169.

[16] Moys, M.H., Montini, A., "*The use of conductivity measurements in the control of grinding mills*", CIM Bull, 80 (907), 1987, pp 52–56.

[17] Moys, M.H., "*Slurry rheology: the key to further advance in grinding mill control*", Int. Conf. on Autogeneous and semi-Autogeneous Grinding, Vancouver, British Columbia, 1989, pp 713-727.

[18] Shi, F.N., Napier-Munn, T.J., "*Estimation of shear rates inside a ball mill*", Int. J. Mineral Process, 57, 1999, pp 167–183.

[19] Shi, F.N., Napier-Munn, T.J., "*Effects of slurry rheology on industrial grinding performance*", Int. J. Mineral Process, 65, 2002, pp 125–140.

[20] Pax, R.A., "*Non-contact acoustic measurement of in-mill variables of SAG mills*", Proceedings of the International Conference on Autogenous and semi-Autogenous Grinding Technology, 2001, Vancouver, Canada, pp. 386–393.

[21] Tano, K., Palsson, B., Persson, S., 2003. "*Continuous monitoring of a tumbling mill*", Proceedings XXII International Mineral Processing Congress, Cape Town, South Africa.

[22] Dupont, J.F., Vien, A., 2001b, "*Direct measurement and control of SAG volumetric loads using embedded sensors*", In: Preprints of the SME Annual Meeting, USA, pp. 1–5.

[23] ANSYS Inc., "ANSYS 9.0 documentation"

[24] Thompson, Erick G. "*An Introduction to the finite element method*", Hoboken, NJ, John Wiley, 2005

[25] G. M. L. Gladwell, D. K. Vijay, "*Natural frequency of free finite-length circular cylinders*", Journal of Sound and Vibration 42(3), 1975, pp 387-397

[26] http://www.donhad.com.au/donhad_pdf/LBoltTp.pdf

[27] http://www.maths.usyd.edu.au/u/AppliedSeminar/abstracts/2003/spencer.html

[28] Herbst J.A., Gabardi T.L., "*Closed loop media charging of mills based on a smart sensor system*", In: Sommer G. (Ed.), IFAC Applied Measurements in Mineral and Metallurgical Processing, Transvaal, South Africa, 1988, pp 17-23.

[29] Vermeulen,L.A., Schakowski,F.A, "*Estimation, by use of a conductivity bolt, of the charge volume and other milling parameters in an operating mill*", IFAC Applied Measurements in Mineral and Metallurgical Processing, Sommer. G.ed., Transvaal, South Africa, 1988, pp 11-15.

[30] http://www.mech.uwa.edu.au/DANotes/threads/preload/preload.html

[31] Roymech, "*Bolt preloading*", http://www.roymech.co.uk

[32] http://www.roymech.co.uk/Useful_Tables/Screws/Preloading.html

[33] Martins, Radziszewski, Coleman, "*An instrumented lifter for tumbling mill wear Monitoring*", CANCAM Conference, 2005, Canada

[34] J. T. Kalala, M. Bwalya, M. H. Moys, "*Discrete element method (DEM) modeling of evolving mill liner profiles due to wear. Part II. Industrial case study*", Minerals Engineering, Volume 18, No. 15, 2005

[35] K. T. Tano, B. I. Palsson, A. Sellgren, "*On-line lifter deflection measurements showing flow resistance effects in grinding mills*", Minerals Engineering, Vol. 18, No.11, 2005

[36] J. T. Kalala, M. Bwalya, M. H. Moys, "*Discrete element method (DEM) modeling of evolving mill liner profiles due to wear. Part I: DEM validation*", Minerals Engineering, Vol. 18, No.15, 2005

[37] S. Martin, W. Li, "*Liner wear sensor project report*", 2005

[38] Cohen L., "*Time-frequency distributions - A review*", Proceedings of the IEEE, 77, 1989, pp 941-981

[39] Granulair Technologies, http://www.granulair.com/gallery/ball-mill.html

[40] Genta G., "*A fast modal technique for the computation of the Campbell diagram of multidegree-of-freedom rotors*", Journal of Sound and Vibration, 155(3), 1992, pp 385-402

[41] K. S. Liddell, M.H. Moys, "*The effects of mill speed and filling on the behavior of the load in a rotary grinding mill*", Journal of the South African Institute of Mining and Metallurgy, Vol. 88, No.2, February, 1998, pp49-57

[42] Panta Engineering corp., http://www.penta.net/projects_vibration.html.

[43] Newland D. E., "*An introduction to random vibration and spectral and wavelet analysis*", 3rd Ed., Longman Group Limited, 1993

[44] S. M. Hashemi, M. J. Richard, "*Natural frequencies of rotating uniform beams with coriolis effects*", Transactions of the ASME, Vol.123, October 2001

[45] M. Behzad, A.R. Bastami, "*Effect of centrifugal force on natural frequency of lateral vibration of rotating shafts*", Journal of Sound and Vibration, Vol. 274, 2004

[46] J. W. Tedesco, W. G. Mcdougal, C. A. Ross, "*Structural dynamics: theory and applications*", Prentice-Hall, 1999

[47] Y. Chen, H.B. Zhao and Z.P. Shen "*Vibrations of high speed rotating shells with calculations for cylindrical shells*" Journal of Sound and Vibration (1993) 160(1), p137-160

[48] K.M. Liew, T.Y. Ng and X. Zhao "*Vibration of axially loaded rotating cross-ply laminated cylindrical shells via Ritz method*" Journal of Engineering Mechanics, Vol. 128, No. 9, September 2002, pp. 1001-1007

[49] V.V. Novoshilov, "*Thin shell Theory (2nd edition)*", Groningen, P. Noordhoff, 1964